

Level 2 Photometric Calibration for the LSST Survey

R. Lynne Jones¹, Tim Axelrod², Željko Ivezić¹, David Burke³, Christopher Stubbs⁹,
James G. Bartlett⁴, Gurvan Bazin⁴, Guillaume Blanc⁴, Alexandre Boucaud⁴,
Jean Marc Colley⁴, Michel Crézé⁴, Mario Juric⁸, Cécile Roucelle⁴, Abhijit Saha⁵,
J. Allyn Smith⁷, Michael A. Strauss⁶, Peter Yoachim¹
on behalf of The Photometric Calibration Team
Docushare-8123, 07/01/13

ABSTRACT

This document describes the photometric calibration procedure for LSST Data Release catalogs. This procedure will use specialized hardware, an auxiliary telescope, an atmospheric water vapor measurement system, and narrow-band dome screen illuminator, to measure the wavelength dependence of the atmospheric and hardware response functions, together with a self-calibration procedure that leverages multiple observations of the same sources over many epochs, to deliver 1%-level photometry across the observed sky.

Contents

1	Introduction	4
2	Photometric Requirements	6

¹University of Washington

²University of Arizona

³SLAC National Accelerator Laboratory

⁴APC, Université Paris Diderot

⁵NOAO

⁶Princeton University

⁷Austin Peay State University

⁸LSST Corp

⁹Harvard University

3 The Photometric Calibration Process	7
4 From Flux to Counts	9
4.1 Bandpasses and Associated Magnitudes	11
4.2 Perturbations to the System Bandpass	13
4.3 Effects of Airmass Variation	14
4.4 Effects of Atmospheric Variations	14
4.5 Throughput Variations Due to Contamination	16
4.6 Variations in Detector Quantum Efficiency	16
4.7 Throughput Variations Due to Filter Position Shifts	16
4.8 Putting it All Together	17
5 From Counts to Flux	17
5.1 Measuring the Hardware Response	17
5.1.1 Determining the Illumination Correction	19
5.1.2 Normalizing Fluxes Across Wavelengths	20
5.1.3 Correcting for Pixel Geometry	20
5.1.4 Accounting For Finite PSF Width	20
5.1.5 Constructing the Synthetic Flat	23
5.2 Measuring the Atmospheric Transmission	23
5.3 Estimating SEDs From Colors	26
5.4 Finding the Zero Points: Self Calibration	26
5.5 Calibration Operations	28
6 Fixing LSST to an external scale	29
6.1 White Dwarf Standards	30
6.2 Population Methods	32

6.3	Computational Technique for Determining Δ_{b-r}	33
7	Calibration Hardware	33
7.1	Flat Field Illumination System	33
7.2	Auxiliary Telescope	33
7.3	Water Vapor Monitoring System	34
7.4	Camera System Telemetry	34
8	Calibration Error Budget	35
8.1	Repeatability Errors	35
8.1.1	errors in m_b^{inst}	36
8.1.2	errors in Δm_b^{obs}	36
8.1.3	errors in Z_b^{obs}	38
8.2	Uniformity errors	41
9	Testing and Verification	42
9.1	Self Calibration Simulation	42
9.1.1	Self-Calibration of a Large System Using HEALpixels	43
9.2	Auxiliary Telescope Simulation	44
9.3	Calibration Performance Metrics	45
9.3.1	Repeatability	45
9.3.2	Spatial Uniformity	45
9.3.3	Flux Calibration	45
9.3.4	Color Calibration	46
10	Software Implementation	46
10.1	Calibration Products Production	46
10.2	Calibration Within the Data Release Production	47

10.3 Level 2 Data Products	47
10.3.1 Storing and Obtaining $\phi_b(\lambda \mathbf{p})$	48
10.3.2 Database-level Recalibration	49
11 Risks and Mitigations	49
A Filter Set	55
B Photometric measurements for non-main sequence stars	55
C Fiducial Self-Calibration Input	56
D Glossary	60

1. Introduction

LSST is required to deliver photometry with 1% uniformity and 0.5% repeatability across the observed sky and under a wide range of observing conditions. This represents at least a factor of two improvement over current wide-field surveys such as SDSS, CFHTLS, and PanSTARRS. This factor of two improvement will have a major impact on science deliverables because it implies that the uncertainty volume in the five-dimensional LSST color space will be over thirty times smaller than for SDSS-like photometry. This smaller uncertainty volume will improve source classification and the precision of quantities such as photometric redshifts for galaxies and photometric metallicity for stars. For example, a given spectral energy distribution (SED) corresponding to some galaxy type produces a 1-D locus in the *ugrizy* multi-dimensional color space when redshifted, where the position of the galaxy along that line in *ugrizy* space is a function of redshift. Different galaxy SEDs produce lines that are often close to each other in *ugrizy* space and sometimes even cross. The smaller the uncertainty volume around an observed galaxy’s measured *ugrizy* colors, the smaller the number of different lines (thus, different SEDs) and different positions along the line (thus, different redshifts) which will be consistent with the measurement. The same conclusion is valid in the case of algorithms that estimate stellar effective temperature and metallicity, as well as any other model-based interpretation of measurements. Furthermore, the smaller uncertainty volume per source is advantageous even in the absence of any models. Two sources whose color differences produce a value of χ^2 per degree of freedom of 1, will

have a χ^2 per degree of freedom of 4 when the uncertainties are halved. In case of five degrees of freedom, χ^2 pdf > 4 will happen by chance in only 0.1% of all cases. Therefore, the ability to reliably detect color differences between sources is a strong function of photometric uncertainties.

SDSS is widely credited with pioneering high accuracy photometry for large surveys, and it is instructive to compare its photometric calibration procedure with LSST’s. The factor of two reduction in photometric uncertainty results from two major differences between the surveys. First, each source will receive hundreds of observations in each band over the ten years of the LSST survey, a much greater number than possible with SDSS. These series of repeat observations will be used to self-calibrate the photometric system across the sky and for each observation (akin, but not identical to, the uber-calibration procedure used by SDSS (Padmanabhan et al. 2008)), allowing LSST to operate in strongly nonphotometric conditions. Secondly, the wavelength dependence of the hardware and atmospheric transmission response functions will be measured with auxiliary instrumentation on sufficiently fine angular and temporal scales to enable their explicit inclusion in the calibration procedure, rather than resorting to traditional approximations such as linear color terms. SNLS re-processing of CFHT Legacy Survey data found these color-dependent terms to be a significant contributor to photometric calibration uncertainties (Regnault et al. 2009), on the level of several percent.

This document describes the calibration requirements and processes for LSST Data Release photometry. At each Data Release, there will be a complete recalibration of all data acquired to that point, on approximately an annual schedule. These data products are referred to as Level 2 Data Products. There will also be a separate photometric calibration process that provides near real-time, but lower quality, photometry for quality assurance, generation of alerts, and other quantities required on a nightly basis. This Level 1 photometric calibration process is not discussed here.

Section 2 reviews the survey requirements for photometric calibration, while Section 3 describes the foundation of LSST’s calibration procedure, first motivating this procedure by describing the transmission of flux through the atmosphere and LSST system and then from the calibration point of view, trying to recreate the flux from the ADUs measured by the detector. Sections 4 and 5 describe those aspects in some detail. Section 6 describes how the LSST’s internal photometric scale is tied to external references. Section 7 describes the hardware required to realize the calibration process. Section 8 presents the uncertainty budget for each step of the calibration procedure. Section 9 describes how we will verify that the calibration system functions as designed, and meets the science requirements, first during the construction phase, and later during survey operations. Section 10 describes

the implementation of the calibration process in software that will be part of LSST Data Management. Finally, Section 11 discusses the risks that remain in the implementation of the calibration process, and the steps we are taking to mitigate them.

2. Photometric Requirements

The LSST Science Requirements Document (SRD) provides a set of requirements on the annual Data Release (Level 2) photometry. These requirements are extended in the LSST System Requirements (LSR), the Observatory System Specifications (OSS), and the individual subsystem requirements documents, to cover aspects which are too detailed for the SRD. In this section we consider only requirements from the SRD. Calibration requirements from the LSR and below are discussed further in Section 8 on the calibration uncertainty budget.

The SRD requirements are based on measurements of bright, unresolved, isolated, non-variable main-sequence stars from individual LSST visits. In this context, “bright” implies that the measurement of the star’s brightness is not dominated by photon statistics, approximately 1-4 magnitudes fainter than the saturation limit in a given filter. “Isolated” implies that the star’s photometry is not significantly affected by nearby galaxies or stars. “Non-variable” objects are astrophysically non-variable at levels well below calibration requirements (1 mmag or less); these will be identified in an iterative fashion from the many epochs of LSST observations. The “main-sequence” restriction derives from the need for accurate knowledge of the SEDs of calibration objects, given only their multi-band photometry. Calibration of objects with non-MS SEDs is discussed in Appendix B.

The SRD specifications are:

1. **Repeatability:** the median value of the photometric scatter for each star (the rms of calibrated magnitude measurements around the mean calibrated magnitude) shall not exceed 5 millimags in *gri*, 7.5 millimags in *uzy*. No more than 10% of these objects should have a photometric scatter larger than 15 mmag in *gri*, 22.5 mmag in *uzy*. This requirement sets the level above which we can reliably detect intrinsic variability in a single source.
2. **Uniformity:** the rms of the internal photometric zeropoint error (for each visit) shall not exceed 10 millimags in *grizy*, 20 millimags in *uzy*. No more than 10% of these sources can be more than 15 mmag in *gri* or 22.5 mmag in *uzy* from the mean internal zeropoint. This places a constraint on the stability of the photometric system across the sky as well as an upper limit on various systematic uncertainties, such as any correlation

of photometric calibration with varying stellar populations (or colors). This makes the photometry of sources directly comparable over the entire sky, and when combined with the previous requirement, creates a stable photometric system across the sky and over time, in a single filter.

3. **Band-to-band photometric calibration:** The absolute band-to-band zeropoint calibration for main sequence stars must be known with an rms accuracy of 5 millimags for any color not involving u band, 10 millimags for colors constructed with u band photometry. This requirement ties photometric measurements in different filters together, enabling precise measurement of colors, and allows LSST photometry to be compared with that from other optical telescopes, and with astrophysical models.
4. **Absolute photometric calibration:** The LSST photometric system must transform to an external physical scale (*e.g.* AB mags) with an rms accuracy of 10 millimags. This is essential for comparing with photometry from other wavelength regions, such as IR or UV.

Requirements 1 and 2 must be met by measuring and then correcting for changes in hardware and atmospheric transmission as a function of time, location in the sky or focal plane, and result in a relative calibration within a single filter. Requirements 3 and 4 require comparison of LSST measurements to externally calibrated spectrophotometric standards, providing a relative calibration from filter to filter as well as an absolute physical scale for the overall system. Performance of the LSST system regarding requirement 1 can be verified by simply measuring the rms of the calibrated magnitude measurements. Verification of requirement 2 is more complicated; in a simulated system it is simple to compare the (simulated, thus known) true magnitudes of the stars to the best-fit magnitudes produced after calibration. In operations, this will be verified using a combination of simulations, comparisons to known standards, and evaluation of science outputs such as stellar locus diagrams. These last two tests are also relevant to verifying the final two requirements, 3 and 4. These issues are discussed further in Sections 8 and 9.

3. The Photometric Calibration Process

In traditional photometric calibration, a set of standard stars is observed at a range of airmasses to calculate zeropoint offsets and (typically) a single color-dependent extinction curve per night. With care, this approach can deliver 1% photometry in stable photometric conditions. Such programs typically follow only a few objects, and devote roughly equal time to standards and program objects. This approach fails for a survey like LSST, for at least

two reasons. First, from a calibration point of view, the very wide field and multiple detector array mean that effectively a large number of instruments must be calibrated rather than just one. Second, historical weather data from Cerro Pachón tells us only 53% of the available observing time can be considered photometric even at the 1–2% level. To take advantage of the full 85% of the available observing time which is usable (total cloud extinction less than 1.5 magnitudes), and to reach the SRD specified requirements – 0.5% level photometric repeatability and 1% photometric uniformity – requires a new approach.

This new approach, first proposed by (Stubbs & Tonry 2006), *directly* measures the system throughput as a function of wavelength, focal plane position, and time. Further, the *normalization* of the throughput in each observation (the gray-scale zeropoint) and the *shape* of the throughput curve (the color dependent terms), are explicitly separated and measured with separate procedures for both the telescope system response and the atmospheric transmission. Calibration systems based on this approach are already in use at PanSTARRS and DES.

Several hardware systems are required to implement the approach. We briefly describe them here, with full descriptions in Section 7:

- A dome screen projector designed to provide uniform ($\sim 10\%$ variation) illumination across the field of view, while minimizing stray light. This projector system will have the capability to not only illuminate the screen with broadband white light, but also narrow-band light to measure the system response at individual wavelengths. The narrow-band light will be generated by a tunable laser, capable of producing light from 300 – 1100 nm and tunable in 1 nm increments. The brightness of the screen is measured with a NIST-calibrated photodiode, so that the relative intensity at different wavelengths can be precisely determined.
- A 1.2-m auxiliary telescope with an $R \approx 400$ spectrograph, located adjacent to the LSST itself. This auxiliary telescope will obtain spectra of a chosen set of atmospheric probe stars across the sky to determine an atmospheric absorption model.
- Water vapor monitoring system, consisting of a GPS system and a microwave radiometer copointed with the LSST telescope, and monitoring a similar field of view. This supplements the auxiliary telescope spectra, which are unable to track the sometimes rapid variations of water vapor in time and space.

An overview of the entire calibration process, from science observation to calibrated photometric measurements, together with the required calibration data products is shown in

Figures 1, 2, 3, and 4. Note that four classes of objects participate in the calibration process in different ways:

- Standard stars. These are stars whose absolute flux as a function of wavelength above the atmosphere is precisely known. This class contains only a few members, perhaps as few as ten. Their role is to enable the self calibration process to set absolute zeropoints for each band, and to allow testing of the SRD uniformity requirements. See Section 6.
- Calibration stars. These are stars that densely cover the sky, with typical spacings between stars of order 1 arcminute. Unlike standard stars, neither their SEDs nor their absolute fluxes are precisely known *a priori*, and their standard magnitudes are determined by the self calibration process. They have been selected to be on the stellar main sequence, to be nonvariable, and to be relatively isolated so that their photometry is not degraded by crowding effects.
- Atmospheric probe stars. These are bright stars of known type, distributed roughly uniformly over the LSST sky, which yield high SNR spectra from the auxiliary telescope.
- Science objects. Calibration of science objects utilizes the results of processing the standards and the calibration stars, and the measurement of the system bandpass. If an SED is supplied for an object, an accurate standard magnitude can then be calculated.

The following section will provide a more in-depth overview of the calibration process. We will start with a review of what is physically happening to photons in their path toward the focal plane, and then outline how LSST will translate the measured ADU counts back to fluxes above the atmosphere.

4. From Flux to Counts

We first consider how the photons from an astronomical object make their way to the detector and are converted into counts (ADUs), paying attention to the various temporal or spatial scales for variability might arise in the LSST system to affect the final ADU counts.

Given $F_\nu(\lambda, t)$ – the specific flux¹ (flux per unit frequency) of an astronomical object at the top of the atmosphere – at a position described by (alt, az) , the total specific flux from

¹Hereafter, the units for specific flux (flux per unit frequency) are Jansky ($1 \text{ Jy} = 10^{-23} \text{ erg cm}^{-2} \text{ s}^{-1}$)

the object transmitted through the atmosphere to the telescope pupil is

$$F_\nu^{pupil}(\lambda, alt, az, t) = F_\nu(\lambda, t) S^{atm}(\lambda, alt, az, t), \quad (1)$$

where $S^{atm}(\lambda, alt, az)$ is the (dimensionless) probability that a photon of wavelength λ makes it through the atmosphere,

$$S^{atm}(\lambda, alt, az, t) = e^{-\tau^{atm}(\lambda, alt, az, t)}. \quad (2)$$

Here $\tau^{atm}(\lambda, alt, az)$ is the optical depth of the atmospheric layer at wavelength λ towards the position (alt, az) . Observational data (Stubbs et al. 2007b; Burke et al. 2010) show that the various atmospheric components which contribute to absorption (water vapor, aerosol scattering, Rayleigh scattering and molecular absorption) can lead to variations in $S^{atm}(\lambda, t)$ on the order of 10% per hour. Clouds represent an additional gray (non-wavelength dependent) contribution to τ^{atm} that can vary even more rapidly, on the order of 2–10% of the total extinction at 1° scales within minutes (Ivezić et al. 2007).

Given the above $F_\nu^{pupil}(\lambda, alt, az, t)$, the total ADU counts transmitted from the object to a footprint within the field of view at (x, y) can be written as

$$C_b(alt, az, x, y, t) = C \int_0^\infty F_\nu^{pupil}(\lambda, alt, az, t) S_b^{sys}(\lambda, x, y, t) \lambda^{-1} d\lambda. \quad (3)$$

Here, $S_b^{sys}(\lambda, x, y, t)$ is the (dimensionless) probability that a photon will pass through the telescope’s optical path to be converted into an ADU count, and includes the mirror reflectivities, lens transmissions, filter transmissions, and detector sensitivities. The term λ^{-1} comes from the conversion of energy per unit frequency into the number of photons per unit wavelength and b refers to a particular filter, *ugrizy*. The dimensional conversion constant C is

$$C = \frac{\pi D^2 \Delta t}{4gh} \quad (4)$$

where D is the effective primary mirror diameter, Δt is the exposure time, g is the gain of the readout electronics (number of photoelectrons per ADU count, a number greater than one), and h is the Planck constant. The wavelength-dependent variations in S_b^{sys} generally change quite slowly in time; over periods of months, the mirror reflectance and filter transmission will

Hz⁻¹). The choice of F_ν vs. F_λ makes the flux conversion to the AB magnitude scale more transparent, and the choice of λ as the running variable is more convenient than the choice of ν . Note also, while $F_\nu(\lambda, t)$ (and other quantities that are functions of time) could vary more quickly than the standard LSST exposure time of 15s, it is assumed that all such quantities are averaged over that short exposure time, so that t refers to quantities that can vary from exposure to exposure.

degrade as their coatings age. A more rapidly time-varying wavelength-dependent change in detector sensitivity (particularly at very red wavelengths in the y band) results from temperature changes in the detector, but only on scales equivalent to a CCD or larger. There will also be wavelength-dependent spatial variations in S_b^{sys} due to irregularities in the filter material; these are required by the camera specifications to vary slowly from the center of the field of view to the outer edges. The equivalent bandpass shift can be no more than 2.5% of the effective wavelength of the filter. Wavelength-independent (gray-scale) variations in S_b^{sys} can occur more rapidly, on timescales of a day for variations caused by dust particles on the filter or dewar window, and on spatial scales ranging from the amplifier level, arising from gain changes between amplifiers, down to the pixel level, in the case of pixel-to-pixel detector sensitivity variations.

From equation 3 and the paragraphs above, we can see that the generation of counts $C_b(alt, az, x, y, t)$ from photons is imprinted with many different effects, each with different variability scales over time, space, and wavelength. In particular the wavelength-dependent variability (bandpass shape) is typically much slower in time and space than the gray-scale variations (bandpass normalization). These different scales of variability motivate us to separate the measurement of the normalization of S_b^{sys} and S^{atm} from the measurement of the wavelength-dependent shape of the bandpass.

4.1. Bandpasses and Associated Magnitudes

This then leads us to introduce a ‘normalized bandpass response function’, $\phi_b^{obs}(\lambda, t)$, that represents the true bandpass response shape for each observation,

$$\phi_b^{obs}(\lambda, t) = \frac{S^{atm}(\lambda, alt, az, t) S_b^{sys}(\lambda, x, y, t) \lambda^{-1}}{\int_0^\infty S^{atm}(\lambda, alt, az, t) S_b^{sys}(\lambda, x, y, t) \lambda^{-1} d\lambda}. \quad (5)$$

Note that ϕ_b only represents *shape* information about the bandpass, as by definition

$$\int_0^\infty \phi_b(\lambda) d\lambda = 1. \quad (6)$$

Using $\phi_b^{obs}(\lambda, t)$ we can represent the in-band flux at the top of the atmosphere for each observation as

$$F_b^{obs}(t) = \int_0^\infty F_\nu(\lambda, t) \phi_b^{obs}(\lambda, t) d\lambda, \quad (7)$$

where the normalization of $F_b(t)$ corresponds to the top of the atmosphere. Unless $F_\nu(\lambda, t)$ is a flat ($F_\nu(\lambda) = \text{constant}$) SED, F_b^{obs} will vary with changes in $\phi_b^{obs}(\lambda, t)$ due simply to

changes in the bandpass shape, such as changes with position in the focal plane or differing atmospheric absorption characteristics, *even if the source is non-variable*.

To provide a reported $F_b^{std}(t)$ which is constant for non-variable sources, we also introduce the ‘standardized bandpass response function’, $\phi_b^{std}(\lambda)$, a curve that will be defined before the start of LSST operations (most likely during commissioning). $\phi_b^{std}(\lambda)$ represents a typical hardware and atmospheric transmission curve, roughly minimizing the average difference between the varying $\phi_b^{obs}(\lambda, t)$ and the standard bandpass. Now,

$$F_b^{std}(t) = \int_0^\infty F_\nu(\lambda, t) \phi_b^{std}(\lambda) d\lambda, \quad (8)$$

is a constant value for non-variable sources.

We define a ‘natural magnitude’

$$m_b^{nat} = -2.5 \log_{10} \left(\frac{F_b^{obs}}{F_{AB}} \right) \quad (9)$$

where $F_{AB} = 3631$ Jy. The natural magnitude will vary from observation to observation as $\phi_b^{obs}(\lambda, t)$ changes, even if the source itself is non-variable. The natural magnitude can be transformed to a ‘standard magnitude’, m_b^{std} , as follows:

$$m_b^{nat} = -2.5 \log_{10} \left(\frac{F_b^{obs}}{F_{AB}} \right) \quad (10)$$

$$= -2.5 \log_{10} \left(\frac{\int_0^\infty F_\nu(\lambda, t) \phi_b^{obs}(\lambda, t) d\lambda}{F_{AB}} \right) \quad (11)$$

$$= -2.5 \log_{10} \left(\left(\frac{\int_0^\infty F_\nu(\lambda, t) \phi_b^{obs}(\lambda, t) d\lambda}{\int_0^\infty F_\nu(\lambda, t) \phi_b^{std}(\lambda, t) d\lambda} \right) \left(\frac{\int_0^\infty F_\nu(\lambda, t) \phi_b^{std}(\lambda, t) d\lambda}{F_{AB}} \right) \right) \quad (12)$$

$$m_b^{nat} = \Delta m_b^{obs} + m_b^{std} \quad (13)$$

$$\Delta m_b^{obs} = -2.5 \log_{10} \left(\frac{\int_0^\infty F_\nu(\lambda, t) \phi_b^{obs}(\lambda, t) d\lambda}{\int_0^\infty F_\nu(\lambda, t) \phi_b^{std}(\lambda, t) d\lambda} \right) \quad (14)$$

where Δm_b^{obs} varies with the *shape* of the source spectrum, $F_\nu(\lambda, t)$ and the *shape* of the bandpass $\phi_b^{obs}(\lambda, t)$ in each observation. Note that $\Delta m_b^{obs} = 0$ for flat (constant) SEDs, as the integral of $\phi_b(\lambda)$ is always one.

The natural and standard magnitudes can be tied back to the counts produced by the system by adding the correct zeropoint offsets. As Δm_b^{obs} removes all wavelength dependent variations in m_b^{std} ,

$$m_b^{std} = m_b^{inst} - \Delta m_b^{obs} + Z_b^{obs} \quad (15)$$

$$\equiv m_b^{corr} + Z_b^{obs} \quad (16)$$

$$m_b^{inst} = -2.5 \log_{10}(C_b^{obs}) \quad (17)$$

The zeropoint correction here, Z_b^{obs} , contains only gray-scale *normalization* effects, such as variations due to the flat field or cloud extinction. The SED corrected magnitude, m_b^{corr} , is the input to the Self Calibration block in Figure 1, and m_b^{std} is its output.

To summarize the various magnitudes utilized, and their associated fluxes:

- m_b^{inst} , the instrumental magnitude. $m_b^{inst} = -2.5\log_{10}(C_b^{obs})$, where C_b^{obs} are the instrumental counts (ADU) that are attributed to the object
- m_b^{nat} , the natural magnitude. This is the magnitude in the AB system that would be measured for the object if it were measured through the actual normalized system bandpass, $\phi_b^{obs}(\lambda)$, at the top of the atmosphere. This bandpass varies from exposure to exposure. See equations 7 and 9. $m_b^{nat} = m_b^{inst} + Z_b^{obs}$
- m_b^{std} , the standard magnitude. This is the magnitude in the AB system that would be measured for the object if it were measured through the standard normalized system bandpass, $\phi_b^{std}(\lambda)$, at the top of the atmosphere. This bandpass is selected as part of the survey design, and does not vary. See equation 8.
- m_b^{corr} , the SED corrected instrumental magnitude. This is the standard magnitude, but with an unknown gray zeropoint correction, which will be removed by self calibration. These magnitudes are the input to self calibration. $m_b^{corr} = m_b^{inst} + \Delta m_b^{obs}$

4.2. Perturbations to the System Bandpass

The normalized system bandpass will vary from exposure to exposure due to a myriad of effects. The major ones are:

- Atmospheric transmission variations. The major wavelength-dependent sources of atmospheric absorption, Rayleigh scattering from molecules, molecular oxygen lines, ozone, water vapor, and aerosols, all vary in time and space, with widely varying temporal and spatial scales. Even in the absence of intrinsic variation in the atmosphere, of course, the bandpass varies due to changing airmass. This latter effect is compensated for in traditional photometric calibration, but the others are generally ignored.
- Long term variations in the throughput of the optical path due to contamination
- Changing detector quantum efficiency, particularly in the y-band, due to varying focal plane temperature

- Shifts in filter position with respect to the system optical axis, due to positioning jitter and gravity sag

It bears repeating that every perturbation in general affects both the zeropoint, through the gray component of the perturbation, and the shape of the system bandpass, through the wavelength-dependent component. The gray component is removed by the self calibration process, while the wavelength-dependent component must be separately characterized and removed (see Figure 1). We are concerned here only about the latter effect, and discuss it for each of the above categories.

4.3. Effects of Airmass Variation

The effects of airmass variation on photometry is well known to all photometrists. In fact, it is the only effect which is always accounted for in photometric calibration, and quite often the only effect. Figure 5 shows the effects of variation over the full airmass range expected for the LSST survey. There is a more subtle effect, however, which is important because of the LSST’s large field of view: the airmass can vary significantly from one side of the field to the other. For example, if the field center is at airmass 2.1, the airmass varies from 1.98 to 2.22 across the field. Figure 6 shows the error that would be made in ignoring this effect. This requires us to maintain an atmospheric model which can be interpolated to any position in the focal plane.

4.4. Effects of Atmospheric Variations

The main components of wavelength-dependent atmospheric extinction are Rayleigh scattering from molecules; oxygen molecular lines; water vapor; ozone; and aerosols. Rayleigh scattering and molecular oxygen extinctions are directly proportional to barometric pressure at the surface. As is well known from looking at surface pressure charts, away from weather fronts the pressure varies significantly on timescales of hours or more and spatial scales of hundreds of km. Variations can be much more rapid in the vicinity of fronts. In any case, this component can be compensated for very accurately just by measuring the barometric pressure, and we do not consider it further here. The other components are not so easily measured, and in the case of water vapor and aerosols, can display complex patterns of variability.

Figures 7, 8, and 9 give three different perspectives on historical water vapor variability in the vicinity of CP. There are broad patterns in space (the E-W gradient), and in time

(the regular seasonal variations). There are large variabilities on top of these, amounting to several mm of PWV, which can occur in hours or less. The biggest effect of water vapor is in the y-band, since it contains a strong water band (Figure 47). Figure 10 shows the change in natural magnitude when the PWV is varied from 1mm to 6mm for a set of Kurucz stars. The 4mm variation in PWV shown in Figure 8 would lead to a roughly +/-3mmag color-dependent scatter in calibration of y photometry, if not compensated for.

While we do not have aerosol variability data for Cerro Pachon (CP), data from CASLEO, a site at 2550m in Argentina, serves as a reasonable proxy. Figure 11 shows the time history of aerosol optical depth at 675nm over a period of roughly a year. The spiky nature of the data is notable, suggesting rapid variations on timescales of perhaps a few hours. Figure 12, which shows a time-altitude profile of aerosol variations at a site in the US, backs up this impression. Although the site is at much lower altitude than CP, there are nonetheless significant variation of aerosol extinction at altitudes above 3000m on time scales well under an hour, and we should expect similar variations at CP. Determining the effects of aerosol variations on the system bandpass is more complex than for other atmospheric components, because the spectral shape of the aerosol extinction varies as well as its magnitude. Figure 13 shows the change in natural magnitude when the aerosol optical depth is varied from 0.04 mag to 0.16 mag, roughly the range of the CASLEO data, while keeping a constant spectral index of $\alpha = -1.7$. Unlike water vapor, which affected the reddest bands most strongly, aerosols affect the bluest bands the most. The effects in the u-band range from -5 mmag to +35 mmag, strongly dependent on star color.

Ozone is dominantly a stratospheric component of the atmosphere, and is routinely monitored by satellite. There is little evidence for variations on short time or space scales, with most variation periodic on a seasonal scale. Figures 14 and 15 shows the overall variability of ozone at CP over a roughly 8 year period. Figure 16 shows the changes in the natural magnitudes for a variation in ozone by 50 Dobson units. The effect is very small, except in the u-band, where it has a noticeable effect on red stars.

To summarize the effects of wavelength-dependent atmospheric variations, they are sufficiently large, and occur sufficiently rapidly, that they must be corrected by an atmospheric model with fidelity substantially greater than the traditional photometrist's extinction model. The combination of the auxiliary telescope and the water vapor monitoring system will supply the data required for construction of these atmospheric models. It is also worth emphasizing that correcting for these effects requires not only an accurate bandpass model, but also SEDs for the objects being calibrated. Calibration stars will be picked from well defined stellar populations to minimize SED uncertainty. SED determination for arbitrary science objects, such as supernovae and galaxies, will be more challenging, and may

limit the accuracy of their photometric calibration.

4.5. Throughput Variations Due to Contamination

The rates of contamination buildup on surfaces has been evaluated for both the telescope ((Krabbendam 2012)) and the camera ((Nordsby 2013)). Many contaminants have wavelength-dependent effects, so they will affect the system bandpass. The variation, however, is expected to be very slow, with a year being a typical timescale. These effects will be adequately measured by the collection of monthly monochromatic dome flats, as discussed in Section 5.1. We do not specifically account for them in the calibration uncertainty budget.

4.6. Variations in Detector Quantum Efficiency

The detector quantum efficiency as a function of wavelength varies with the detector temperature. The camera both measures and actively controls the temperature, but there is still variation on the order of 0.5 degK. The variation affects only wavelengths near the silicon bandgap at 1100 nm, and therefore only the y filter. Figure 28 shows the resulting effect.

4.7. Throughput Variations Due to Filter Position Shifts

The LSST filters are quite large interference filters, with diameter 75 cm. As manufactured, such filters always display some variation of the bandpass with position on the filter surface. This results in a system bandpass which is a function of position on the sky. Additionally, the LSST filters are exchanged by a mechanism which is not perfectly repeatable, and has some sag due to gravity. This results in a time-dependent variation of the filter position with respect to the telescope optical axis, leading to an additional bandpass variation.

Modeling of these effects is difficult due to the lack of knowledge of the detailed filter characteristics, which will not be available until they are manufactured. To do so in our simulations, we currently use a simple model that the filter bandpass has a shift which is a linear function of radius. The effect of a 1% bandpass shift on natural magnitudes is shown in Figure 29. It is worthy of note that this effect is large in all bands, so it must be carefully corrected in the calibration process.

4.8. Putting it All Together

Examples of the Δm_b^{obs} due to variations in the shape of the hardware and atmospheric response curves are shown in Figure 17 and Table 2. Two main sequence stellar models (Kurucz 1993) – one with temperature 35000K (blue) and one 6000K (red) – were combined with three different atmospheric response curves (with airmass $X=1.0$ with minimal H₂O vapor, $X=1.2$ with a nominal amount of H₂O (the ‘standard’), and $X=1.8$ with a large H₂O vapor content) and two different hardware response curves (one ‘standard’ and one shifted in wavelength by 1%) to illustrate the resulting changes in observed natural magnitudes. In Figure 18, the $X = 1.8$ atmospheric response is combined with a 1% shift (the maximum allowed in the filter manufacturing specification from center to edge) in filter bandpass, thus altering the hardware response, for many main sequence Kurucz models spanning a range of $g - i$ colors; the resulting changes in natural magnitudes are plotted. These examples demonstrate that the scatter in natural magnitudes induced by expected atmospheric and hardware transmission curve shape changes alone (without any gray-scale changes) can be much larger than the SRD repeatability requirements would permit. Roughly speaking, these effects reach a level of about 50 mmag. This suggests that our measurement-based model of wavelength-dependent effects must be accurate at the 90-95% level. This issue is discussed in detail in Section 8.

5. From Counts to Flux

The previous section laid out the origins of ADU count variability from one observation to another. Now we will consider how we can, in practice, acquire the information necessary to convert a particular observed ADU count to a measurement of $F_\nu(\lambda, t)$ above the atmosphere for a particular object. This requires measuring and then compensating for the variations in $S^{atm}(\lambda, alt, az, t)$ and $S_b^{sys}(\lambda, x, y, t)$. Let us first consider measurement of the variations in the hardware throughput curve, $S_b^{sys}(\lambda, x, y, t)$.

5.1. Measuring the Hardware Response

To measure the wavelength-dependent hardware response curve as a function of position in the focal plane, we will use a dome-screen system that is capable of producing narrow-band light over a range of wavelengths, producing a data cube of ‘narrow-band flat fields’. A

Table 1:: Δm_b^{obs} due to variations in system and atmospheric bandpass shape (see also Fig 17). The first two rows show the baseline ('standard') magnitude of the star. All other rows show the *change* in magnitude (in mmag) due to the variations listed at left. Any value larger than 5 mmag would be larger than the RMS scatter allowed by the SRD. *TODO color-code values larger than 5 mmag*

Bandpass	star	<i>u</i> (mag)	<i>g</i>	<i>r</i>	<i>i</i>	<i>z</i>	<i>y</i>
Std (X=1.2) atm, std sys	red	21.472	20.378	20.000	19.911	19.913	19.913
Std (X=1.2) atm, std sys	blue	19.102	19.503	20.000	20.378	20.672	20.886
		Δu (mmag)	Δg	Δr	Δi	Δz	Δy
Std (X=1.2), +1% sys shift	red	-31	-22	-8	-2	1	1
Std (X=1.2), +1% sys shift	blue	9	17	20	20	16	16
X=1.0, std sys	red	7	2	0	0	-0	-1
X=1.0, std sys	blue	-3	-1	-1	-0	1	-4
X=1.0, +1% sys shift	red	-24	-20	-8	-1	1	0
X=1.0, +1% sys shift	blue	7	16	19	20	18	12
X=1.8, std sys	red	-21	-10	-2	-0	0	1
X=1.8, std sys	blue	8	8	4	2	-1	6
X=1.8, +1% sys shift	red	-50	-30	-10	-2	1	2
X=1.8, +1% sys shift	blue	16	24	24	22	15	22

similar approach has already been employed at PS-1 ((Stubbs & Tonry 2012); (Tonry et al. 2012)), and at DES ((Marshall et al. 2013)). A series of steps is needed to convert this data cube into $S_b^{sys}(\lambda, t)$ at each x, y location in the focal plane:

- Determine and apply the monochromatic illumination correction (see Section 5.1.1)
- Normalize fluxes across wavelengths using the photodiode monitors
- Correct for pixel geometry

The resulting data cube then records (up to an overall normalization constant) $S_b^{sys}(\lambda, t)$ at each x, y location in the focal plane. Further processing constructs a synthetic field that will be used to flatten incoming science exposures.

We discuss each of these in turn.

5.1.1. Determining the Illumination Correction

As mentioned above, before dome flats (either broadband or narrow-band) can be used to measure S_b^{sys} , they must be modified to correctly produce *photometrically* uniform measurements of a collimated source across the field of view. This correction is called the ‘illumination correction’. The illumination correction must correct the observed flat fields for effects resulting from non-uniform illumination of the dome screen, for ghosting caused by internal reflections in the camera, and for the presence of stray or scattered light arriving in the focal plane on paths other than the direct image path (such as light bouncing from the dome floor or glinting off a filter holder). Figure 19 gives a perspective on the difference between the direct, total, and ghost flatfield illumination from a realistic model of the LSST telescope, camera, and domescreen illumination system.

The illumination correction is difficult to measure directly. To do so would require a collimated light source with diameter small compared with the telescope pupil that is able to scan in pupil position, angle, and wavelength. Aside from the engineering challenges in producing such a light source in the dome, the resulting 5-dimensional data cube would require an inordinate amount of time to collect, and we have deemed this approach impractical. Instead, we plan to combine data from several paths to generate an illumination correction which is consistent with all of them:

- Detailed monte carlo optics models, such as FRED
- Laboratory measurements of the as-built camera with the CCOB (see Appendix D). This provides the detailed data cube envisioned above, but only for the camera in isolation. This is sufficient to characterize ghosts, but not scattered light in the full system.
- Raster scans of star fields in photometric conditions. The star fields will be chosen to be dense, without compromising photometry due to crowding, and to contain a wide range of colors.
- Second order corrections from running self calibration. Self calibration is particularly capable at determining corrections which are position dependent but wavelength independent, such as arise from nonuniform illumination of the dome screen (see Figure 21).

This process will consume significant amounts of time in the lab, time on the sky, and time in analysis. Fortunately, the illumination correction is expected to be stable with time and will be remeasured only when components in the optical path of the telescope are altered.

Because the illumination correction is wavelength dependent (highly so near the edges of the filter bandpasses), its effect on photometry is dependent on the SED of the object in question. Figure 20 shows this effect as a function of both radius in the focal plane and star color, for a set of Kurucz main sequence stars. The effects are clearly too large to ignore, or they would overwhelm the uncertainty budget. This is discussed further in Section 8. It seems likely that the quality of the illumination corrections is currently limiting the photometric accuracy of large surveys, and we expect the LSST treatment of the illumination correction to yield significant improvement.

5.1.2. Normalizing Fluxes Across Wavelengths

The intensity of the monochromatic illumination source will vary with wavelength. This intensity will be accurately measured with a calibrated photodiode system that looks at the screen. Each wavelength slice of the data cube will be divided by the illumination intensity, so that the ratio of the data at any two wavelengths is the ratio of the system throughputs.

5.1.3. Correcting for Pixel Geometry

A pixel on the optical axis subtends more area on the sky than a pixel near the edge of the field. This results in an exposure of a uniform surface brightness source being brighter at the center than it is in the edge. This gradient, which can be precisely calculated from the optical prescription of the system, must be removed from the flats. If it were not, flattened science images would have the gradient removed, and the result would be systematic errors in the photometry of point sources, with a source at the edge being measured brighter than the same source on the optical axis.

5.1.4. Accounting For Finite PSF Width

Before we can discuss construction of the synthetic flat, we must take a brief detour and extend the discussion in Section 4. There, we implicitly assumed that the flux from an object is sampled at a single point in the focal plane. We must now extend the formalism to account for the fact that the system has a PSF with finite width, so that the flux from an object is spread over multiple pixels, each of which may differ slightly in response from its neighbors. Let us use i as an index over the pixels in the PSF for a particular object, and let w_i be the integral of the PSF over the area of pixel i , with $\sum_i w_i = 1$. To make the

notation compact, define

$$q_{b,i}(\lambda) = S^{atm}(\lambda, alt, az, t) S_b^{sys}(\lambda, x_i, y_i, t) \lambda^{-1} \quad (18)$$

Further, define the SED of the object, $f_\nu(\lambda)$ by

$$F_\nu(\lambda) = F_b f_\nu(\lambda) \quad (19)$$

where λ is within band b, and

$$\int_b f_\nu(\lambda) d\lambda = 1 \quad (20)$$

Then the total number of counts from the object, C_b^{inst} is

$$C_b^{inst} = F_b \sum_i w_i \int q_{b,i}(\lambda) f_\nu(\lambda) d\lambda \quad (21)$$

For compactness, let's define

$$Q_{b,i} = \int q_{b,i}(\lambda) f_\nu(\lambda) d\lambda \quad (22)$$

Since we are following the path from counts to flux, we are interested in

$$F_b = \frac{C_b^{inst}}{\sum_i w_i Q_{b,i}} \quad (23)$$

At this point, we notice that $Q_{b,i}$ is close to what we mean by a 'flat'. Let us make it identical, by factoring out the normalization, which is not directly measured:

$$Q_{b,i} = N Q_{b,i}^{norm} \quad (24)$$

where N is chosen to make $\max_i(Q_{b,i}^{norm}) = 1$. N will become the zeropoint of the exposure: $Z_b^{obs} = -2.5 \log_{10}(N)$.

There is a problem with using this flat, however: At the time we process the pixels in Flat SED Calibration (Figure 1), we are unable to calculate $Q_{b,i}$ because we are (probably) ignorant of both $f_\nu(\lambda)$ and the atmospheric bandpass for the observation, $S_b^{atm}(\lambda)$. Even

if we knew that information, this prescription would be unworkable because the flat would need to be constructed with an SED that varies rapidly over the focal plane. So we must accept our inability to work with $Q_{b,i}$ when processing the pixels, and must content ourselves with a broadband flat measured from the dome flatfield system.

$$Q_{b,i}^{BB} = \int q_{b,i}^{sys}(\lambda) f_\nu^{BB}(\lambda) d\lambda \quad (25)$$

where $f_\nu^{BB}(\lambda)$ is an SED we are free to choose in constructing the broadband flat. Note that $q_{b,i}^{sys}(\lambda) = S_b^{sys}(\lambda, x_i, y_i, t) \lambda^{-1}$ includes only the system response, not the atmosphere. We can now write

$$F_b = \frac{1}{N} \left[\frac{C_b^{inst}}{\sum_i w_i Q_{b,i}^{BB}} \right] \left[\frac{\sum_i w_i Q_{b,i}^{BB}}{\sum_i w_i Q_{b,i}} \right] \quad (26)$$

Expressed in magnitudes, this becomes

$$m_b^{nat} = m_b^{inst} + Z_p - 2.5 \log_{10} \left(\left[\frac{\sum_i w_i Q_{b,i}^{BB}}{\sum_i w_i Q_{b,i}^{norm}} \right] \right) \quad (27)$$

This may not at first seem like an advance over equation 23, but in fact it is: The first term on the RHS is just what we usually mean by measuring the flux in a flattened image. It is done at the pixel level in the usual way, without any dependence on $f(\lambda)$. We can at least imagine calculating the third, correction, term in exactly the way it is written. We do not need to actually access the image pixels, but do need to know the PSF and the object SED, and we need to construct at least a localized flat from the object SED. We reserve this as a future option in calibration processing, because it may reduce the systematics floor in the instrumental magnitudes. For the present, however, we make the assumption which is univerally made today in doing photometry, albeit almost always implicitly: The ratio of the true flat to the broadband flat is independent of the pixel within the PSF footprint, so that:

$$m_b^{nat} = m_b^{inst} + Z_p - 2.5 \log_{10} \left(\frac{Q_b^{BB}}{Q_b^{norm}} \right) \quad (28)$$

Note that the correction term must be applied in the "SED Correction" block of Figure 1. The required information to compute it is not available earlier. We now turn to the actual measurement of $q_{b,i}$, and the construction of $Q_{b,i}^{BB}$.

5.1.5. Constructing the Synthetic Flat

As discussed in the previous section, the choice of the SED used to construct the synthetic flats is largely arbitrary. It defines a reference SED $f_\nu^{BB}(\lambda)$, which must later be corrected for as shown in equation 28 when both the true $\phi_b^{obs}(\lambda)$ and the actual object SED, $f_\nu(\lambda)$ are known.

Given the arbitrariness of $f_\nu^{BB}(\lambda)$, we must choose on grounds of convenience. At least three choices suggest themselves:

- Choose $f_\nu^{BB}(\lambda) = const.$. This has the virtue of maximal simplicity.
- Choose $f_\nu^{BB}(\lambda)$ to be a flat SED at the top of the atmosphere, propagated through an average atmosphere.
- Choose $f_\nu^{BB}(\lambda)$ to be in some sense an average SED for all objects in the survey, propagated through an average atmosphere, such that the average value of the BBF correction is minimized.

We will initially choose the first of these. This choice may have unaccounted for impact on calibration accuracy, however, because the above formalism does not include the propagation of errors. We can readily change the prescription during construction or commissioning.

Generation of the entire data cube of narrow-band flats is too time-consuming to complete on a daily basis (the domescreen requirements allow 4 hours per filter, so 24 hours per set). Instead, the full narrow-band flat field scan will only be repeated on a time interval adequate for measurement of the more slowly variable components of $S_b^{sys}(\lambda, t)$, approximately monthly (but to be determined during commissioning). Since the system response can change on shorter timescales, principally due to a changing population of dust particles on optical surfaces, we correct the FSF nightly by multiplying by the ratio of two flats obtained with the broadband light source, one at the current epoch and one at the reference epoch when the narrow-band flats were acquired.

5.2. Measuring the Atmospheric Transmission

Next, considering $S^{atm}(\lambda, alt, az, t)$, we will again separate the measurement of the shape of the atmospheric response and the measurement of normalization of the transmission. The currently available data are still incomplete, but suggests that the wavelength-dependent variations in $\phi^{atm}(\lambda, t)$ change smoothly over spatial scales larger than the field of view

and over several minutes. By using an auxiliary telescope equipped with a spectrograph to observe bright stars with known SEDs, we can measure atmospheric absorption at a variety of positions in the sky every 5–10 minutes throughout the night. These observations are used as constraints for MODTRAN atmospheric models, generating representations of the atmospheric throughput in the form of a set of absorption components as a function of alt, az, t . These components can be interpolated in time and space to generate a wavelength-dependent atmospheric absorption profile, $\phi_b^{atm}(\lambda, alt, az, t)$, for each observation.

This approach has been put into practice by Burke et al. (2010). Probe stars were selected in the range $9 < V < 12$, and spectra were taken on a 1.5m telescope with a $R \approx 400$ resolution spectrograph covering a usable wavelength range of approximately $500 < \lambda < 1000nm$. Exposure times were 2 to 4 minutes. The observing pattern is shown in Figure 22. The atmospheric model was a simple linear combination of templates generated by Modtran4 for molecular scattering, molecular absorption, aerosols, ozone, and water vapor. The models, together with some factors to account for the spectrograph efficiency as a function of wavelength, were fit to all the observed spectra simultaneously. Figures 23 and 25 show some results. The fit to the individual spectra are impressively good, and the coefficients in the resulting atmospheric models show strong variation, as expected for the highly variable nights for which the data was obtained. Traditional extinction plots (Figure 24), show behavior that would be well fit by traditional calibration in the r- and i-bands, together with behavior in the z- and y-bands that would not. In subsequent development of the approach, Burke et al. (2013) obtained probe star spectra while simultaneously imaging over a wide field - roughly comparable to LSST operations. Unlike LSST, however, the imaging exposures were managed to keep the pixel coordinates of a given star nearly constant for all exposures. The full calibration process on the imaging data, including both atmospheric fitting and gray extinction determination through self calibration, yielded repeatability of approximately 8 mmag - good enough to meet the SRD minimum requirement for repeatability.

Using MODTRAN we can generate atmospheric transmission profiles at a variety of airmasses for each of these major sources of atmospheric extinction – molecular (Rayleigh) scattering, aerosol (Mie) scattering, and molecular absorption from each of O₃, H₂O, and combined O₂/trace species, as is shown in Figure 30 for a standard atmospheric composition (the 1976 US Standard). These profiles capture the wavelength dependence of each component individually, over a grid of airmasses, and can be used as templates to generate new atmospheric transmission curves for any desired atmospheric composition as follows:

$$\begin{aligned} S^{fit}(alt, az, t, \lambda) = & e^{-\tau_{aerosol}(alt, az, t, \lambda) X} \\ & \times (1 - C_{mol} (BP(t)/BP_o) A_{Rayleigh}(X, \lambda)) \\ & \times (1 - \sqrt{C_{mol} (BP(t)/BP_o)} A_{O_2}(X, \lambda)) \end{aligned}$$

$$\begin{aligned} & \times (1 - C_{O_3}(t) A_{O_3}(X, \lambda)) \\ & \times (1 - C_{H_2O}(alt, az, t) A_{H_2O}(X, \lambda)). \end{aligned} \quad (29)$$

The $A_{Rayleigh/O_2/O_3/H_2O}$ functions are absorption templates (i.e. 1 minus the transmission profiles from the MODTRAN models), the C_{mol,O_3,H_2O} are coefficients describing the composition of the atmosphere together with $\tau_{aerosol}$, and $BP(t)$ is measured. An example of an atmosphere generated in this fashion is shown in Figure 31, demonstrating that this method can be used to generate an atmosphere at any airmass for any composition desired, without needing to generate a full MODTRAN model.

With this capability, we can fit the auxiliary telescope spectroscopic data taken throughout the night for the values of C_{mol,O_3,H_2O} , increasing our SNR for these coefficients by modeling their expected behavior over time and across the sky. The Rayleigh scattering and molecular absorption due to O₂ and other trace species are fit with a single coefficient, C_{mol} , which simply scales the MODTRAN templates to the appropriate level for Cerro Pachon, and then only change with the barometric pressure (BP). The O₃ absorption is fit with a single C_{O_3} value for each night, as it is not expected to vary more than 5-10% within a night. The aerosol absorption, as it is expected to have a small spatial variation across the sky, is modeled as

$$\tau_{aerosol}(alt, az, t, \lambda) = (\tau_0 + \tau_1 \text{EW} + \tau_2 \text{NS}) \left(\frac{\lambda}{\lambda_0} \right)^\alpha, \quad (30)$$

where EW and NS are defined as $\text{EW} = \cos(alt)\sin(az)$, $\text{NS} = \cos(alt)\cos(az)$, projections of the telescope pointing in the EW/NS directions. Single values of τ_0 , τ_1 , τ_2 and α are fit for each night of observing, with τ_1 and τ_2 likely to be very small (Burke et al. 2010). The H₂O absorption is likewise expected to show spatial variation, but also time variability, and is modeled as

$$C_{H_2O}(alt, az, t) = C_{H_2O}(t) + \frac{dC_{H_2O}}{d\text{EW}} \text{EW} + \frac{dC_{H_2O}}{d\text{NS}} \text{NS} \quad (31)$$

using a constant spatial EW and NS gradient per night and a $C_{H_2O}(t)$ that is fit to each auxiliary telescope measurement (and interpolated between these times).

The coefficients $C_{mol/O_3/H_2O}$ and $\tau_{aerosol}$ will be determined using spectra of bright stars obtained from the 1.2-m LSST auxiliary telescope. The stars observed with the auxiliary telescope must be bright ($r < 12$) and ideally either white dwarfs or F stars – stars with relatively simple and well-understood SEDs to minimize confusion with the atmospheric extinction. By observing the same grid of stars on multiple nights, even if the SEDs are not well determined initially, they can be bootstrapped from the many epochs of data.

5.3. Estimating SEDs From Colors

Correcting for the color terms resulting from the difference between $\phi_b^{meas}(\lambda, t)$ and $\phi_b^{std}(\lambda)$ requires some preliminary measurement of the color of each calibration star (to within 0.02 magnitudes). This means we must either have some prior knowledge of the colors of each star (from Gaia, for example) or we must have some other method for measuring colors in the *ugr* bands relevant to determining metallicity and the color corrections detailed in Section 4.1, presumably by measuring the magnitudes of these stars in photometric data. Without this requirement, we could just combine all photometric and non-photometric data in the self-calibration routine, leaving the self-calibration solver to determine the appropriate δz_j to compensate for any non-photometric images.

Assuming that we must first identify and use photometric data to determine the colors of each object, this could proceed as follows. Identify all observations which were obtained in relatively photometric conditions by searching for images where the average scatter in magnitude measured for each source was less than some threshold (say < 0.05 magnitudes). Using these images and standard stars in these images, measure a preliminary color for each object. With this preliminary color, make a correction for Δm_b^{meas} and run the self-calibration solver for this (photometric) subset of the data. Iterate the results of the self-calibration solver to improve the color determination for each star, until the color measurement converges to within 0.02 magnitudes.

At this point, we have colors accurate enough to apply a Δm_b^{meas} correction sufficient to run self-calibration on all images, including the non-photometric data. There will be some data which is not calibrateable, due to a large amount of cloud extinction; these images will be identifiable by the low signal-to-noise ratio of the stars in the image.

5.4. Finding the Zero Points: Self Calibration

In order to correct for the more rapid gray-scale variations in the relative normalization of $S^{atm}(alt, az, t)$ due principally to cloud extinction, we must use the observations of calibration stars in the images themselves. This ‘self-calibration’ procedure could be thought of as creating a massive calibration ‘standard’ star catalog, where the calibration stars are a selected set of the non-variable, main-sequence stars in the science images; their main difference from true standards is that the true magnitudes of the calibration stars have to be bootstrapped from the many different observations of the survey, and their SEDs need to be inferred from multicolor photometry. For every calibration star, corrections for $\phi_b^{sys+atm}(\lambda, t)$ must be applied to produce a standardized magnitude, m_b^{std} , then in the self-

calibration procedure we minimize the difference between the standardized magnitude and a model magnitude,

$$\chi^2 = \sum_{ij} \left(\frac{m_{b,ij}^{std} - m_{b,ij}^{model}}{\sigma_{b,ij}^{std}} \right)^2 \quad (32)$$

where the model magnitude is derived from the best-fit ‘true’ magnitude of the calibration star and a model describing how we expect the magnitude to vary from observation to observation. In the simplest self-calibration plan, this model simply consists of a normalization constant (zeropoint offset) for a ‘patch’ equivalent to the size of a CCD,

$$m_{b,ij}^{model} = m_{b,i}^{best} - \delta z_{b,j}. \quad (33)$$

This produces best-fit magnitudes for the calibration star catalog as well as zeropoint offsets (normalization constants) for each CCD in every observation, allowing us to correct for atmospheric extinction on the scale of a CCD. By adopting a more complex model, this procedure can also correct for variations in the relative normalization of the total system throughput beyond those contributed by cloud extinction (such as remaining errors in the illumination correction for the broadband and narrow-band flat fields), but is generally limited by the number of stars and number of observations of each star that are obtained. A CCD size patch provides several hundred calibration stars per patch, allowing good signal to noise when determining cloud extinction which varies from observation to observation. This is similar in nature to the ubercal method applied to SDSS in Padmanabhan et al. (2008), and more recently DLS (Wittman et al. 2012) and PanSTARRS-1 (Schlafly et al. 2012).

Repeating Equation 15 above, adjusting *obs* indexes to *meas* to reflect the difference between the true and measured quantities,

$$m_b^{std} = m_b^{inst} - \Delta m_b^{meas} + Z_b^{meas} \quad (34)$$

we can relate the terms in this equation to the corrections just described above. Δm_b^{meas} originates from the difference between $\phi_b^{meas}(\lambda, t, x, y)$ and $\phi_b^{std}(\lambda)$ convolved with the source SED, and thus it depends on the shape of the total system response as well as the shape of the source SED. Δm_b^{meas} will be calculated by combining a series of model SEDs with $\phi_b^{meas}(\lambda, t, x, y)$ at various locations in the focal plane, creating a lookup table of values to apply to measured magnitudes. The Z_b^{meas} zeropoint offset comes from any normalization constants generated by the self-calibration procedure (in the simple model, just the $\delta z_{b,j}$ in equation 33 above).

These standard magnitudes are calibrated for variations in the observed bandpass shape (where applicable) and relative normalization, thus are directly comparable from one observation to the next. However, they are not yet tied to an external physical scale or from one

filter band to another, and thus only define an internally calibrated LSST magnitude in a particular filter.

To fulfill SRD requirements 3 and 4, these internally calibrated natural magnitudes must also be tied from one filter band to another, and then tied to an absolute external physical scale. For this, a further set of measurements is needed. In all filters, a set of spectrophotometric standards must be observed, and calibrated using the steps described above. Then the known SED is combined with the standard bandpass shape to generate synthetic color photometry. The synthetic colors are then compared with the calibrated measured standard magnitudes to calculate Δ_{b-r} , the corrections needed to tie measurements in each filter together (referenced to r band). At this point, only one final measurement is necessary to tie the entire system to an external physical scale: an r band LSST natural magnitude measurement of an absolutely calibrated source on a photometric night. Although in theory these last two steps could be done with a single externally calibrated object, on a single photometric night, a larger set of external reference objects with well known AB magnitudes will be used to reduce systematic errors. This defines an AB magnitude,

$$m_b^{AB} = m_b^{std} + \Delta_{b-r} + \Delta_r \quad (35)$$

which can be compared to absolute physical flux scales.

This self-calibration procedure can be successful only if patches overlap on the sky, so that the same star is observed on multiple patches. This means complete sky coverage is necessary to link all stars together into a rigid system, but also indicates that some amount of dither is required. Our investigations have shown that dither patterns where the overlap is one quarter of the field of view or more produce results meeting the SRD requirements.

Note that $m_{b,i}^{best}$ and $\delta z_{b,j}$ are constrained only up to an arbitrary additive constant. For convenience, this constant can be set so that stars have roughly correct AB magnitudes, however the goal after self-calibration is primarily to have a rigid, self-consistent magnitude system, equivalent to the natural magnitudes. Accurately calibrating the internal magnitudes to an external scale is discussed in Section 6.

5.5. Calibration Operations

The sequence for photometric calibration is then:

1. Acquire the data cube of narrow-band flat field images, approximately monthly. Determine and apply wavelength-dependent illumination correction. Measure $\phi_b^{sys}(\lambda, t, x, y)$.

Note that the time required to acquire these flats is required to be less than four hours per filter, so a full set of filters requires 24 hours.

2. Acquire a broadband flat in each filter at the start of each observing night. Generate the flats which will be used for the night’s images by scaling each synthetic broadband flat by the ratio of tonight’s broadband flat to the reference broadband flat (Section 5.1.5). These flats will also be used to do a nightly camera gain calibration.
3. After performing usual mosaic image processing (bias correction, fringe correction, flattening, etc) extract ADU counts of sources from images.
4. Acquire spectra of known stars roughly every 5–10 minutes throughout each night, fit for atmospheric absorption coefficients and generate $\phi_b^{atm}(\lambda, t, az, el)$ for each science images.
5. Combine ϕ_b^{atm} and ϕ_b^{sys} with a range of model SEDs to create lookup tables for Δm_b^{meas} for various locations in the focal plane, and store these as a data product
6. At every Data Release, run the self-calibration procedure, applying Δm_b^{meas} to stars chosen for self-calibration procedure and minimizing χ^2 from equation 32.
7. Apply appropriate Z_b^{meas} and Δm_b^{meas} to all objects in Data Release catalog, producing standardized magnitudes.
8. Apply measured corrections Δ_{b-r} and Δ_r , producing absolutely calibrated magnitudes.

This results in calibrated m_b^{AB} values in a standardized bandpass shape, with above-the-atmosphere fluxes.

6. Fixing LSST to an external scale

The next two subsections describe how the internally calibrated standard magnitudes, independently calibrated in each filter bandpass, are fixed to an external scale such that the flux in a single band can be compared to the flux in another filter band (SRD requirement 3) and that the flux in a particular filter band can be compared to an absolute external system (SRD requirement 4). This is equivalent to determining Δ_{b-r} and Δ_r from Eqn 35. In practice, the same standards will be used for both tasks, and we discuss them together.

Both the band to band calibration for each filter b (the Δ_{b-r} values) and the absolute calibration of Δ_r will be determined by measuring the flux from standards. Ideally these

would be standard sources placed above the atmosphere, but in practice must be celestial objects whose SEDs across the LSST wavelength range are precisely measured and/or predicted by physical models, and which are contained in the LSST survey fields. Although in principle a single standard with known colors would be sufficient, the major concern here is with systematic errors, for example a variation in color calibration across the sky induced by say seasonal and/or directional variations in water vapor and aerosol content. Our current simulations (Section 9) show significant spatial patterns in photometric zeropoints. Monitoring and controlling these systematics will require a larger set of standards.

These fall into three groups:

- DA white dwarfs observed with HST. Relatively few in number, these form the "gold standard" for the survey, and include not only the three fundamental standards ((Bohlin & Gilliland 2004a)) that are used to calibrate instruments on board the HST that is self-consistent to better than 5 milli-mag, but also a growing set from the HST program GO-12697 of Saha et al, for which observations are still underway.
- DA white dwarfs for which accurate spectroscopic determination of T_{eff} , g , and interstellar reddening are available.
- Stars observed with Gaia. By roughly 2020, when LSST will be in commissioning, Gaia will achieve 1mmag photometry in the Gaia G band for a large set of stars with $V < 18.5$ ((Jordi et al. 2010)). If the Gaia G magnitudes can be accurately transformed to the LSST bands, we will have a very large set of absolute standards. This transformation is conceivable, because Gaia produces low resolution spectra for every object. We are currently investigating the photometric accuracy that can be achieved, and do not yet intend to rely on Gaia photometry for calibrating LSST.

Additionally, the main sequence stellar locus can be used to check for systematic errors in photometry.

6.1. White Dwarf Standards

DA white dwarfs have atmospheres dominated by hydrogen, and thus are the simplest stellar atmospheres to model. The opacities are known from first principles, and in the temperature ranges we are interested in, photospheres are purely radiative and photometrically stable. The emergent fluxes from such an atmosphere can be defined by just two parameters: effective temperature and a surface gravity, which only require a flux normalization at

some wavelength. These parameters are easily determined spectroskopically from a detailed analysis of the H I Balmer profiles, without reference to any photometry. Thus the entire spectral energy distribution (SED) from the UV to the IR can be calculated at arbitrary spectral resolution and folded through any well determined photometric band pass or spectroscopic system. The primary example of such an effort is Holberg & Bergeron (2006), where synthetic photometry of DA white dwarfs was used to place *UBVRI*, 2MASS *JHK*, SDSS *ugriz* and Stromgren *uby* magnitudes on the HST photometric scale to 1% using a consistent set of photometric zero points and magnitude offsets. A fundamental independent check on this photometric calibration was established by using a set of DA white dwarfs having good trigonometric parallaxes and calculating the corresponding photometric parallaxes from the Bergeron photometric grid (Holberg et al. 2008). The two parallaxes agreed at the 1%.

This idea has been quantitatively tested with HST/STIS spectroscopy (Bohlin 2000), who observed 4 bright DA white dwarfs spanning a range of temperatures and unaffected by reddening (due to their proximity to us), and found their relative flux distributions to be internally consistent with model predictions (Finley et al. 1997) from spectroscopic T_e and $\log g$ to better than 1% in the wavelength range $0.2 - 0.9\mu$. Spectrophotometry of Vega with STIS (Bohlin & Gilliland (2004b), Bohlin (2007)) referred to the DA white dwarf (WD) flux scale shows agreement with the Hayes et al. (1985) calibration at the 1 to 2% level, and with the Kurucz (2003) Vega atmosphere model to better than 1% in the wavelength range $0.5 - 0.8\mu$. This seems to indicate that in the visible region, the Kurucz model is a better predictor of the flux from Vega than the ground based comparisons to standard sources. The WD based calibration disagrees with Hayes (1985) by 5% at 0.4μ , and by 10% between 0.9 and 1.0μ . The 9400K Kurucz model for Vega agrees with the STIS observations of Vega tied to the WD scale to $\sim 2\%$ from 0.28 to 1.0μ . We surmise that 1) outside $0.5 - 0.8\mu$, the atmospheric extinction is a real hindrance to setting up calibrators, and 2) the self-consistency of the WDs is better than the comparison with the best *model* for Vega, verifying that the WD modeling is superior to that for A stars, and validating the assertion that DA white dwarfs are best understood as standard SEDs. The calibration in place for HST instruments relies on Vega for the flux at 555.6μ : fluxes relative to this wavelength are determined by 3 (4 are available) primary WD models.

For LSST, it is desirable to have a larger set of calibrated DA white dwarfs which are faint enough to be unsaturated in the regular survey observations. Ideally there should be at least 3 of them visible in the sky at any time spanning a range of airmass and direction. However, DA white dwarfs fainter than 17th mag in general suffer some reddening, which must therefore be determined in addition to T_{eff} and $\log g$. The HST program GO-12697 (PI: Saha) is photometrically measuring a set of 9 such DA white dwarfs near the equator

and distributed in RA with ACS on board the HST. This photometry will be on the gold standard of the three white dwarfs that define the HST absolute scale, and systemically accurate to within 10 mmag. The program is also obtaining high S/N spectra with the Gemini telescope(s) to determine accurate T_{eff} and $\log g$. Comparison of the photometric colors, and the model SED will then yield the reddening, and thus render the object as an SED standard. To date only 2 of the 9 objects have been observed by HST, while the Gemini spectroscopy is farther along. A proposal to augment the targets to span non-equitorial declinations in a follow up proposal in the HST cycle was rejected by their TAC.

In addition to the selectively crafted effort described above, it is estimated that there will be $\approx 100/10$ DA/DB WD stars with $r < 24$ in each LSST image at the South Galactic Pole, though few of these will have available the spectra necessary for synthetic photometry. At least 100–1000 across the sky will be used to search for systematic effects. Catalogs of WD stars visible from Cerro Pachon have been constructed.

6.2. Population Methods

An alternative approach to using a small handful of precisely known standards is to use the properties of entire populations of astronomical objects.

The locus of main sequence stars in color-color space is also reasonably well understood and has been used to calibrate photometric colors with success in previous surveys (MacDonald et al. 2004; Ivezić et al. 2007; High et al. 2009). The use of the main sequence stellar locus in addition to WD stars will provide a valuable check on systematic effects that may arise from using (primarily) white dwarfs in the determination of $\phi^{atm}(\lambda, alt, az, t)$, as white dwarfs are bluer than most of the main sequence stars used for the bulk of the remainder of the calibration procedures.

Additional checks on the quality of color calibration will be based on color residuals when determining photometric redshifts for galaxies. Analyzing these residuals as a function of galaxy brightness and color, and across the LSST footprint, will yield detailed quantitative estimates of the calibration quality.

6.3. Computational Technique for Determining Δ_{b-r}

The values for Δ_{b-r} will be determined by generating model m_b^{std} values for each band-band calibration object, then minimizing

$$\chi^2 = \sum_i \left(\frac{(m_{b,i}^{std} - m_{r,i}^{std})^{meas} - (m_{b,i}^{std} - m_{r,i}^{std})^{model}}{\sigma_{b-r,i}} \right)^2. \quad (36)$$

This comparison can be done using subsets of objects from low Galactic extinction regions, and then bootstrapping to the entire sky to check for systematic effects.

After determining the band to band calibration, there is one further value required to calibrate the entire system to an absolute flux scale: Δ_r . This could again be determined using a single object with a well-known flux and spectral energy distribution, however multiple external calibrators provide a valuable check on systematic effects.

7. Calibration Hardware

7.1. Flat Field Illumination System

The flat field illumination system is designed to illuminate the dome screen with a uniform flood of either broadband or tunable narrowband light. A precision photodiode measures the intensity of the illumination. The requirements for the flat field illumination system are in (Sebag & Krabbendam 2013). The overall goals are very similar to the DECal system used for the Dark Energy Survey ((Marshall et al. 2013)), but due to the larger telescope aperture, and more compact dome, is designed somewhat differently. The overall design is shown in Figure 52.

7.2. Auxiliary Telescope

The role of the auxiliary telescope in the calibration process was described in Section 5.2. The requirements for the auxiliary telescope are in Sebag and Krabbendam ((Sebag & Krabbendam 2013)). We will use the refurbished Calypso telescope, which will be moved from Kitt Peak to Cerro Pachon. It has a 1.2 meter diameter F/18 primary mirror, with instruments at the Nasmyth focus. Figure 50 shows the siting of the auxiliary telescope in relation to LSST, and Figure 51 shows the auxiliary telescope itself.

The auxiliary telescope will be instrumented with a spectrograph covering the wavelength range of 400 to 1125 nm at a resolution of approximately 400. Exposure times for

typical atmospheric probe stars to obtain $SNR \approx 200$ are estimated to be between 60 and 250 sec. Its operation will be automated, and under the control of the LSST Scheduler. Generally, the auxiliary telescope will *not* observe stars along the same line of sight as LSST, for two reasons: First, it requires exposure times roughly ten times longer than LSST, so it would rapidly get left behind. Second, the values for $C_{mol/O_3/H_2O}$ and $\tau^{aerosol}$ are better constrained by observing a wide variety of airmasses and locations on the sky that cover a wide range in N/S/E/W directions, as well as utilizing repeat observations of the same star throughout each night, and then fitting the spectroscopic data from the entire night. This improves the signal to noise for the atmospheric absorption profiles generated for each science observation.

7.3. Water Vapor Monitoring System

As discussed in Section 4.4, water vapor can potentially vary on spatial and temporal scales that will not be adequately sampled by the auxiliary telescope. Because y-band photometry is so sensitive to water vapor (PWV), the LSST has a dedicated system to monitor it. The system has two components

- A GPS system that measures an all sky value for PWV. This system operates continuously, whether the LSST is observing or not, and forms part of the site’s complement of weather instruments.
- A microwave radiometer optimized for measuring PWV that is copointed with the LSST, so that a PWV measurement is available for every exposure.

Both of these system components are well tested in astronomical applications, and are relatively inexpensive (Blake & Shaw (2011), Radomski et al. (2010), Gaffard & Hewison (2003)). Their data will be logged through the Engineering and Facility Data Base.

7.4. Camera System Telemetry

The calibration process relies on measurements collected by the camera system on a per-exposure basis, and stored in the Engineering and Facility Database. The measurements directly utilized are:

- focalplane temperature

- shutter travel time
- gain for each amplifier

There is a much wider range of available information, and we have the option to mine it to understand and compensate for systematics in the system.

8. Calibration Error Budget

Many sources of errors feed into the calibration process. It is a challenging task to identify and quantify all of them, and we have not yet completely done so. We present our current estimates here, but they are subject to change as our analysis improves. We first discuss repeatability errors, and then uniformity errors. The band-to-band, and absolute calibration errors flow directly from the characteristics of the standard stars, and have already been discussed in Section 6.

8.1. Repeatability Errors

The repeatability error in m_b^{std} for individual calibration stars must meet the requirement in the SRD (Requirement 1 in Section 2). The contributions to this error are best discussed in the context of Figure 1. If we recall that

$$m_b^{std} = m_b^{inst} - \Delta m_b^{obs} + Z_b^{obs} \quad (37)$$

it is natural to divide the error sources into three categories:

- errors in m_b^{inst} , determined by Flat SED Calibration
- errors in Δm_b^{obs} , determined by SED Correction
- errors in Z_b^{obs} , determined by Self Calibration

We will assume that the errors in these terms are uncorrelated, and add in quadrature to produce the overall error.

8.1.1. errors in m_b^{inst}

As sketched in Figure 1, m_b^{inst} is produced by the LSST Data Management System (DM), through processing raw science exposures. Leading error contributions come from the flat spectrum flat (modulated by position and PSF changes of the star on the focal plane), sky background subtraction, and the photometry algorithm used to extract source counts from the flattened and sky-subtracted image. We do not attempt to quantify those individual contributions here, in good part because the relevant software is still early in its development process within DM. Rather, we note that photometric errors, considered as a function of stellar magnitude, always display a systematics floor at the bright end. The contribution of this error to repeatability can not be reduced by any part of the subsequent calibration process, and adds in quadrature to the repeatability error estimate. The estimate from DM is that this error floor will be 3mmag.

8.1.2. errors in Δm_b^{obs}

As shown in Section 5, Δm_b^{obs} is a function both of the system bandpass, ϕ_b^{obs} , and the SED of the object, $F_\nu(\lambda, t)$. It is affected by the following errors:

- errors in the atmospheric bandpass, S^{atm}
 - errors induced by measurement noise in atmospheric probe instruments (auxiliary telescope; water vapor monitoring system)

Measurement errors from the water vapor monitoring system are expected to be $\pm 1\text{mm}$. Making use of the plots in Figure 10, which is for a variation of 5mm, this translates to errors of 0.2 mmag in u-band, negligible in g,r, and i-bands, 1 mmag in z, and 2mmag in y.

We do not yet have reliable error levels for aerosols and ozone. Based on the data from Burke et al. (2010), we estimate that the errors are no more than 10% of the total variation seen in each of those components, RSSed together. Figures 35 and 36 show that the resulting errors are roughly 1.6 mmag in u-, 2.1 in g-band, 0.1 in r, and negligible in all other bands.
- Unmodelled spatial and/or temporal variation of atmospheric components, particularly aerosols

The water vapor extinction is measured along the LSST’s line of sight by the co-pointed microwave radiometer, so it is not subject to this errors. For aerosols we

again take 10% of the total variation seen. This gives 1.4 mmag in u, 0.7 mmag in g, and negligible for others.

- errors in determination of monochromatic illumination correction, which propagate directly into errors in S_b^{sys} .

If the monochromatic illumination correction is ignored, the resulting errors in Δm_b^{obs} are shown in Figure 20. The maximum effect is roughly 15mmag in u-band and 3mmag or less in the other bands. As discussed in Section 5.1.1, we will determine the illumination correction from a combination of modelling and dedicated measurements. While the accuracy of the result is difficult to assess in advance, we conservatively assume that the error will be 20%. This results in an error contribution of 3mmag in u-band, and 0.6mmag in the others.

- Wavelength-dependent errors in measurement of the domescreen intensity by the photodiode monitor. This will result in errors in combining the monochromatic domeflats to determine S_b^{sys} .

A photodiode monitor for this purpose was first employed by Stubbs on the Blanco telescope at CTIO ((Stubbs et al. 2007a)), and an error analysis was undertaken in (Stubbs et al. 2010) . We are sensitive to systematic errors in the photodiode response rather than to noise, which can be effectively averaged over. Figure 46 estimates the level of these systematic errors as 2 mmag at 400nm, 1 mmag between 470 and 950nm, and increasing beyond 950nm to 10 mmag. Figure 46 shows the effects on Kurucz SEDs of a randomly chosen systematic error curve that conforms to these levels. The effects are negligible in all but the u-band.

- errors in determining the SEDs of calibration stars from their multicolor photometry.

In practice, Δm_b^{obs} for a calibration star will be determined by looking up its SED as a function of a set of colors formed from the 6 band magnitudes, and then integrating against the system bandpasses ϕ_b^{obs} and ϕ_b^{std} according to equation 14. The SEDs will come from some model of main sequence (MS) stars (we have been using Kurucz in our work). Real stars deviate from the canonical main sequence (MS) locus, however, due to many causes. Intrinsic widths of the MS color-color locus are generally estimated to be on the order of 20mmag ((Ivezić et al. 2007; High et al. 2009)). This translates directly into an error in Δm_b^{obs} . For example, if we use Figure 18 as an indication of the maximal expected values of Δm_b^{obs} , we can multiply the maximum slope in each band by 20mmag to get an estimate of the effect. The values of the maximum slopes are roughly: 0.28 (u), 0.04 (g), 0.02 (r), 0.02 (i), 0.02 (z), 0.01 (y). This leads to the values in Table 3. This error source is negligible for all but the u-band, where it contributes

significantly to the error budget. It is likely that a more careful choice of SED models can reduce this error term.

- Effects of contamination buildup between monochromatic domeflats

Still TBR. This will likely determine the required frequency of taking monochromatic domeflats

- Effects of errors in focal plane temperature on wavelength-dependent detector QE

The detector QE at wavelengths near the red cutoff is affected by temperature, with higher temperatures resulting in higher QE. The focal plane temperature is monitored by the camera, allowing the temperature at any point on the focal plane to be predicted to 0.5 K with respect to the reference condition when the monochromatic dome flats were obtained. Figure 28 shows, as expected, that the effect of that prediction error on the natural magnitudes is negligible for all but the y-band, where it is 0.2 mmag. There is, of course, a larger effect on the zeropoints, discussed below.

- errors in filter bandpass due to variation in position with respect to the optical axis

Figure 29 shows the effects of shifting the filter bandpass by 1% of the central wavelength. The effect varies with the filter band, but an ensemble of stars of varied color will show an increased scatter of roughly 40 mmag. The LSST filter requirements permit a 2.5% shift in the bandpass from center to edge, and require a smooth variation. Assuming that variation is linear, a shift in the filter position by δR mm, results in a bandpass shift

$$\frac{\delta\lambda}{\lambda} = \frac{0.025 \delta R}{325} \quad (38)$$

The resulting magnitude scatter, in mmag, is then

$$\delta m \approx \frac{50}{0.01} \frac{\delta\lambda}{\lambda} \approx 0.30 \delta R \quad (39)$$

If we require that the effect be no more than 0.5 mmag, $\delta R < 1.6$ mm. The camera requirement for filter position knowledge is chosen to meet this photometric requirement.

8.1.3. errors in Z_b^{obs}

Every exposure has a spatial zeropoint model determined by Self Calibration as the solution to a large linear least squares problem, as discussed in Section 5. The errors in the zero points are dependent on the spatial scale of the perturbations, as one can see from a

simple argument. One can reasonably expect that Self Calibration will determine the true magnitudes of the calibration stars with an error that is well below the repeatability requirement ($\sigma \approx 5 \text{ mmag}$) for individual measurements, so for present purposes we ignore the errors in the true magnitudes. Suppose a perturbation shifts, for a single exposure, the zeropoint over an area A by some constant δZ . If that area contains N calibration stars, each provides an estimate of δZ with an error of σ . The full set of calibration stars, assuming that their measurement errors are uncorrelated, allows δZ to be estimated to a precision of $\sigma_{\delta Z} = \sigma/\sqrt{N}$. The density of calibration stars varies over the sky. Here we will use a mean value of 2 arcmin^{-2} , which corresponds to stars in the range $20 > V > 18$ at Galactic latitude of 30 degrees. This provides the following rough estimates for spatial scales of relevance:

- Detector segment: $A = 11 \text{ arcmin}^2$, $N \approx 22$, $\sigma_{\delta Z} \approx 1 \text{ mmag}$
- Detector: $A = 178 \text{ arcmin}^2$, $N \approx 356$, $\sigma_{\delta Z} \approx 0.25 \text{ mmag}$
- Focalplane: $A = 3.4 * 10^4 \text{ arcmin}^2$, $N \approx 6.8 * 10^4$, $\sigma_{\delta Z} \approx 0.02 \text{ mmag}$

This makes it clear that the size of a detector segment is a rough boundary, above which zeropoint errors should be negligible, while below it they may become quite significant.² This expectation is confirmed by our simulation results, as shown in Figure 38. These runs, for the r-filter, have no color dependent errors, and data is plotted only for zeropoint errors less than 100 mmag (the fat tails extend further). The zeropoint errors after self calibration saturate at a level independent of the input zeropoint perturbations, and the saturation level is approximately $\sigma_{sat} = \sqrt{(\sigma_1^2/N + \sigma_{sys}^2)}$ where $\sigma_1 \approx 3 \text{ mmag}$ and $\sigma_{sys} \approx 0.7 \text{ mmag}$.

Zeropoint errors obey the approximate relation above only when they are relatively small. If they become large enough to dim the calibration stars significantly, the reduction

²In reality, many zeropoint perturbations (such as clouds and focal plane temperature variations) have a continuous spatial power spectrum, and a more sophisticated estimate is required. This estimate can be provided through "objective analysis", a formulation developed by the oceanographic and meteorological communities, and based on the Gauss-Markov theorem ((Bretherton et al. 1976), (Bretherton & McWilliams 1980),(McIntosh 1990)). The problem addressed by objective analysis is: Given a continuous scalar field, measured in a two dimensional domain at a set of points, what is the optimal estimator for values of the field throughout the domain, and what is the expected error of that estimator? In our application, the scalar field is the zeropoint, and there are (noisy) measurements of it at the position of each calibration star in the field. The formalism allows the error to be predicted based on the measurement errors and the structure function of the field. Figure 40 shows an example result using a realistic cloud structure function, with characteristic length scale of 500 meters, which is at the short (and more stressing) end of what we expect. This development has just begun, but it will offer an independent check of the simulation results. Early results show consistency between the two methods.

in their signal-to-noise ratio increases the errors that come out of Self Calibration. This is shown in Figures 41, 42 and 43, which present the results of a self calibration simulation, again without color-dependent effects. As the first of these figures illustrates, the zeropoint error has the shape of a fan in (zp , zp -error) space, with the width of the fan increasing as the input zeropoint increases. The other two figures, which are cross sections of the fan at different zeropoint levels, show that the error distribution is roughly a gaussian core with fat tails. When the zeropoint is between 0 and 0.5 mag, the gaussian sigma is only 1 mmag. Under extinction conditions near the limit at which we propose to continue survey operations, between 1 and 1.5 mag, the gaussian core has a sigma of 30 mmag.

In practice, zeropoint variations are dominated by clouds, with smaller effects described below. The impact of these variations on calibration performance as a whole will depend strongly on the pdf of the cloud extinction, as the above results show. The strength of this dependence derives partly from the fact that the standard deviation in cloud extinction is roughly proportional to the extinction itself. Additionally, increasing extinction increases the photometric errors in the measurements of the calibration stars. Our current estimate for the cloud extinction pdf is based on rather crude data from CTIO, and is shown in Figure 39 for the r filter. Averaged over all filters and the full survey, this data suggests that the extinction should be less than 0.5 mag for approximately 94% of the observations. The higher extinction data therefore comfortably falls within the 10% fraction of the data excludable from the repeatability requirement by the SRD.

Other perturbations to the zeropoints arise from:

- Varying gray averages of extinction from aerosols, water vapor, and ozone. These are dominated by aerosols, and have spatial scales large compared to a detector.
- Camera gain variation. This is constrained by Camera requirements to be less than 1 mmag rms over a 1 hour period, and less than 10 mmag over 12 hours. These gain variations occur at the detector segment level.
- Shutter travel time variation. Camera requirements constrain this to 20 mmag. The effects are over spatial scales comparable to the size of the focal plane
- Detector QE variation due to varying focal plane temperature. These occur over full detectors, affect only the y-band, and knowledge of them is constrained by Camera requirements to be better than 0.5 K. This results in a 1 mmag zeropoint perturbation.

In summary, for the 90% of the survey observations with cloud extinction less than 0.5 mag, we expect the zeropoint errors to be dominated by perturbations that act at the

detector segment scale. It is prudent to expect that the resultant errors will be at σ_{sat} for that scale, the saturation level determined above. For typical detector segment size areas on the sky, these contain roughly 20 stars, and $\sigma_{sat} \approx 1$ mmag. Some segment areas will have substantially less, however, leading to increased $\sigma_{sat} \approx 2$ mmag. To be conservative, we carry this latter value in our error budget. The error budget for repeatability errors, including all of the above effects, and for the above specified 90 % fraction of the survey, is summarized in Table 3.

8.2. Uniformity errors

Uniformity errors must meet the uniformity requirement in the SRD (Requirement 2 in Section 2). Nonuniformity can arise from systematic errors in either Z_b^{obs} , Δm_b^{obs} , or both. These in turn tend to arise from the combination of two factors: systematic patterns across the sky in stellar populations, and the way they are observed by the survey (sky systematics); incompletely modelled systematic variation of the system bandpass with respect to focalplane position and/or color (system systematics).

There are several sources of sky systematics:

- errors in standards. Because standards are relatively sparse on the sky (Section 6), an error in the flux of a single standard can create significant nonuniformity in the overall calibration in the area of the sky which is near to it.
- Systematic variation of calibration star properties across the sky, in color or in more subtle effects on the SEDs, for example from interstellar reddening.
- Unmodelled systematic variations in the atmosphere. These can include persistent patterns in cloud extinction or wavelength-dependent atmospheric components, such as aerosols. These are especially pernicious when they exhibit a N-S dependence.

Two examples of sky systematics are shown in Figures 44 and 45. In the first of these, the survey’s dither pattern leaves intact a pattern of varying radius on the focalplane. In the second, there is systematic variation over the sky of cloud extinction (likely unrealistic).

Turning to system systematics, we discussed many causes for varying system bandpass in Section 8.1, and several of these can act as the second factor in generating nonuniformity:

- Unmodelled variation of system bandpass as a function of focal plane position, which can beat against the sparse dither pattern of the survey

For reasons not yet fully understood, the least squares system solved by self calibration mixes spatial modes of different scales. In particular, input errors with focalplane scale can drive output errors with much larger spatial scales. Further, modes with large spatial scales tend to be poorly damped, so small amplitude errors on focalplane scales can sometimes result in long wavelength error modes with larger amplitude.

We do not at present have the analytical tools to usefully predict these error processes. We must rely on the results of simulations, as discussed in the following section. The error budget for uniformity, based on these simulations, is summarized in Table 4.

9. Testing and Verification

The calibration process presented above is complex, and meeting the SRD requirements is dependent on understanding and controlling a large number of small perturbations. We seek to verify that our approach will produce the required results, and are doing so with different techniques that apply to the stages of LSST’s construction and operation. During the current final design phase, we are employing simulation tools, backed up when possible by measurements on the sky from existing telescopes. (Burke et al. 2013) and (Burke et al. 2010) are examples of this approach. During the construction phase, we will be able to feed measured data from actual telescope components into the simulations. During operations, our focus is on designing metrics that will let us assess the calibration quality on an ongoing basis.

9.1. Self Calibration Simulation

One of the final steps in the LSST calibration process is running self-calibration, solving for a large number of stellar magnitudes and observation zeropoints. The accuracy and precision of the self-calibration procedure has complicated dependencies on various sources of noise as well as the overall observing strategy which determines how well different regions of sky can be tied together. We have undertaken a series of simulations to test the validity of the LSST self-calibration process. A more comprehensive discussion is available in Yoachim et al. (2013).

To simulate self-calibration, we require a catalog of realistic LSST observations of bright stars. We generate this catalog by combining Galfast and Opsim. The Galfast code generates a realistic model of the Milky Way stellar populations, matching the observed distributions from SDSS. The LSST Opsim can then be used to generate observations of the stars in the

Galfast model. For each Opsim pointing, we generate a list of observed stars along with an observed magnitude that includes atmospheric and hardware effects.

An example self-calibration simulation is shown in Figure 53. This simulates the first two years of LSST observations in r -band, with 1.3 million stars distributed fairly uniformly across the sky. The observed stellar magnitudes include offsets for cloud extinction, noise based on the Opsim 5σ -limiting depth, errors due to ghosting and illumination corrections, and errors based on variations in the filter throughput and placement. The results are promising, showing we easily meet the SRD uniformity requirement, and are very close to meeting the repeatability requirement. The detailed input parameters of this simulation are listed in §C.

Self-calibration simulations will continue to be important during commissioning and regular survey operations. By running simulations that match the conditions of the actual LSST observations, we will be able to identify regions of the sky which are poorly linked to the rest of the survey. We will also be able to identify which spatial scales have the largest errors, which can have important ramifications for cosmological observations (e.g., galaxy clustering) (Huterer et al. 2013).

9.1.1. *Self-Calibration of a Large System Using HEALpixels*

The self-calibration problem for LSST results in a very large least squares system. For comparison, the uber-cal of SDSS involved 36 million observations of 12 million unique stars. For LSST in the first two years we will have around 3.2 billion observations of 100 million unique stars. The memory and computation power required to solve such a system demands that we parallelize the problem in some way.

We have developed a technique using the Hierarchical Equal Area isoLatitude Pixelization (HEALpix) tessellation of a sphere. The HEALpix tessellation was originally designed for analyzing all-sky CMB observations. HEALpixels have equal area, and are distributed to allow fast calculations of multipole moments and power spectra.

To run self-calibration in parallel, we assign each observation (consisting of a patch ID, star ID, observed magnitude, magnitude error, and possibly Illumination patch ID) to the nearest four HEALpixels on the sky. This divides the observations in such a way that we have regions on the sky that are entire HEALpixels plus an added border of approximately one-half HEALpixel. We have had good results with using 768 (53 square degrees) or 3072 (13 square degree) HEALpixels.

Once the observations have been divided, we run the self-calibration solver on each HEALpix region independently. By solving each HEALpixel in isolation, each result has a unique floating zeropoint. To tie the system back to a single floating zeropoint, we construct a matrix based on

$$P_{ij}^{model} = P_i^{best} + HP_j \quad (40)$$

where the P_{ij}^{model} are the patch zeropoints that were fitted on each HEALpixel. The equation is solved for the true patch zeropoint P_i^{best} and the HEALpixel floating zeropoints HP_j , completely analogous to Eqn 33. If an illumination correction is included, we replace the patch ID with a unique ID for each patch ID and illumination ID combination present. At full density, we expect ~ 100 stars per calibration patch and ~ 15 observations per year. Thus, by using the patches to tie large scale solutions together, we have reduced the computational requirements by three orders of magnitude. For example, the two-year r -band simulation presented shown in Figure 53 has 129 billion non-zero matrix elements in the full self-calibration formulation, but the patch solution needs only 32 million non-zero elements.

This procedure is inefficient in the sense that each patch zeropoint and stellar magnitude is solved for 4 times. However, there is substantial speedup provided by not having to run the solver to convergence over very large spatial scales. Once the final patch zeropoints are solved for, we loop back through the data and apply the zeropoints (and possibly illumination solution) to the stellar observations and calculate a weighted mean for the final best-fit stellar magnitudes. We are currently weighting the patches in Eqn 40 by the number of stars they contain. This should probably be refined, as patches taken in cloudy conditions will be poorly fit even if they contain many stars.

The solutions returned by fitting in parallel are well-matched to solutions which solve the system simultaneously. Figure 55 compares a fit with the traditional global solver with a solution made with HEALpixels.

9.2. Auxiliary Telescope Simulation

We have a simulator under development, “auxteles”, for the generation of spectra by the auxiliary telescope, and the fitting of atmospheric models to them. The spectrum generation is done by simSpectro, which propagates Kurucz spectra through atmospheres generated by Modtran4, and into a simplified spectrograph model. The atmospheric model fitting is done by simSolver, and is based on the formulation of Burke et al (Burke et al. 2010). Auxteles has been used to study the impact of spectrograph resolution on the accuracy of the atmospheric models, with results shown in Figure 56. Note that the errors shown do not include errors

due to unmodeled atmospheric variations away from locations of the probe stars (see Section 8)

9.3. Calibration Performance Metrics

9.3.1. Repeatability

Testing our repeatability is rather trivial, as it does not require any external data. We simply apply the best-fit patch zeropoints to each patch and measure how well we make repeat measurements of each star. By comparing the repeatability in data taken in photometric conditions versus non-photometric, we can empirically test the systematic limits of the photometry pipeline as well as constraining the structure function of typical clouds at Cerro Pachon.

9.3.2. Spatial Uniformity

The primary means of testing the spatial uniformity of the final calibration is to compare to previous surveys. Pan-Starrs notes that they tend to see SDSS-shaped footprints in their residuals when comparing surveys. This will probably only put an upper limit on the uniformity, as LSST will be deeper and/or have larger coverage than available comparison surveys. Simulations can also help identify regions which we would expect could be poorly linked to the rest of the survey. This is expected to be a particular problem early in the survey before all regions of the sky have many well-linked observations. We can measure very accurately our RMS as a function of patch and magnitude, and thus generate mock catalog realizations to run through the self-calibration procedure. These mock catalogs should give a good picture of the spatial uniformity, and can be used to help schedule future observations to ensure calibration residuals are minimized.

9.3.3. Flux Calibration

As mentioned in Section 6.1, there should soon be a system of white dwarf flux standards with HST observations. We can use subsets of these flux standards to make bootstrap estimates of our overall flux calibration. This is also a potential test of the spatial uniformity of the calibration, although this will be limited if the flux standards are concentrated along the celestial equator.

9.3.4. Color Calibration

There are now a number of techniques for comparing stellar colors across the sky. Ivezić et al. (2004) use a principal color analysis, High et al. (2009) use a stellar locus regression, and Schlafly et al. (2010) look at the color of main-sequence turn-off stars. For all of these techniques, the signal is usually dominated by dust extinction. However, at high galactic latitudes, the differences in stellar colors reveals errors in the calibration.

In addition to main-sequence stars, our flux standards should be useful for checking the color calibration. As with the flux calibration in a single band, we can exclude some of the flux standards from the analysis and use the excluded stars to see how well we recover their colors.

10. Software Implementation

The calibration process presented above is software intensive, as is clear from Figures 1 - 4. All software components are implemented within the LSST Data Management System, in two separate productions, described briefly here, and in much more detail in DM publications. The end products of the calibration process are Level 2 data products, also described below.

10.1. Calibration Products Production

The Calibration Products Production is responsible for the processes shown in Figures 2 and 3. These processes occur with varying frequencies:

- The monochromatic illumination correction is determined at most monthly, and likely less frequently, since it is expected to be quite stable.
- The corrected monochromatic flats are formed monthly.
- The synthetic broadband flats used in nightly reductions are computed every night.
- Atmospheric models are computed from the auxiliary telescope spectra and water vapor monitoring system every 24 hours.

Additionally, this production creates other data products used in nightly image processing, including bias frames, fringe frames, and crosstalk correction matrices. These are produced as needed.

10.2. Calibration Within the Data Release Production

The processes shown in Figure 1 are performed as part of the Data Release Production (Figure 57).

10.3. Level 2 Data Products

LSST will characterize the system throughput to a degree necessary to achieve the SRD calibration requirements. The system throughput information will be captured by the *normalized system response function*, ϕ_b :

$$\phi_b(\lambda|\mathbf{p}) = \frac{\lambda^{-1}S_b(\lambda|\mathbf{p})}{\int \lambda^{-1}S_b(\lambda|\mathbf{p})d\lambda} \quad (41)$$

which relates the object’s specific flux (spectral energy distribution; SED), $F_\nu(\lambda)$, and the calibrated, in-band, flux at the top of the atmosphere, F_b :

$$F_b = \int F_\nu(\lambda)\phi_b(\lambda|\mathbf{p})d\lambda \quad (42)$$

In the equations above, \mathbf{p} captures the dependence on time, telescope pointing (*alt*, *az*), and the position (*x*, *y*) at which the source has been imaged in the focal plane, and $S_b(\lambda|\mathbf{p})$ is the *total system throughput*. For details, see Eqs 4 and 5 in the LSST SRD.

LSST aims to deliver calibrated fluxes, F_b , in standard bandpass, for all objects and sources in its catalog. We plan to provide the calibrated fluxes for each source/object computed assuming i) flat $F_\nu(\lambda) = \text{const}$ SED (F_b^{flat}), and ii) an SEDs chosen from a library of SEDs, that is consistent with object properties (measured color being the most apparent one, but shape, Galactic longitude and latitude, and others may be considered as well). We expect most users will prefer and use the latter.

These assumed SEDs and precomputed fluxes will not be appropriate for all cases. Examples include objects exhibiting SED variability, and objects with exotic SEDs. To enable *recalibration* of the measured fluxes using user-supplied SEDs, we will retain and make available the normalized system response function, ϕ_b , for every visit. This will allow the computation of the multiplicative corrections to the provided flux:

$$c = \frac{\int f_\nu^{user}(\lambda)\phi_b(\lambda|\mathbf{p})d\lambda}{\int f_\nu^{flat}(\lambda)\phi_b(\lambda|\mathbf{p})d\lambda} \quad (43)$$

and computation of the recalibrated flux as:

$$F_b^{user} = c F_b^{flat} \quad (44)$$

Note that $f_\nu^{flat}(\lambda) \equiv 1$ and since ϕ_b is normalized to one, the denominator of Eq. 43 is identically equal to one as well. Therefore, only the numerator needs to be computed to get c .

10.3.1. Storing and Obtaining $\phi_b(\lambda|\mathbf{p})$

The total system throughput, $S_b(\lambda|\mathbf{p})$, from which $\phi_b(\lambda|\mathbf{p})$ is derived, can be factored into two components, S_b^{sys} and S_b^{atm} :

$$S_b(\lambda, t, alt, az, x, y) = S_b^{sys}(\lambda, x, y, t) \times S_b^{atm}(\lambda, alt, az, t) \quad (45)$$

, capturing its dependence on the telescope+camera system and the atmosphere, respectively. The two will be measured and/or derived as described in Document XXX.

S_b^{sys} will be stored as a series of (λ, x, y) data cubes. For each measurement, we expect on order of ~ 100 bins in both x and y , and about ~ 200 bins in λ . As discussed in Section 5, S_b^{sys} is expected to vary slowly with time, necessitating not more than \sim monthly re-characterization (and therefore, about one new data cube per month). These data cubes will be made available to the user, both in bulk form (e.g., FITS files), and as tables (or functions) in the LSST database.

S_b^{atm} will be computed from models of the atmosphere derived using the spectra obtained with the auxiliary telescope. The parameters of this model will be stored in the database and made available to the user, together with the software needed to compute S_b^{atm} . For ease of use, we will also provide database tables or functions returning $(\lambda, S_b^{atm}, \sigma_{S_b^{atm}})$ evaluated with $\Delta\lambda = 1\text{nm}$ resolution, for each visit³.

The radiometer/GPS data on precipitable water vapor will be stored in the database together with other exposure metadata. The user will be able to query this information for each exposure.

³Or potentially for each CCD in a visit, in case of strong gradients in S_b^{atm}

10.3.2. Database-level Recalibration

We will provide an easy-to-use database interface to perform recalibration given user-defined SEDs. While the exact syntax is yet to be finalized, the following example should be illustrative of how the user could obtain recalibrated time series using the highest-level of provided APIs:

```
SELECT
    midPointTai,
    filter,
    recalibPsFlux(sourceId, mySeds.sedId, "mySeds")      as flux,
    recalibPsFluxErr(sourceId, mySeds.sedId, "mySeds") as fluxErr,
FROM
    Sources, mySeds
WHERE
    Sources.objectId = mySeds.sedId
INTO
    myRecalibratedMagnitudes
```

The query above assumes that, for each object of interest, the user has uploaded their SED into a table named `mySeds` and keyed it by `objectId`. Given the name of the table and the ID of the SED entry, functions `recalibPsFlux` and `recalibPsFluxErr` will use the `sourceId` to locate the appropriate S_b^{sys} and S_b^{atm} pertaining to that specific measurement, compute ϕ_b and the correction c , and return the recalibrated point source flux and its error, respectively.

A suite of lower level functions will be provided as well, providing a more granular control of the recalibration process.

11. Risks and Mitigations

The error budget presented in Section 8, and the simulation results presented in Section 9 show that LSST will meet SRD requirements for calibration, easily for uniformity, but with small margin for repeatability. There is clearly a risk that once commissioning or survey operations begin, an unanticipated source of error will arise, or that known error sources will have been underestimated. The calibration process that we have designed is very similar to those of PS-1 and DES, as previously mentioned. It is therefore cause for some concern that the PS-1 results reported in (Tonry et al. 2012) show clear evidence for

systematic errors that are not understood. Schlafly et al. (2012) nonetheless achieved 10 mmag calibration by empirically correcting for those errors, but it's far from clear that a further improvement by a factor of two would be achievable without better understanding of the source of the systematics. Before turning to more specific risks, we first address this general concern.

It is important to recognize that LSST will incorporate some significant improvements over PS-1:

- Continuous determination of atmospheric extinction through the auxiliary telescope and water vapor monitoring system
- Determination of monochromatic illumination corrections through forward modelling, observations of star grids, and feedback from self calibration
- Careful treatment of the difference between the SED used for construction of the broadband flat and that of objects being photometered

We are confident that these improvements will go a significant way toward better control of the systematics. To address the possibility that our confidence is misplaced, we are pursuing several mitigation strategies that will further improve performance.

- The first mitigation that we will develop is a more rigorous treatment of finite PSF effects, along the lines of equation 28. We have some reason to expect that this will lower the systematics error floor on instrumental magnitudes.
- A second mitigation involves a modification of the overall calibration process. As presented in Section 3, the current design cleanly separates compensation for changing system bandpass shape (performed in SED Correction, see Figure 1), and for changing zeropoints (performed in Self Calibration). The SED Correction process is based completely on forward modeling, in which the effect of some wavelength-dependent perturbation (eg change in atmospheric aerosols) on a particular calibration star is predicted by a measurement-based model of the effect. As an alternative, one can imagine combining the SED Correction and Self Calibration processes into one large least squares problem, in which not only the zeropoints are determined, but all the wavelength-dependent effects as well. We have tested a first step in this direction by incorporating a parameterized model of the wavelength-dependent illumination into Self Calibration. Initial results have not been promising, but this is far from invalidating the overall approach.

- Third, it is clear that systematic errors that affect the uniformity of calibration tie in to the overall survey strategy, and in particular its dithering pattern. The survey strategy is not rigid, and changes to improve calibration performance may well be possible.

We are also tracking a number of more specific risks:

- Simulation tools may produce misleading results because their functionality is limited, and validation is not complete.

We are well along in the development of a second generation calibration simulator which will address these concerns. Also, we will develop the Gauss-Markov approach to error modelling, mentioned in Section 8.1.3, into a tool which can act as an independent check on many aspects of the simulations.

- Systematics error floor for photometry is higher than expected

We are working with LSST Data Management to evaluate this risk as the software and hardware evolve, and mitigate it with improved image processing algorithms.

- Forward models for illumination correction are less accurate than expected

There is considerable scope to improve the models, and add additional sources of data as required.

- Sensor complexities may affect calibration

Testing of prototype LSST sensors has uncovered complex behavior which has not generally been recognized in previous generations of CCD detectors (though it is likely to be there at lower levels). Effects include "tree rings", intensity dependent PSF, and charge dependent electron transport. These may leave an imprint on calibration which is not removed by the standard image processing approach.

We are working with LSST Data Management to develop better calibration products, particularly flat fields, that, in conjunction with improved image processing algorithms, will reduce the impact.

- The currently planned 400nm short wavelength cutoff of the auxiliary telescope may result in insufficient precision in ozone determination

The effect of the short wavelength cutoff can readily be evaluated with existing data, prior to FDR, allowing a change in the spectrograph design if needed.

REFERENCES

- Blake, C. H., & Shaw, M. M. 2011, PASP, 123, 1302
- Bohlin, R. C. 2000, AJ, 120, 437
- Bohlin, R. C. 2007, in Astronomical Society of the Pacific Conference Series, Vol. 364, The Future of Photometric, Spectrophotometric and Polarimetric Standardization, ed. C. Sterken, 315
- Bohlin, R. C., & Gilliland, R. L. 2004a, AJ, 128, 3053
- . 2004b, AJ, 127, 3508
- Bretherton, F. P., Davis, R. E., & Fandry, C. 1976, in Deep Sea Research and Oceanographic Abstracts, Vol. 23, Elsevier, 559–582
- Bretherton, F. P., & McWilliams, J. C. 1980, Reviews of Geophysics and Space Physics, 18, 789
- Burke, D., et al. 2013, AJ(submitted)
- Burke, D. L., et al. 2010, ApJ, 720, 811
- Eppeldauer, G. P., Yoon, H. W., Zong, Y., Larason, T. C., Smith, A., & Racz, M. 2009, Metrologia, 46, 139
- Gaffard, C., & Hewison, T. 2003, Observations/Development Technical Report TR26, Met Office, National Meteorological Library, Exeter, UK. Also available from <http://tim.hewison.org/TR26.pdf>
- Hansen, O. L., & Caimanque, L. 1975, PASP, 87, 935
- Hayes, D. S., Pasinetti, L. E., Philip, A. G. D., & Lynga, G. 1985, Calibration of fundamental stellar quantities. Proceedings of the 111th Symposium of the International Astronomical Union, held at Villa Olmo, Como, Italy, 24-29 May 1984.
- High, F. W., Stubbs, C. W., Rest, A., Stalder, B., & Challis, P. 2009, AJ, 138, 110
- Holberg, J. B., & Bergeron, P. 2006, AJ, 132, 1221
- Holberg, J. B., Bergeron, P., & Gianninas, A. 2008, AJ, 135, 1239
- Huterer, D., Cunha, C. E., & Fang, W. 2013, MNRAS

- Ivezić, Ž., et al. 2004, Astronomische Nachrichten, 325, 583
- . 2007, AJ, 134, 973
- Jordi, C., et al. 2010, A&A, 523, A48
- Krabbendam, V. 2012, LSST Docushare LTS-66
- Kurucz, R. L. 1993, VizieR Online Data Catalog, 6039, 0
- MacDonald, E. C., et al. 2004, MNRAS, 352, 1255
- Marshall, J. L., et al. 2013, ArXiv e-prints
- McIntosh, P. C. 1990, J. Geophys. Res., 95, 13529
- Nordsby, M. 2013, LSST Docushare LCA-18
- Nugent, P., Kim, A., & Perlmutter, S. 2002, PASP, 114, 803
- Padmanabhan, N., et al. 2008, ApJ, 674, 1217
- Radomski, J., Tranco, G., Fuhrman, L., Falvey, M., Gigoux, P., Montes, V., Daruich, F., & Lazo, M. 2010, in Society of Photo-Optical Instrumentation Engineers (SPIE) Conference Series, Vol. 7737, Society of Photo-Optical Instrumentation Engineers (SPIE) Conference Series
- Regnault, N., et al. 2009, A&A, 506, 999
- Schlafly, E. F., Finkbeiner, D. P., Schlegel, D. J., Jurić, M., Ivezić, Ž., Gibson, R. R., Knapp, G. R., & Weaver, B. A. 2010, ApJ, 725, 1175
- Schlafly, E. F., et al. 2012, ApJ, 756, 158
- Sebag, J., & Krabbendam, V. 2013, LSST Docushare LSE-60
- Stubbs, C. W., Doherty, P., Cramer, C., Narayan, G., Brown, Y. J., Lykke, K. R., Woodward, J. T., & Tonry, J. L. 2010, ApJS, 191, 376
- Stubbs, C. W., & Tonry, J. L. 2006, ApJ, 646, 1436
- . 2012, ArXiv e-prints
- Stubbs, C. W., et al. 2007a, in Astronomical Society of the Pacific Conference Series, Vol. 364, The Future of Photometric, Spectrophotometric and Polarimetric Standardization, ed. C. Sterken, 373

- Stubbs, C. W., et al. 2007b, PASP, 119, 1163
- Tonry, J. L., et al. 2012, ApJ, 750, 99
- Vanden Berk, D. E., et al. 2001, AJ, 122, 549
- Veselovskii, I., Whiteman, D. N., Korenskiy, M., Kolgotin, A., Dubovik, O., & Perez-Ramirez, D. 2013, Atmospheric Measurement Techniques Discussions, 6, 3059
- Wittman, D., Ryan, R., & Thorman, P. 2012, MNRAS, 421, 2251
- Yoachim, P., Jones, L., Ivezić, Z., & Axelrod, T. 2013, LSST Docushare TBD

A. Filter Set

Figure 47 illustrates the baseline LSST filter bandpasses, including a ‘standard’ atmosphere, and baseline estimates for the mirrors, lenses, filter and detector transmission and sensitivity functions.

B. Photometric measurements for non-main sequence stars

LSST will record a series of m_b^{nat} measurements for each astronomical object in each visit. These m_b^{nat} measurements are generated directly from the counts recorded in each image, corrected with the photometrically uniform, synthetic broad-band flat field and for gray (cloud) atmospheric extinction effects. However, unless the object SED is flat, m_b^{nat} measurements will vary as the shape of the bandpass changes, whether as a function of position in the focal plane or as a function of changes in atmospheric absorption components. Correcting for these effects requires assuming a particular SED for each source, and produces m_b^{std} values after applying Δm_b^{meas} offsets (see the overview of calibration in section 5 for a review).

To generate precision photometry for objects with arbitrary SEDs, LSST will provide a record of $\phi_b^{meas}(\lambda, alt, az, x, y, t)$ as well as the zeropoint offsets, Z_b^{obs} , for each observation, as discussed in Section 10. With these data products, users can generate the appropriate Δm_b^{meas} corrections and m_b^{std} for their chosen object SED. Section 4.8 outlines the typical magnitudes of these corrections for main sequence stars; Δm_b^{meas} can easily be on the order of 20 mmag for *gri*, or even 100 mmag in *u* band. For more extreme SEDs, these corrections may be even larger.

Figure 49 illustrates the likely magnitude of these Δm_b^{meas} corrections for a wide variety of SEDs. In each plot, the main sequence stars are shown as in the figures in the main paper (small dots, color-coded by metallicity), although given the increased scale here they only appear as a purple series of circles. M dwarfs are now included, generally mimicking the behavior of the main sequence stars but extending further into the red. More unusual SEDs are also included; a quasar SED, based on a composite of many empirical quasars from SDSS from Vanden Berk et al. (2001) that has been extended to the full LSST wavelength range through the addition of power law flux above and below the original range ($f_\nu \propto 1/\lambda^{0.5}$ for $\lambda < 89\text{nm}$ & $f_\nu \propto 1/\lambda^{1.5}$ for $\lambda > 800\text{nm}$), and redshifted from $z = 0$ to $z = 3$; also a sample of SN Ia from templates generated by Peter Nugent (Nugent et al. 2002), redshifted from $z = 0$ to $z = 1$.

The figure shows the Δm_b^{meas} values that would be expected under a maximum change

of atmospheric parameters and under a likely bandpass shift. This demonstrates how much the reported m_b^{nat} values could vary for each object. If LSST was to just calculate an offset between m_b^{nat} and m_b^{std} based on an object’s color (and assuming that the object had an SED similar to a main sequence star), the resulting m_b^{std} values would be incorrect by the value of the offset between the true Δm_b^{meas} for the SED and the main sequence Δm_b^{meas} values at each color; this could easily be more than 20mmag.

C. Fiducial Self-Calibration Input

The input file used with simSelfCalib.py to generate the simulated LSST catalog presented in §9.1.

```
# the number of total stars in the sim
nStarTot = 2000000
# the magnitude range
magmin = 17
magmax = 21
# the color (g-i) range of the sim stars
colmax = 3.5
colmin = -0.8
# A value for the random seed, if desired.
random_seed = 42
# Distribution to use for mag_rand_err. Options: Gaussian, Cauchy
errorDist = Gaussian
# Parameters for using flux standard stars.
# Flux standards are all placed on patchid 0.
# number of stars per block to use.
# values < 1 make a fraction of the stars standards,
# values > 1 are the number of stars per block.
fluxFrac = 0
# Gaussian noise to add to the flux standard mags.
fluxNoise = 0.0001
# the next few values are about the zeropoint and color terms
# the random error added to the stars, distribution set by errorDist.
# This is an error floor.
mag_rand_err = 0.003
# calculate what LSST will think the error is based on observed mag (True) or output a
```

```
# more realistic error (False)
calcerror = False
# Use Opsim xparency for the gray zeropoints
zp_opsim = True
# the maximum zeropoint change added to the patches
zp_var_max = 1.0
# the maximum zeropoint gradient added to the patches
zp_grad_max = 0.0
# the maximum color term change in mag added to stars in a patch
colterm_max = 0.005
# the range between -1 < (g-i) < 1 in the color term due to filter bandpass shift.
colterm_rad_max = -0.040
# the error in the observed color -- 0 or negative values will result
# in no color gradient correction
color_obs_noise = 0.05
# the fractional error in the color correction term ()
color_correction_error = 0.10
# fraction of the FoV that the filter can jitter:
filter_jitter = 0.0055
# fractional variation in the gain (Gaussian RMS)
gainvar = 0.00
# fractional error in the exposure time (e.g., from shutter errors)
exptvar = 0.001
# number of HEALpixel sides to use. Must be power of 2.
nside = 16
# Use cloud images. Each visit has a cloud image generated on a sparse
# grid then interpolated to the star positions.
use_cloudsimage = True
# the magnitude of the sinusoidal variation
# in the zero point in the X and Y-directions. Note, these
# interfere with eachother so the total error
# will be \pm (sinvarx_mag+sinvary_mag)
sinvarx_mag = 0.00
sinvary_mag = 0.00
# the spatial scale for the sinusoidal variation
# value of 1 will make the FOV run from -pi to pi, 2--> -2pi to 2pi
sinvarx_scale = 1.
sinvary_scale = 1.
```

```
sinx_phase = 0.0
siny_phase = 0.0
# angle between the x and y variation axes. This is held constant.
sinx_angle = 20.0
# a second set of spatially varying sinusoidal errors.
# Here, the phase is randomly set for each night to simulate flat fielding errors
flat_sinvarx_mag = 0.00
flat_sinvary_mag = 0.00
flat_sinvarx_scale = 1.
flat_sinvary_scale = 1.
# angle between x and y axes. Held constant, but the phase is
# varied from night-to-night
flat_sinx_angle = 0.0
# how many nights to keep the phase constant
phase_persist = 1
# illumination correction file jdsu_utest.dat
# illumcorr_filename = None
#
# illumination correction file jdsu_r.dat ricbb.dat
#
sed_illumcorr_filename = jdsu_r.dat
bb_illumcorr_filename = ricbb.dat
# what fraction of the illumination error to use
illum_err_factor = 0.1
# focal plane temperature model file
# fpModel1_filename = fpTemp1.dat
# fpModel2_filename = fpTemp2.dat
# spatial variation from cloud removal
# fraction of the total zeropoint shift to put in as the cloud magnitude
cloud_mag = 0.00
cloud_sinvar_scale = 5.
# Variable star contamination
rr_fraction = 0
rr_amplitude = 1.
# Use Kepler stellar variability statistics?
kepler_variablity = False
# limits for sim footprint
# the ra/dec limits, in degrees
```

```
raMin = 0
raMax = 360.
decMin = -90.
decMax = 0.

# you can use opsim (True or False) to generate fields
# use opsim database (opsim3.61)
    use_opsim = True
# flag to use the opsim dither scheme, instead of random dither.
# note that opsim dither scheme covers the entire
# radius_fov (i.e. dith_Offset_frac = 1)
    use_opsimdither = True
# opsim filter, if using this
    opsimfilter = r
# then specify time to start/stop, in nights from start of opsim
    tstart = 0
    tstop = 730
# or don't use opsim and specify nEpoch instead
# nepoch = number of visits to each field
    nEpoch = 10
# you can use calsim database to generate the stars.
# Available calsimtables include: "msrgb", "msrgb_1e6", and "msrgb_1e7"
    use_calsim = True
    calsimtable = msrgb_1e6
# you can also change the radius of the field of view
    radius_fov = 1.8
# and the number of patches to split this radius into. should be 'square' (nPatch=N^2)
    nPatch = 25
# raOff and decOff control dithering
    dith_raOff_frac = 0.5
    dith_decOff_frac = 0.5
# Limits of camera rotation, in degrees (has a dithering effect)
# (LSST standard = -90 to 90)
    dith_skyRot_min = -90
    dith_skyRot_max = 90
# filenames for outputs
# starobs is the file input to the solver
    starobs_filename = star_obs.dat
# should starobs contain the subpatch information?
```

```
# These can then be solved for illumination corrections.  
print_subpatch = True  
# number of radius bins to use for the illumination correction  
nRadiusBins = 5  
# number of g-i color bins to use for the illumination correction  
nColorBins = 1  
# output each ra/dec block to it's own file (only use for very large sims)  
multifile = False  
# master file contains everything relevant to every measurement of every star  
master_filename = /dev/null  
# stardata is the basic star magnitudes, positions and colors  
stardata_filename = stardata.dat  
# star data for re-assigning patches  
ras_filename = /dev/null  
# visitdata gives the information on the visits used in the simulation  
visit_filename = visit.dat  
# patchdata gives the information on the patches in the simulation  
patch_filename = patchdata.dat
```

D. Glossary

- **Level 1 Data Product.** A data product, such as a measurement of an astronomical object’s position or flux in a single image, that is computed on a nightly basis. Level 1 data products primarily consist of alerts on transient, variable and moving objects. The photometric calibration process outlined in this paper does not apply to Level 1 data products. Level 1 data products will be calibrated using all applicable prior knowledge (including secondary standard catalogs generated from previous Data Release calibration of all LSST-observed stars in the field).
- **Level 2 Data Product.** A data product, such a measurement of an astronomical object’s position or flux in either a single image or a series of images, that is computed on the Data Release schedule, on a six-month or yearly schedule. Level 2 data products leverage all previous observations of the same object, as well as all knowledge of the LSST system accumulated to that point. The photometric calibration process outlined in this paper is used to generate Level 2 data products.
- **Normalized system response,** $\phi_b(\lambda)$. The normalized system response describes the shape of the bandpass transmission curve, separating this from the normalization

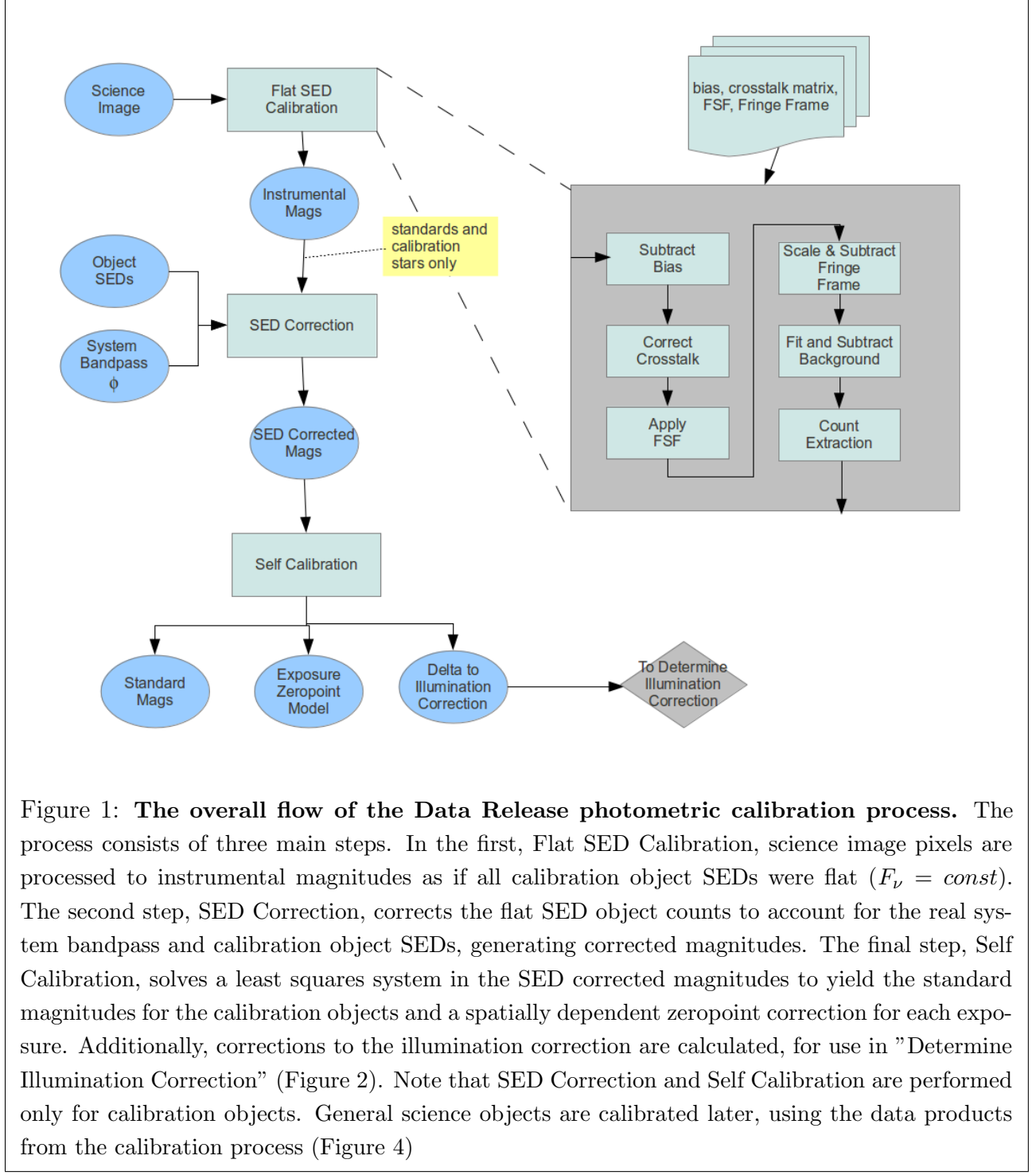
of the throughput curve which can be determined separately. $\phi_b(\lambda)$ is described by Equation 5. The integral of $\phi_b(\lambda)$ is always 1.

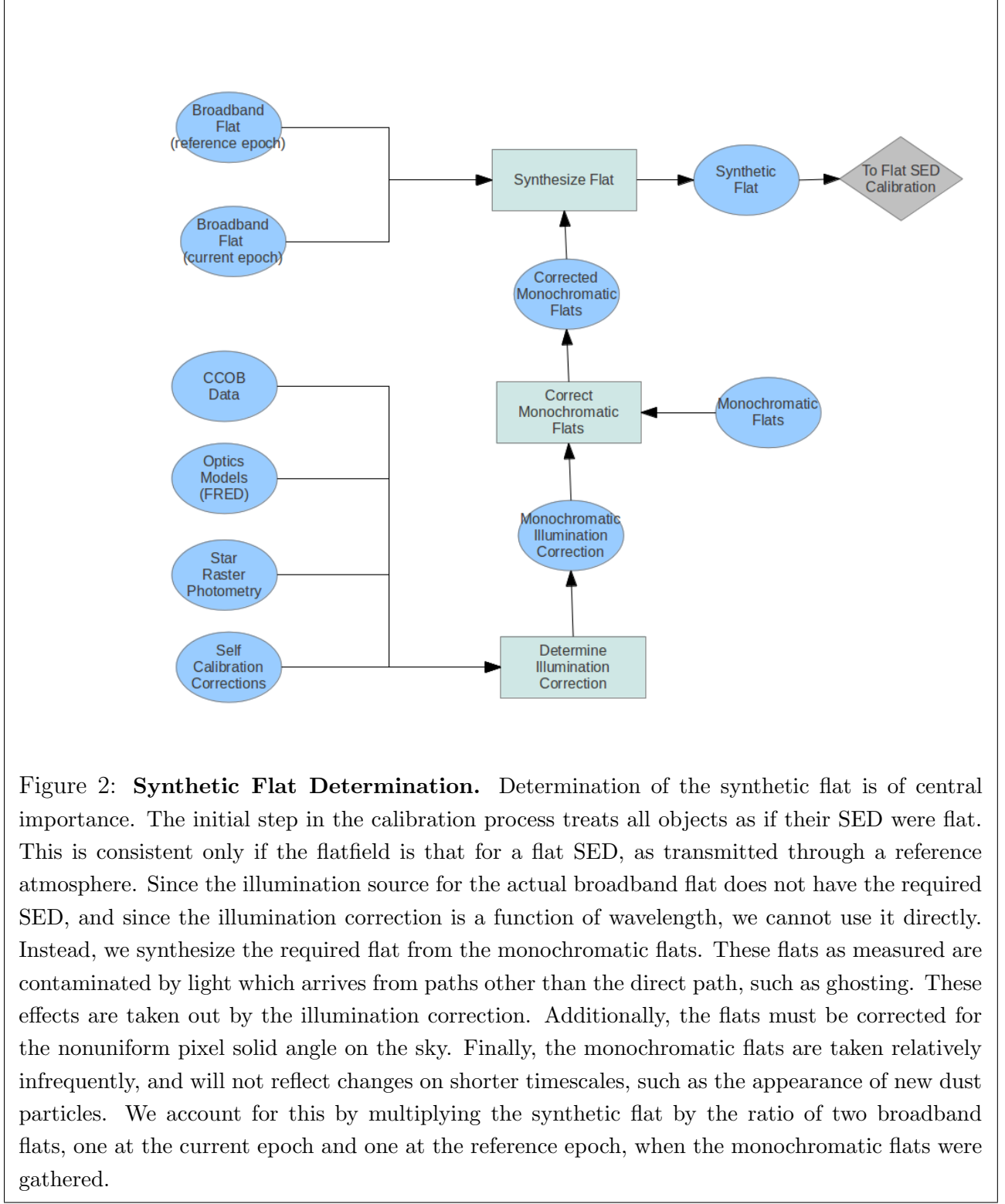
- **Camera Calibration Optical Bench (CCOB).** The CCOB is an apparatus to calibrate the spatial and wavelength-dependent response of the focal plane (detector + camera). The CCOB uses a well controlled, wavelength-variable, light source (such as a tuneable laser) calibrated using a NIST photodiode to illuminate the focal plane when the camera is unmounted from the telescope. This light source, which produces a spot in the focal plane approximately the size of or smaller than the PSF, will be scanned across the detector (x, y) at a variety of beam incident angles, (θ, ϕ) and at a variety of wavelengths (λ). This allows the response of the detector to be measured in the presence of a well-understood light source. The response of the detector can be measured in two different configurations: one with only the detector and the dewar window - which doubles as lens 3 (L3) - and one with the detector, L3, L2, L1, a small test-section of filter and the camera shutter. The filter test section used is not the full LSST filter, and thus will not capture spatial non-uniformities in the filter bandpass. The CCOB provides test data about the camera assembly for camera acceptance and will help constrain the optical ZEMAX model, although without a full filter it cannot capture the full set of parameter required for the ZEMAX model. More details about the requirements and physical apparatus of the CCOB are available in LSST-10015 and LSST-8217.
- **Broadband flat field.** An image obtained by observing a light source which generates photons with a wide range of wavelengths with relatively uniform illumination across the field of view. Night sky flats, twilight flats, and white-light or broadband dome screen flats would all generate broadband flat fields.
- **Narrowband flat field.** An image obtained by observing a light source which generates photons with a very narrow range of wavelengths with relatively uniform illumination across the field of view. A dome screen illuminated with a narrow-band laser light source will generate a narrow-band flat field.
- **‘Synthetic’ flat field.** A flat field constructed from a datacube of narrowband flats. This flat is used in image reduction, and has had a number of corrections applied to ensure that the resulting photometry is uniform as long as the objects possess the same SED as used in constructing the synthetic flat.
- **Illumination Correction.** The ratio between an ideal photometric flat obtained by a raster scan across the field of a collimated light source at infinity, and the observed

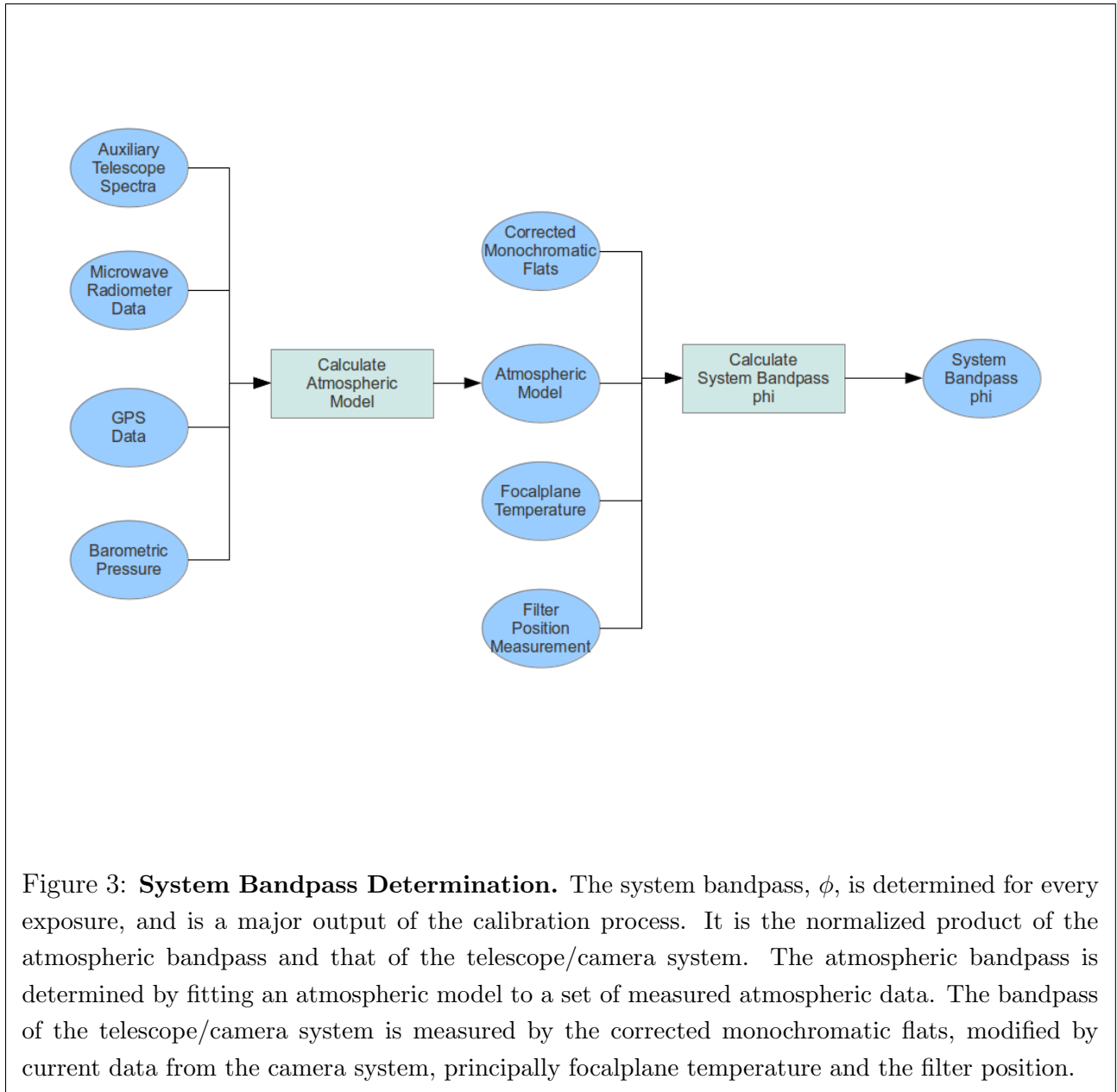
flat field.

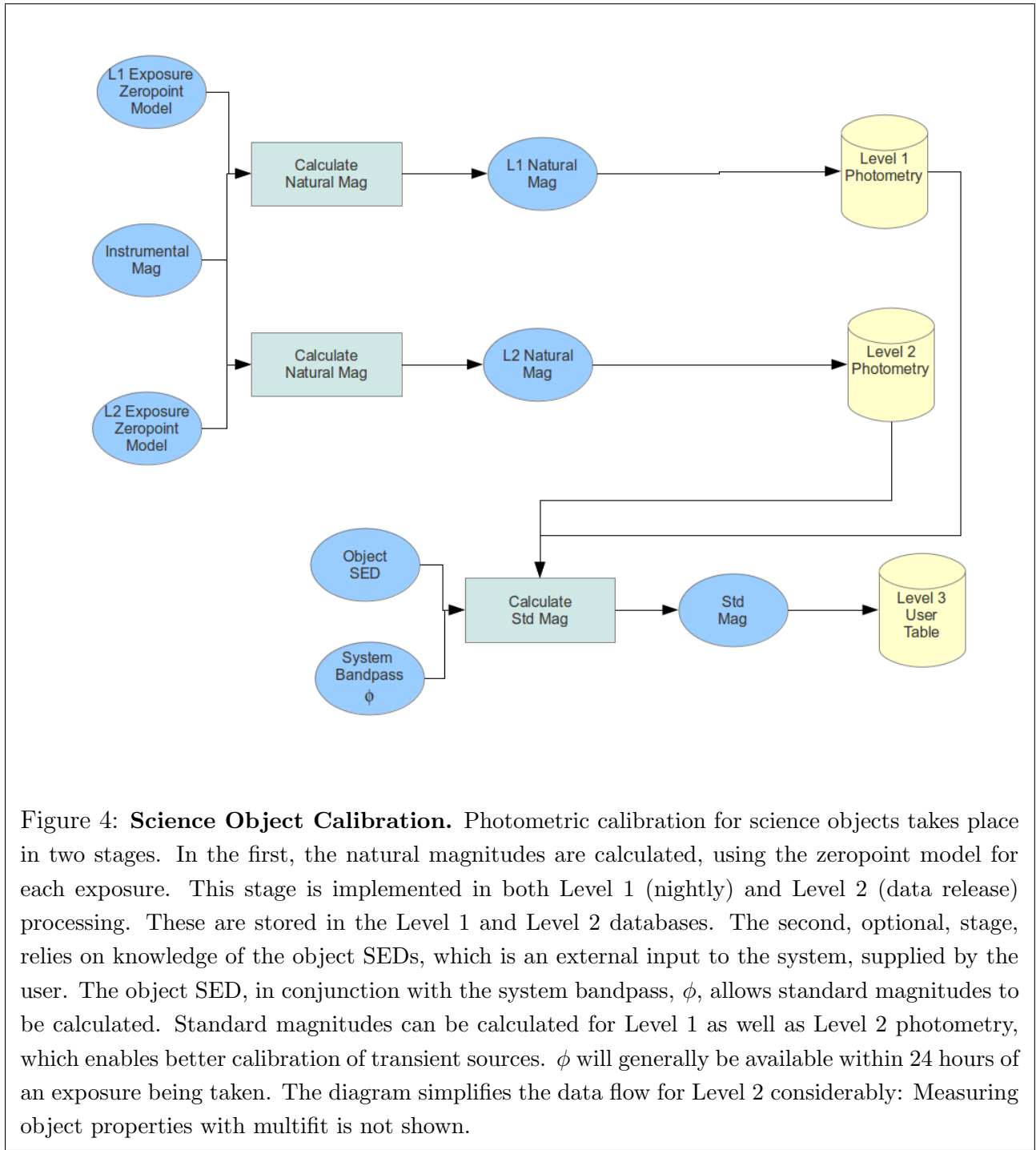
$$\text{Flat}_{\text{photometric}} = \text{Flat}_{\text{observed}} * \text{IlluminationCorrection} \quad (\text{D1})$$

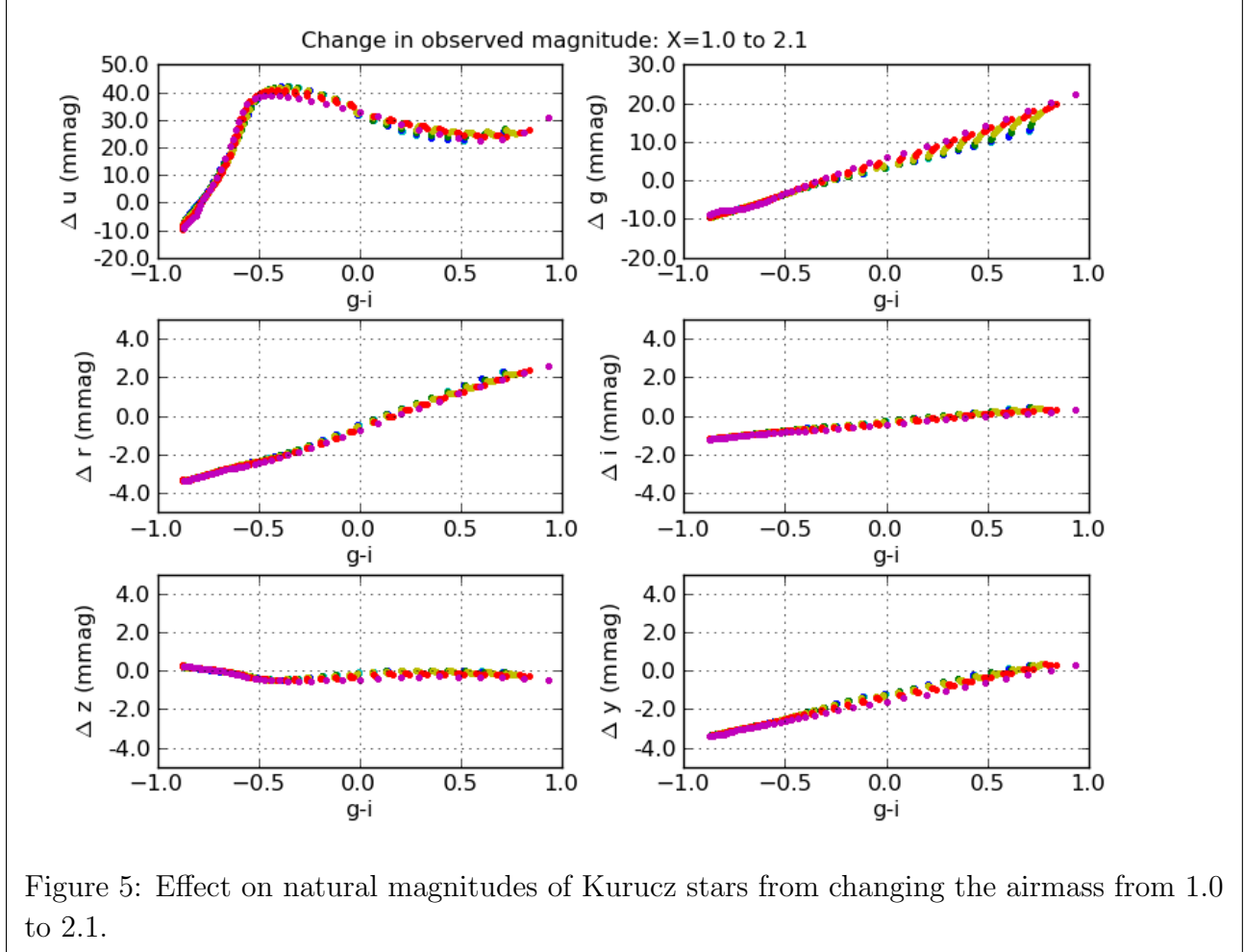
- **Natural magnitude.** A magnitude measurement which relates directly to the number of counts measurement in an image (after including a photometric flat field correction and a rough zeropoint for an entire image). The natural magnitude relate to an ADU count that does *not* account for the color or SED of the source being observed, thus does not include any wavelength-dependent corrections. For a non-variable source observed under variable atmospheric transmission conditions and/or at varying locations in the field of view, the natural magnitude reported will change due to changes in the bandpass shape. The natural magnitude is equivalent to an observed magnitude, after the appropriate zeropoints have been applied.
- **Standard magnitude.** A magnitude measurement which includes not only corrections for the photometric flat field and a rough zeropoint for the image, but also includes a correction for wavelength-dependent effects. This means the Δm_b^{meas} appropriate to correct the natural magnitude of the object from the observed bandpass shape, $\phi_b^{\text{meas}}(\lambda, t)$, to the standard bandpass shape, $\phi_b^{\text{std}}(\lambda)$, has been calculated for the SED of the object and applied. For a non-variable source, m_b^{std} will be constant over time even if the atmospheric absorption curve or the location in the field of view changes.
- **Operations Simulation.** The Operations Simulation is a simulated pointing history of LSST, covering the sky in the same manner as the telescope could, in practice. It uses weather conditions based on historical records from Cerro Tololo, including appropriate seeing and sky brightness variations. The motion of the telescope is simulated in high fidelity, including acceleration from field to field and cable wrap. A variety of proposals are used to determine which fields to observe at each time; these proposal include the ‘universal cadence’ (satisfying most of LSST’s science requirements) and ‘deep drilling’ (a limited set of fields, observed frequently and deeply over the lifetime of the survey).
- **PWV.** Precipitable Water Vapor. The total column depth of water vapor in the atmosphere, measured at zenith. The units are mm of liquid water equivalent.

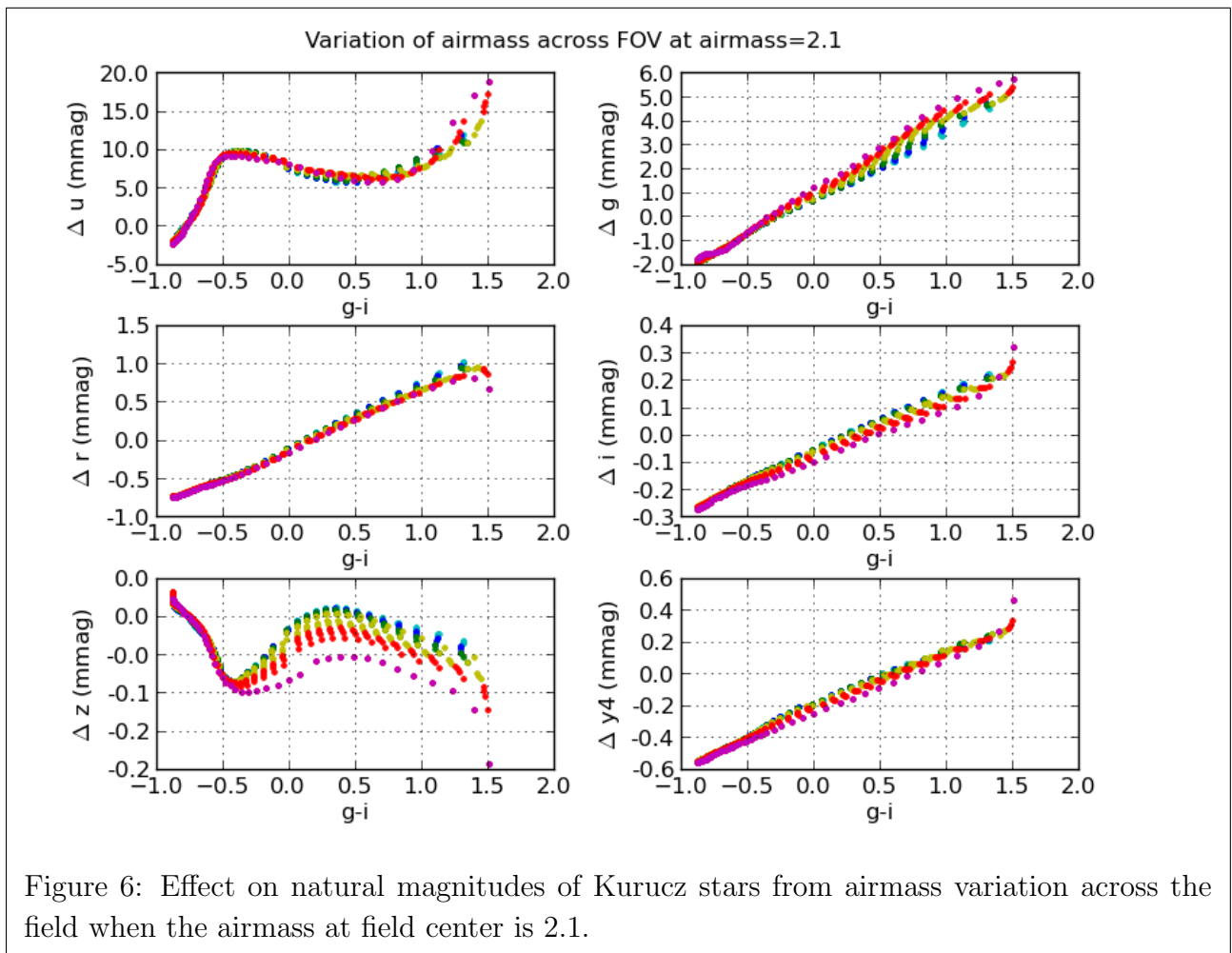


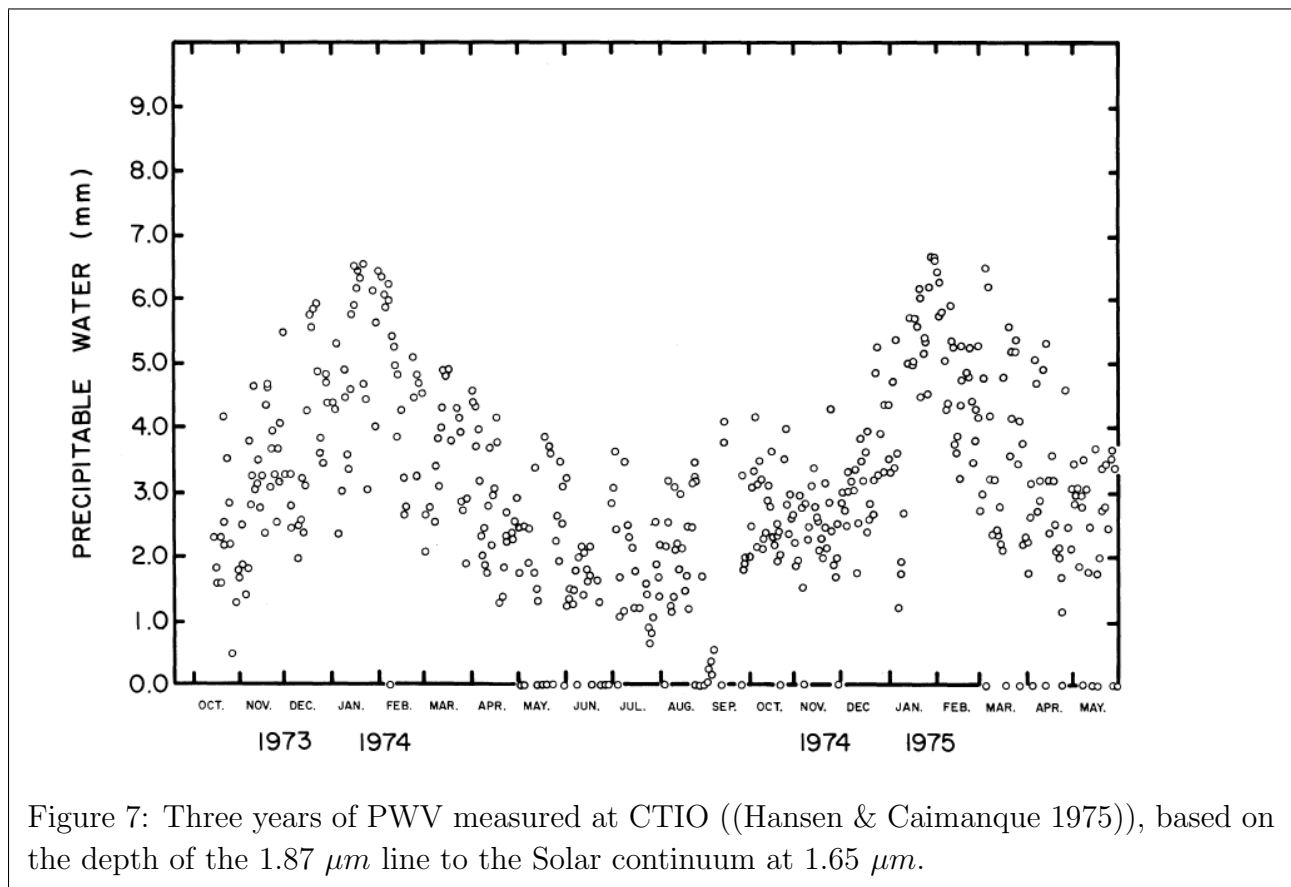


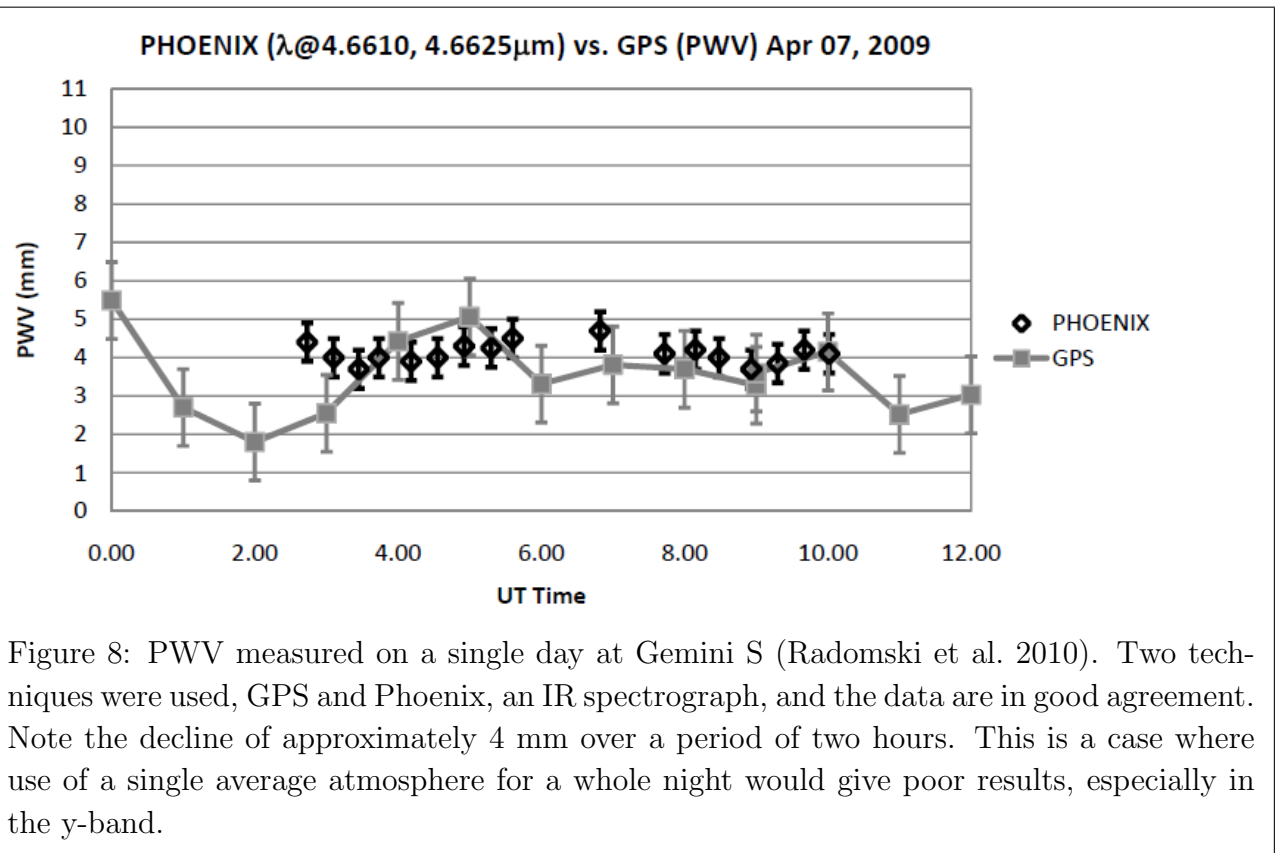


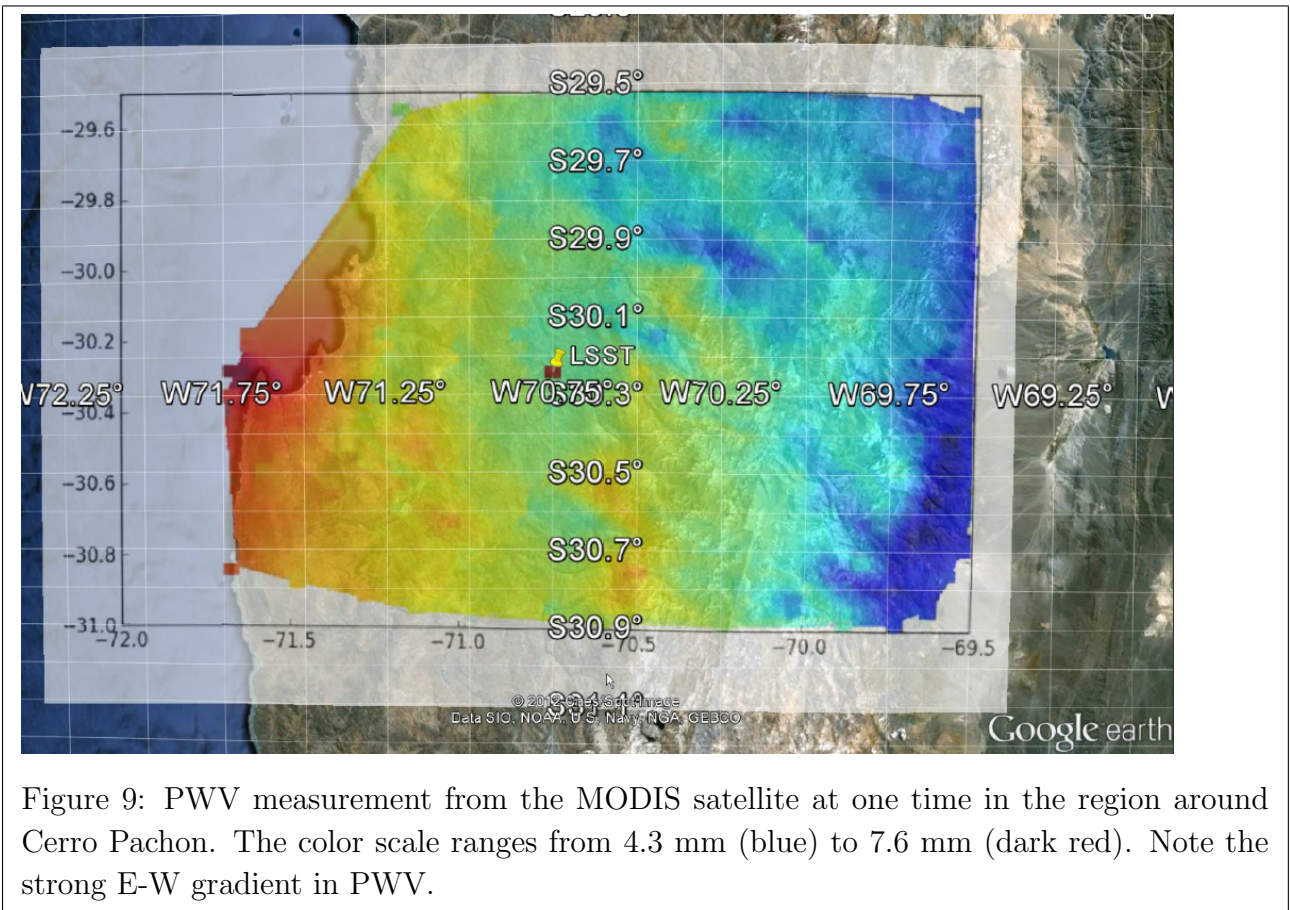


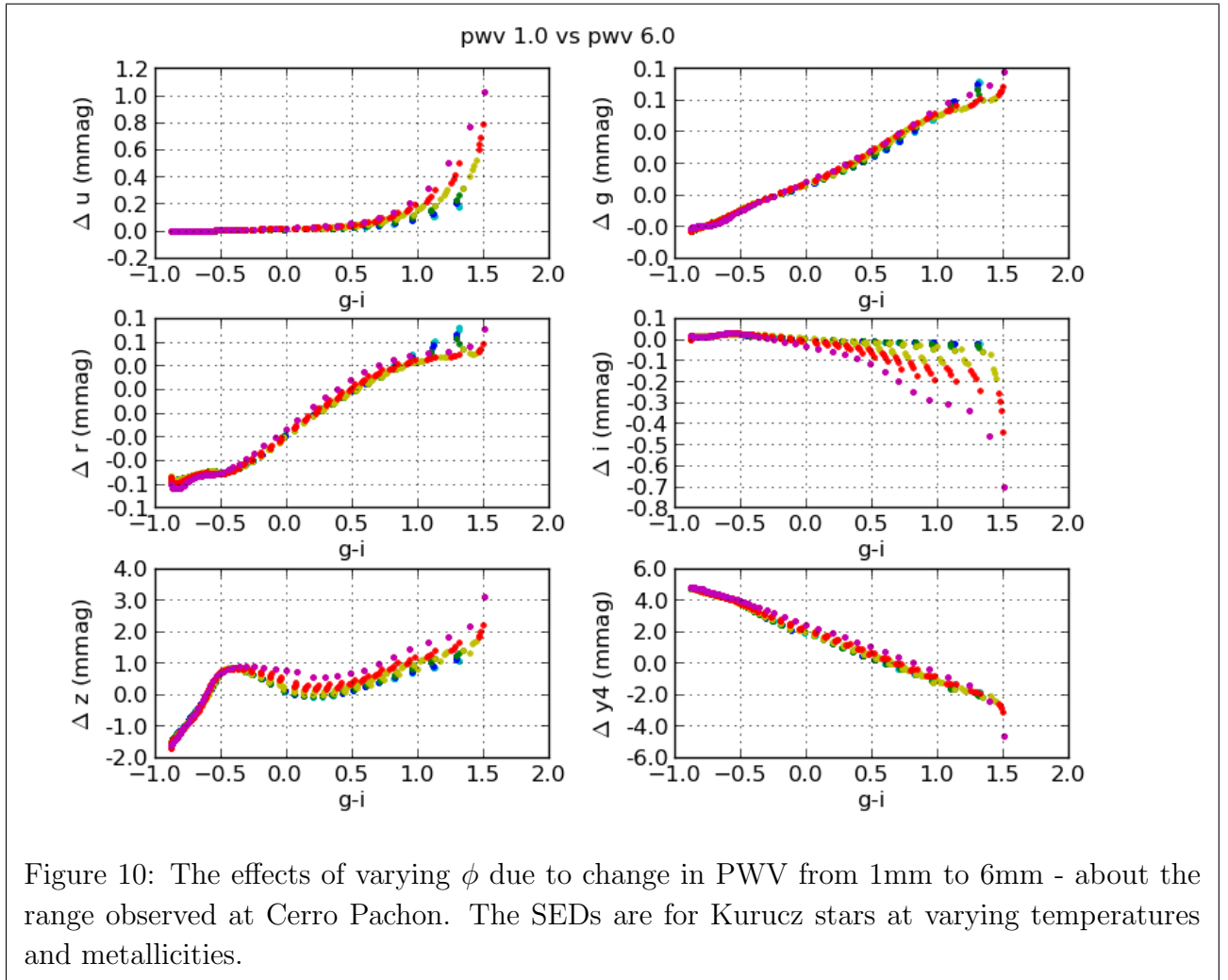












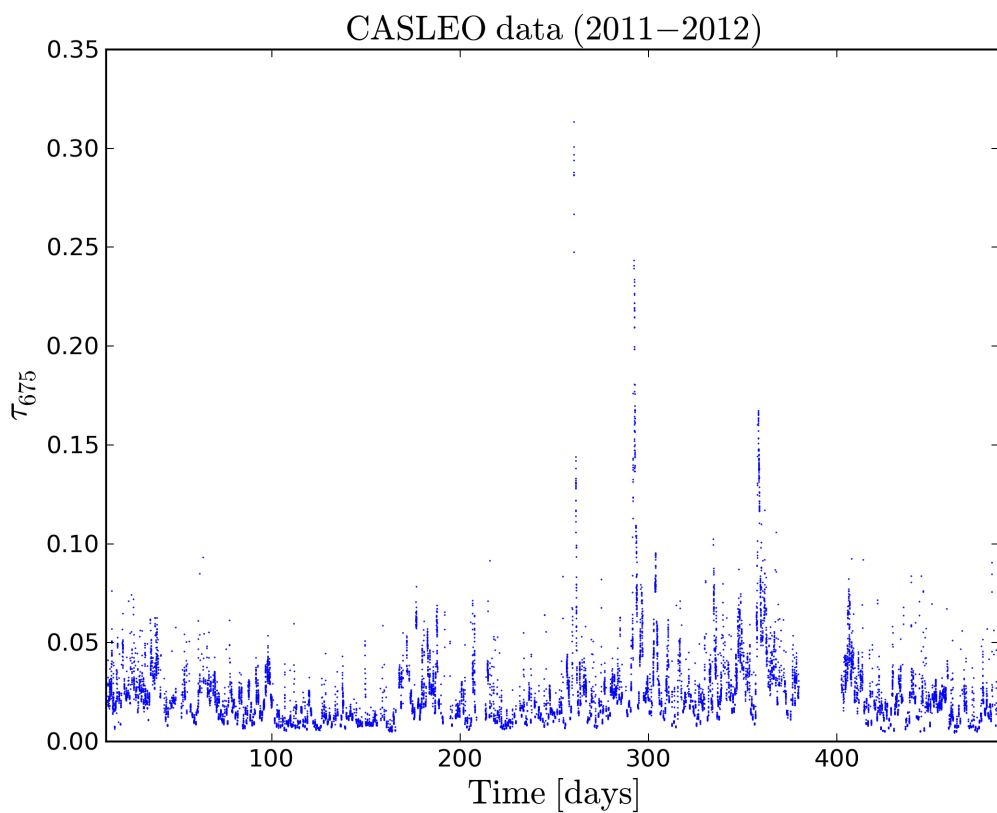
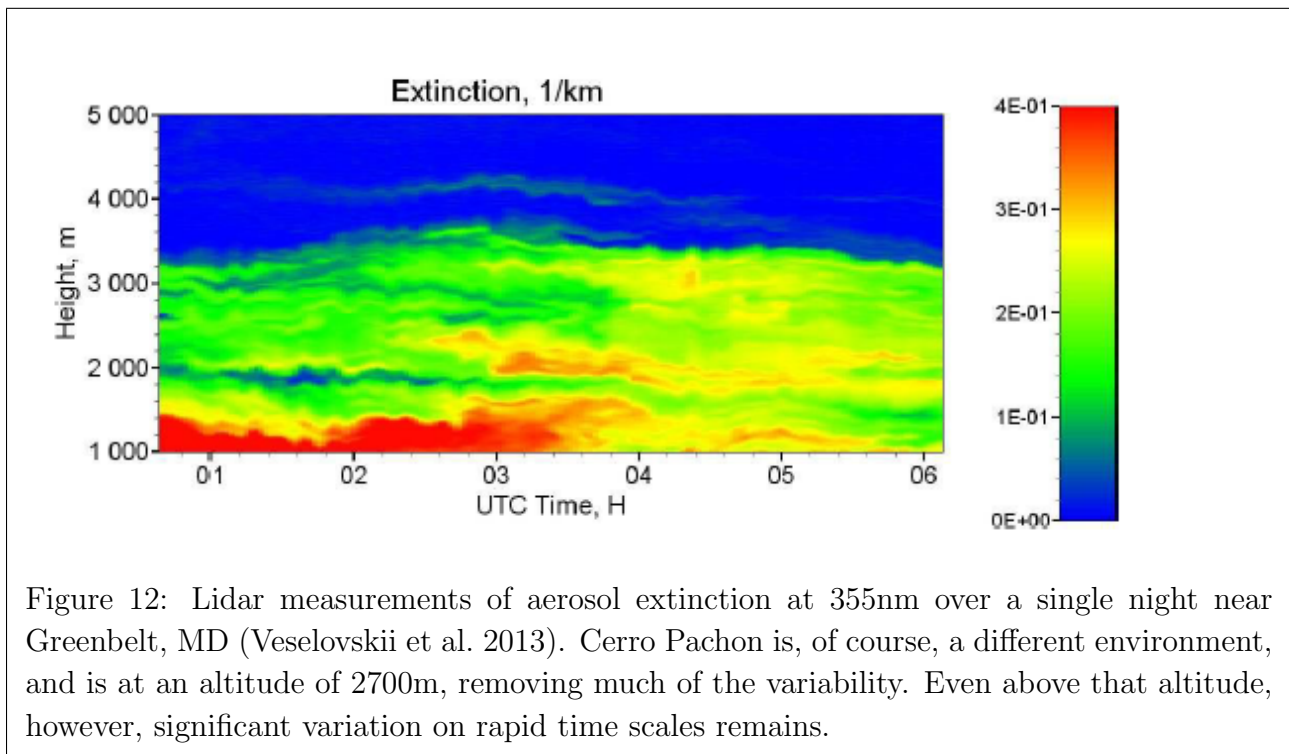
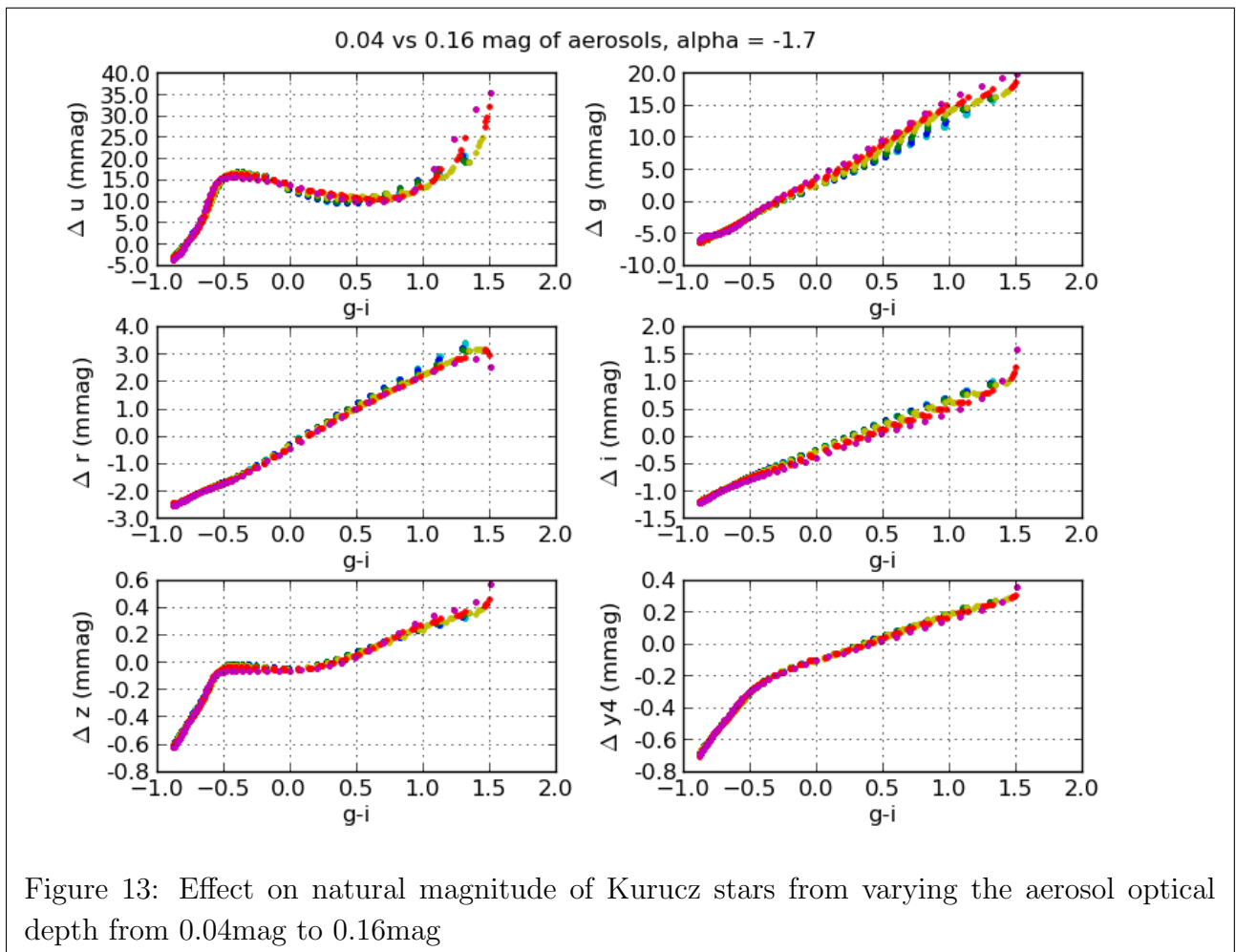
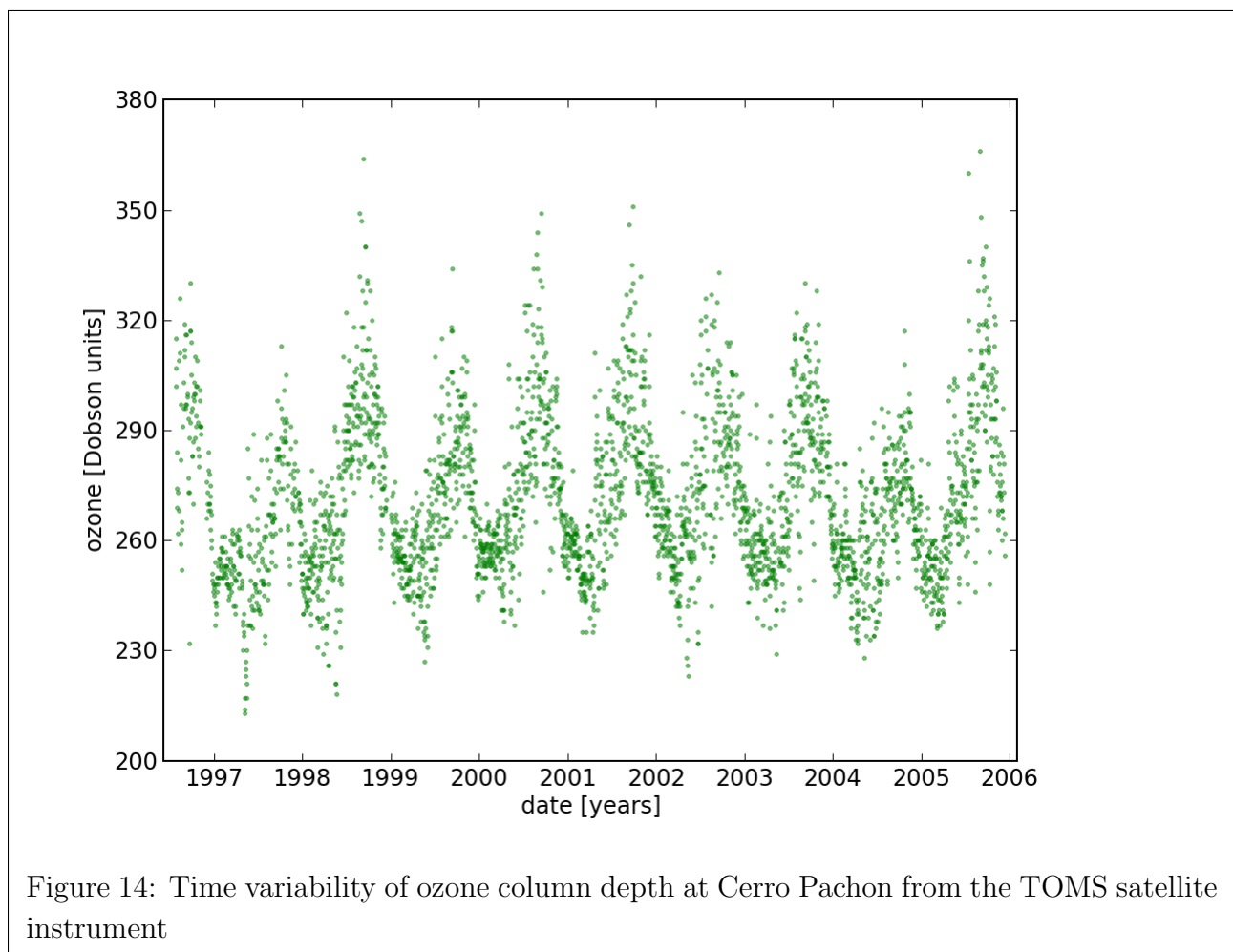
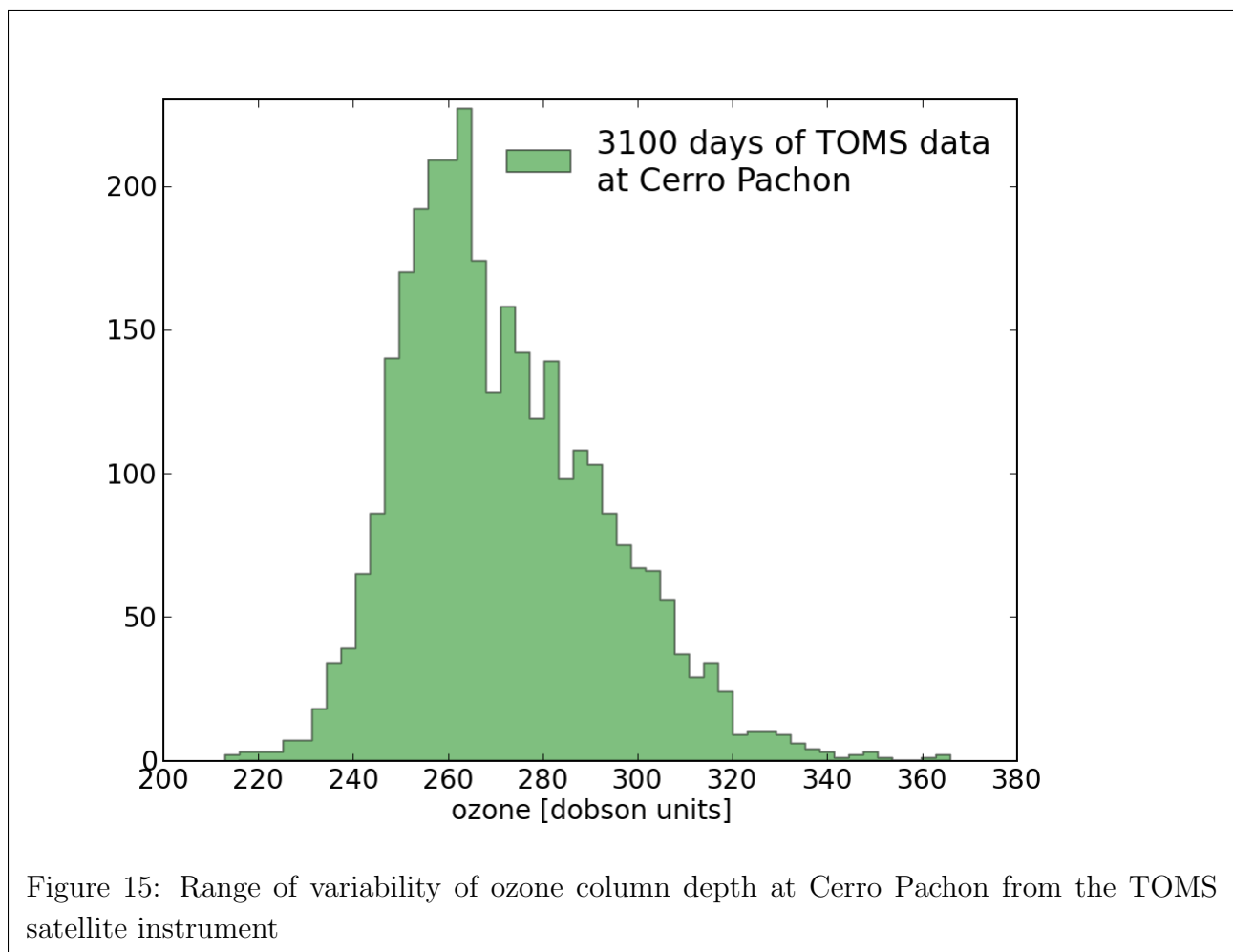


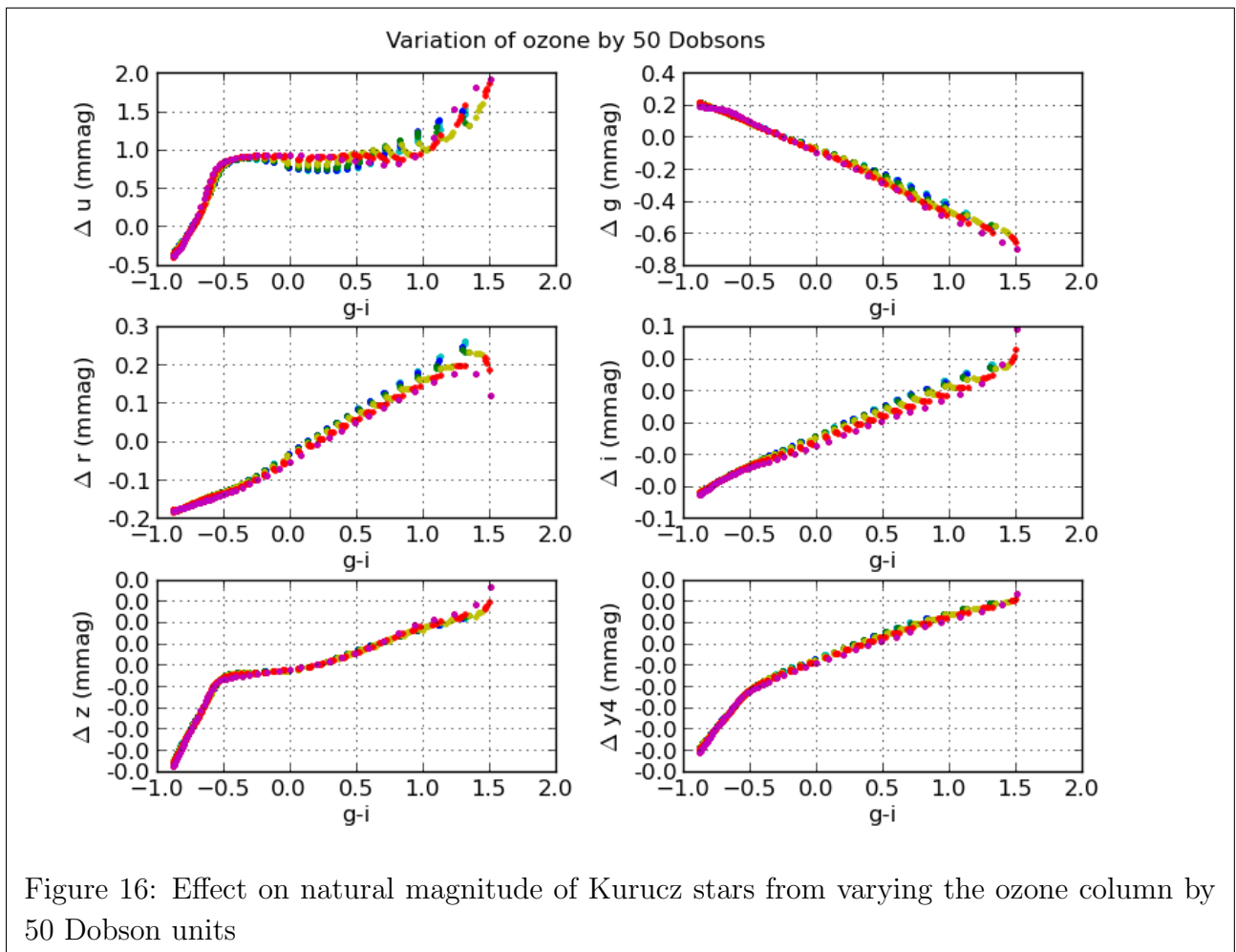
Figure 11: Varying aerosol optical depth at CASLEO, El Leoncito, Argentina. The site elevation at 2550m is similar to CP.











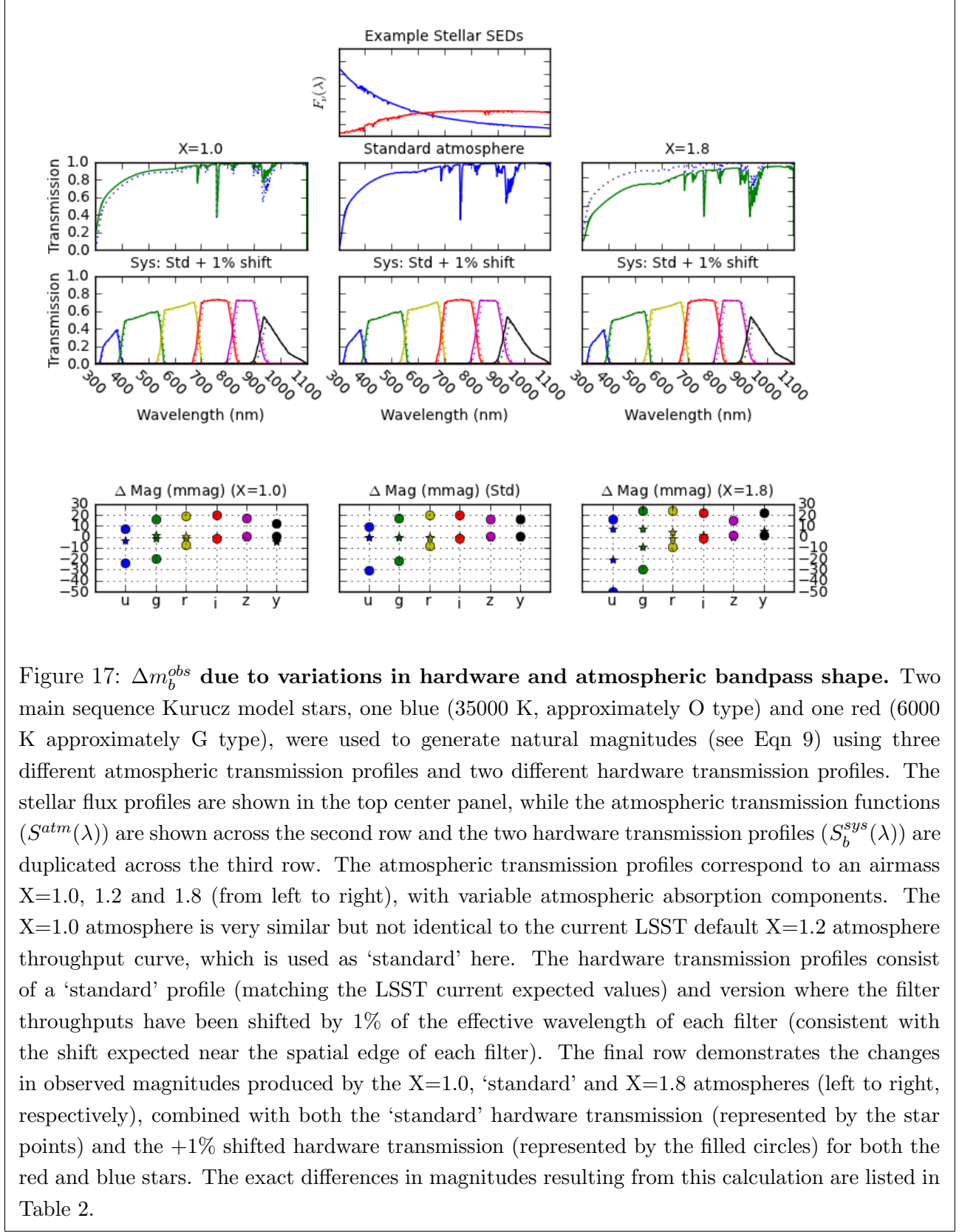
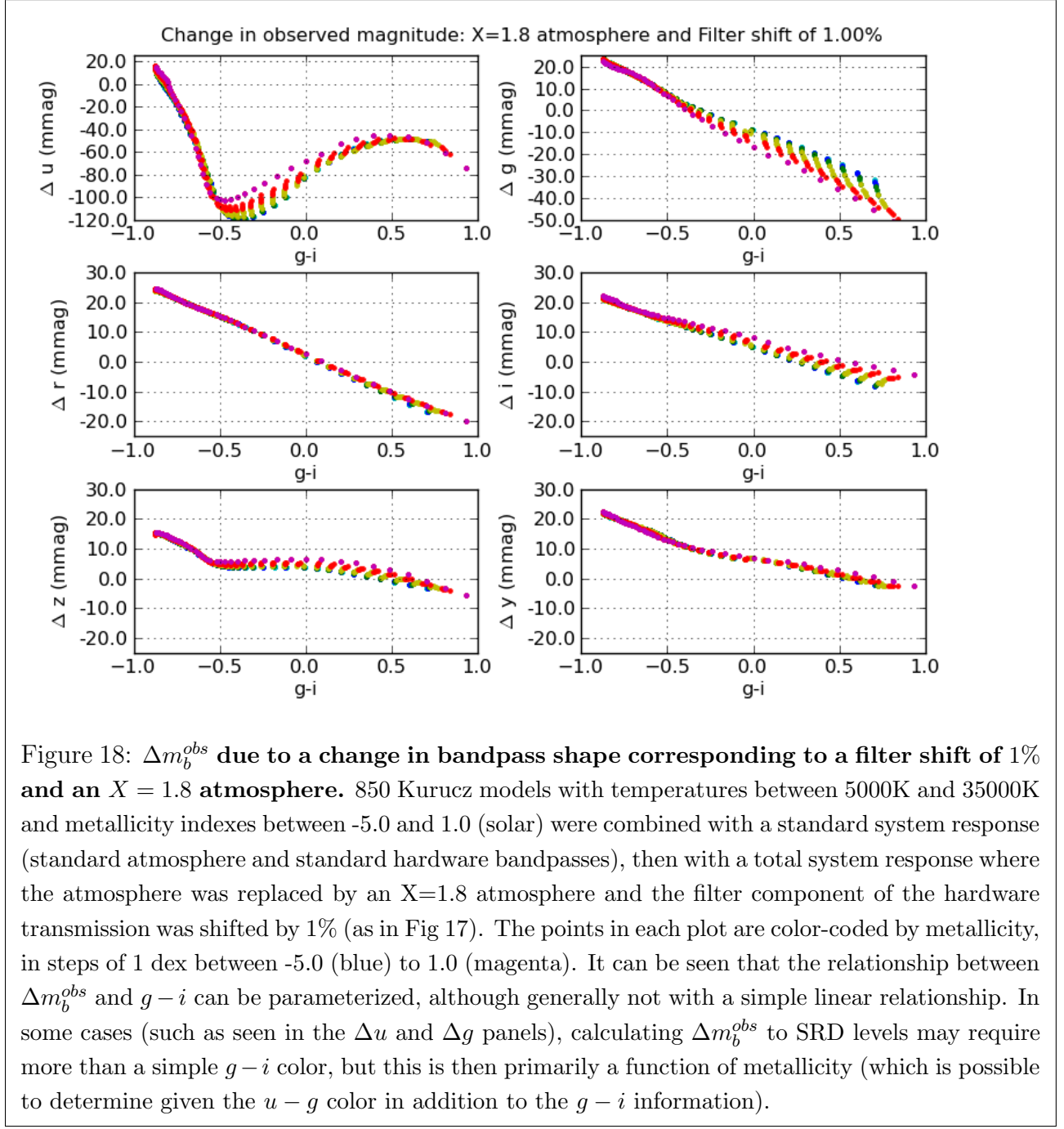
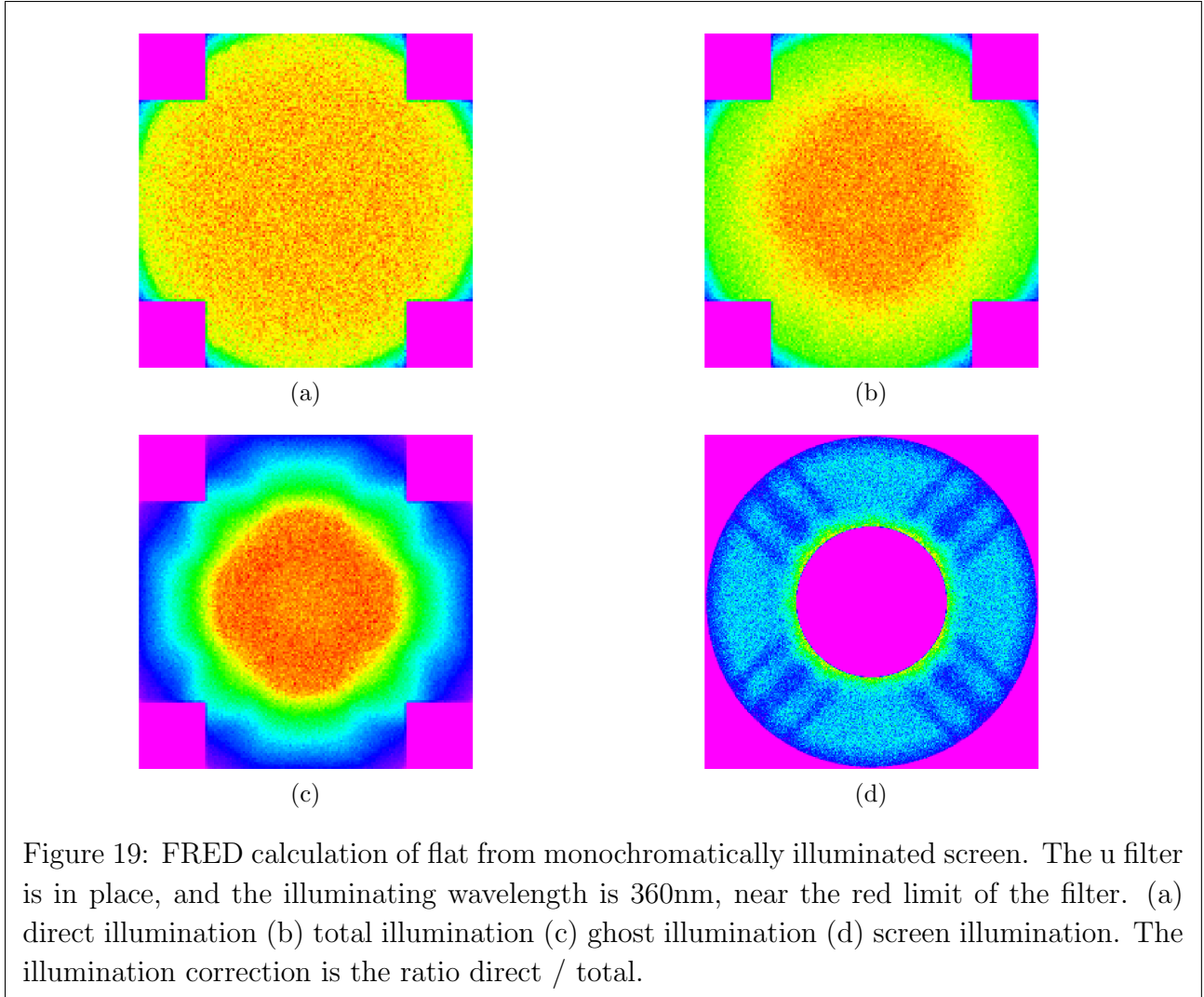


Table 2:: Δm_b^{obs} due to variations in system and atmospheric bandpass shape (see also Fig 17). The first two rows show the baseline ('standard') magnitude of the star. All other rows show the *change* in magnitude (in mmag) due to the variations listed at left. Any value larger than 5 mmag would be larger than the RMS scatter allowed by the SRD. *TODO color-code values larger than 5 mmag*

Bandpass	star	<i>u</i> (mag)	<i>g</i>	<i>r</i>	<i>i</i>	<i>z</i>	<i>y</i>
Std (X=1.2) atm, std sys	red	21.472	20.378	20.000	19.911	19.913	19.913
Std (X=1.2) atm, std sys	blue	19.102	19.503	20.000	20.378	20.672	20.886
		Δu (mmag)	Δg	Δr	Δi	Δz	Δy
Std (X=1.2), +1% sys shift	red	-31	-22	-8	-2	1	1
Std (X=1.2), +1% sys shift	blue	9	17	20	20	16	16
X=1.0, std sys	red	7	2	0	0	-0	-1
X=1.0, std sys	blue	-3	-1	-1	-0	1	-4
X=1.0, +1% sys shift	red	-24	-20	-8	-1	1	0
X=1.0, +1% sys shift	blue	7	16	19	20	18	12
X=1.8, std sys	red	-21	-10	-2	-0	0	1
X=1.8, std sys	blue	8	8	4	2	-1	6
X=1.8, +1% sys shift	red	-50	-30	-10	-2	1	2
X=1.8, +1% sys shift	blue	16	24	24	22	15	22





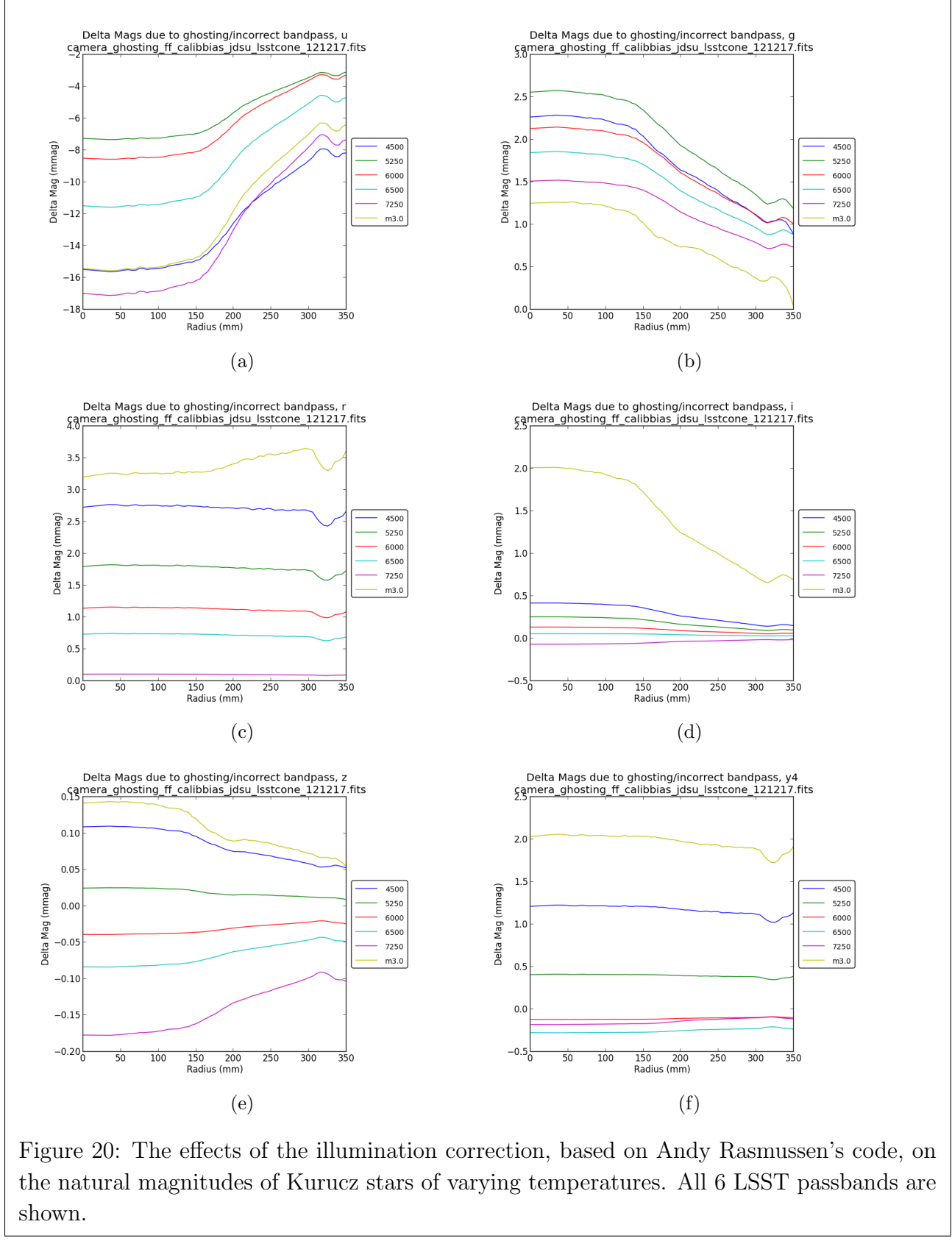


Figure 20: The effects of the illumination correction, based on Andy Rasmussen's code, on the natural magnitudes of Kurucz stars of varying temperatures. All 6 LSST passbands are shown.

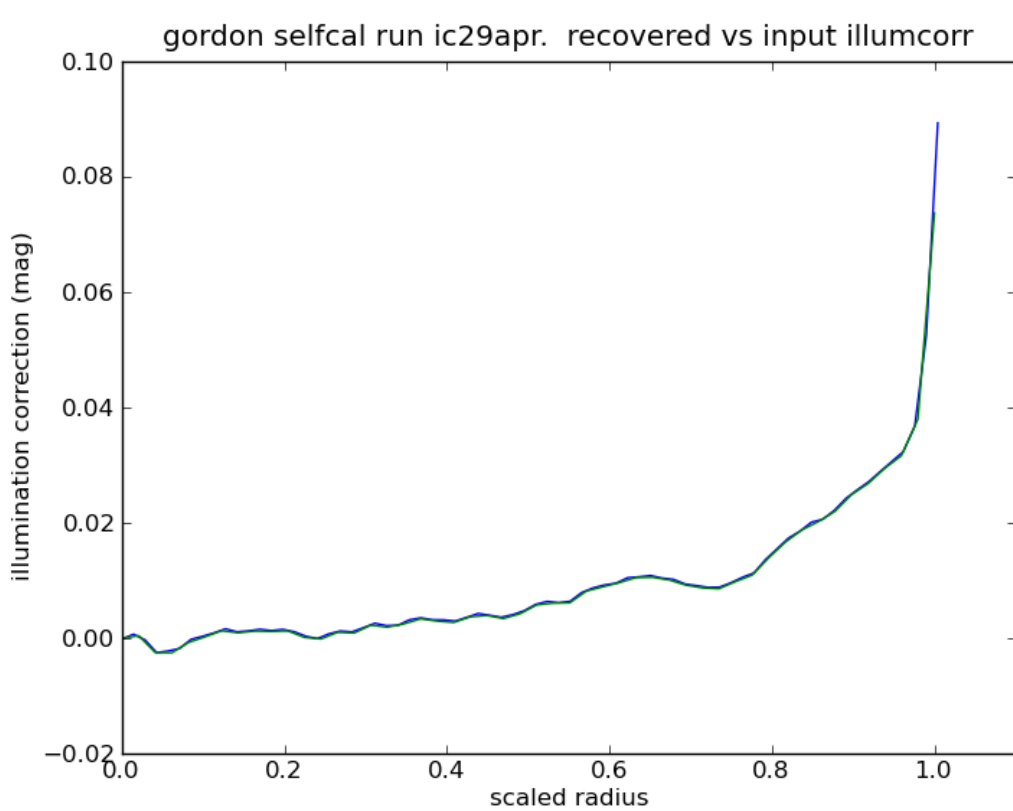


Figure 21: Recovery of input broadband illumination correction by self calibration. The input illumination correction was wavelength independent, but strongly dependent on radial position, as shown. The recovered illumination correction is essentially identical to that input.

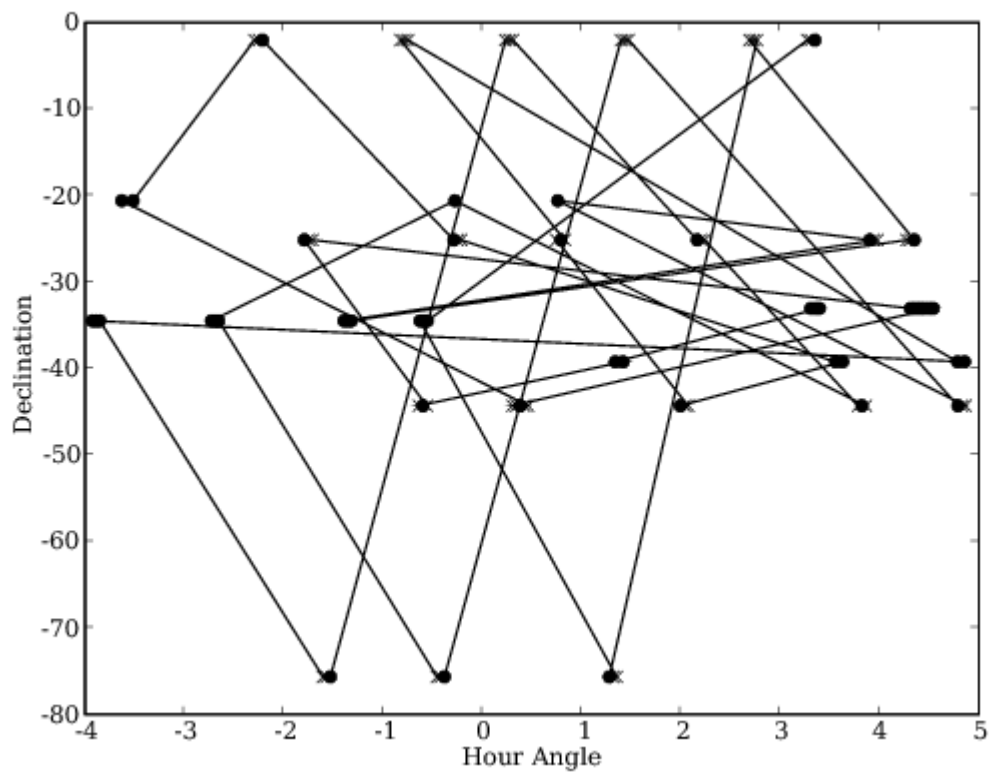
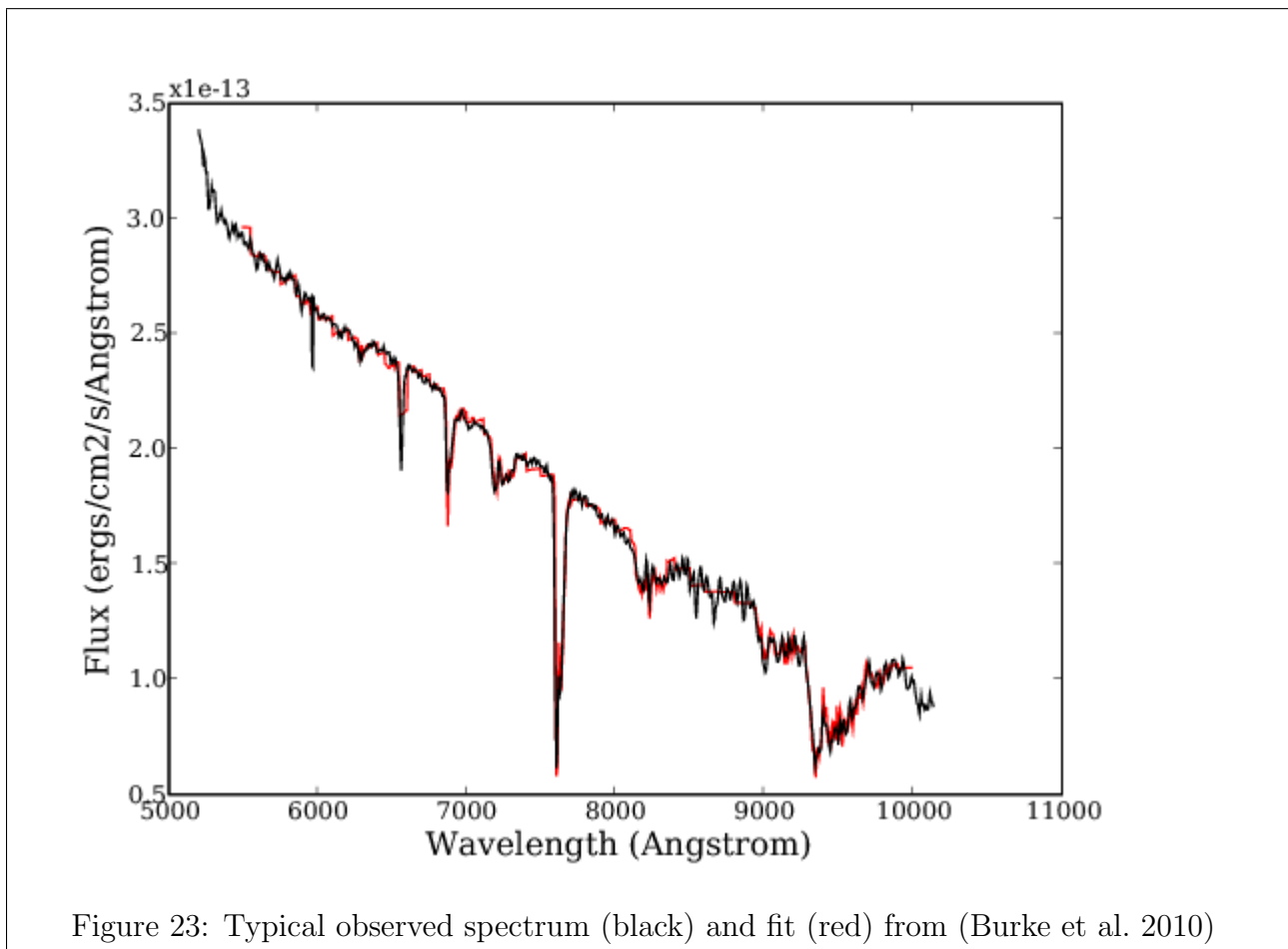


Figure 22: Pattern of observing atmospheric probe stars from (Burke et al. 2010). The Solid lines trace the temporal order of the observations



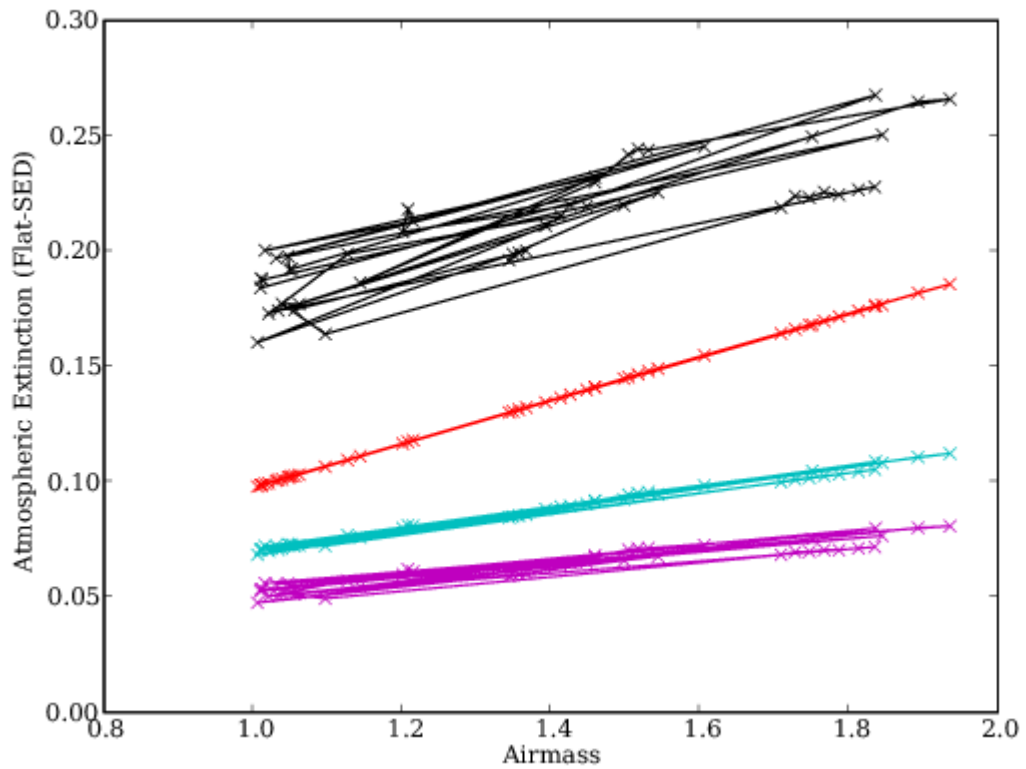


Figure 24: Non-gray atmospheric extinction from (Burke et al. 2010). Red is r-band, cyan is i-band, magenta is z-band, black is y-band. The excess scatter in the z- and y-bands is due to variability of PWV

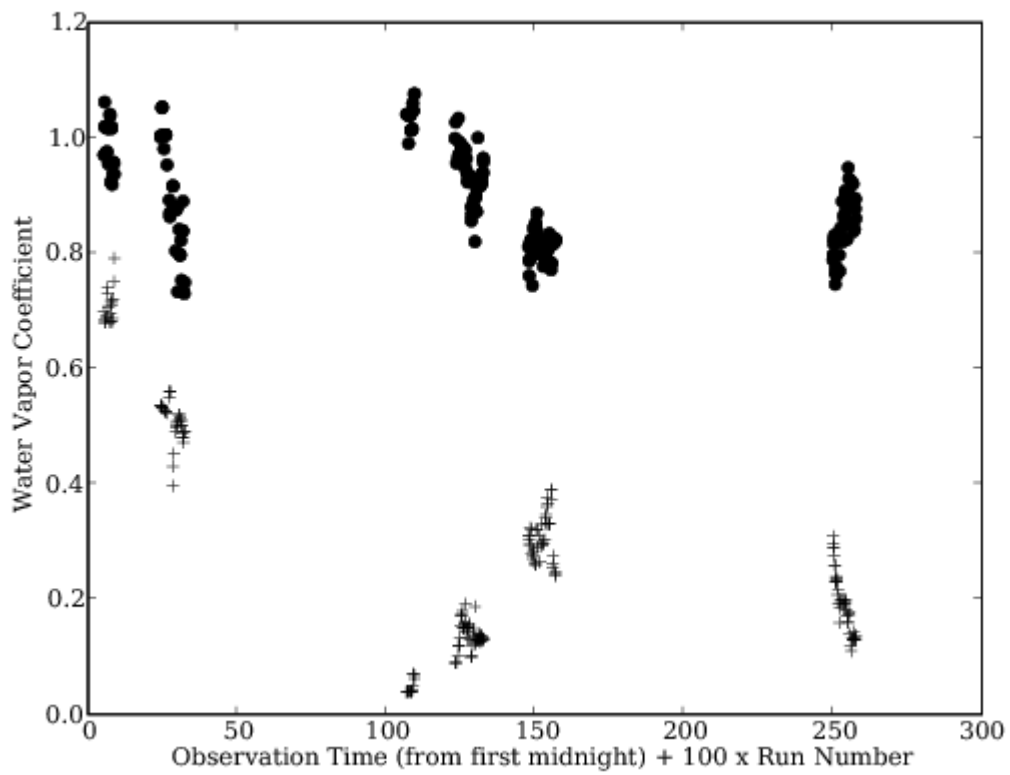


Figure 25: Fitted water vapor coefficient from (Burke et al. 2010), expressed as a ratio to the standard value (filled circles). Crosses are relative humidity from CTIO (changed scale).

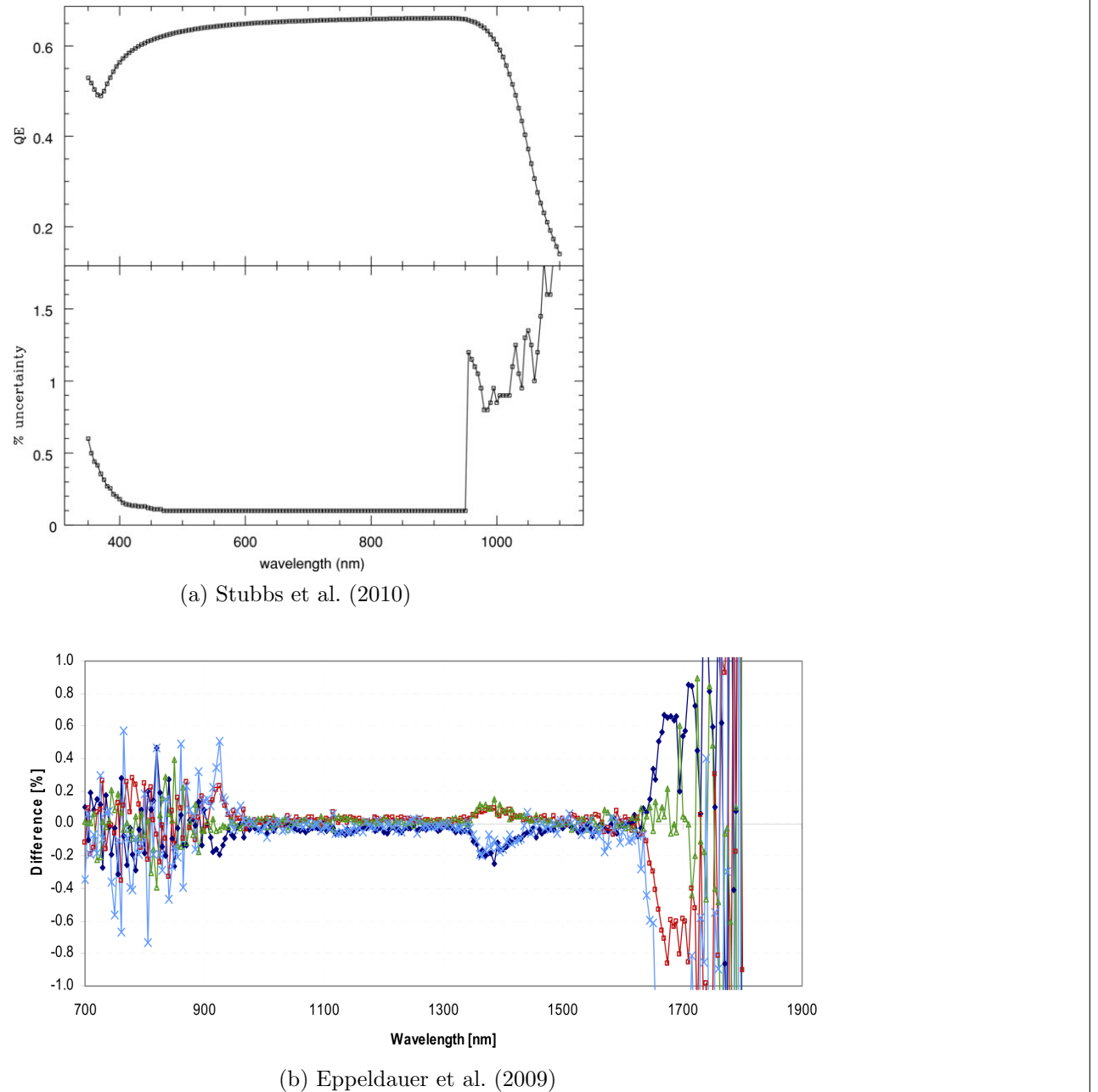


Figure 26: Quantum efficiency curve and fractional error for NIST-calibrated photodiode, from Stubbs et al. (2010) and Eppeldauer et al. (2009). Panel 26a: Between 400 and 900 nm, calibration methods already in use in test systems indicate photodiode accuracy is better than 0.1%, as in the bottom part of this panel. The sudden decrease in calibration accuracy below 900 nm is due to calibration methods used by NIST in 2005. Panel 26b: More recent photodiode calibration efforts by Eppeldauer et al. (2009) show better than 0.1% accuracy can be achieved to beyond 1200 nm, the limit of detector response for LSST, as shown here in the response curves resulting from multiple scans of a single source using the same photodiode.

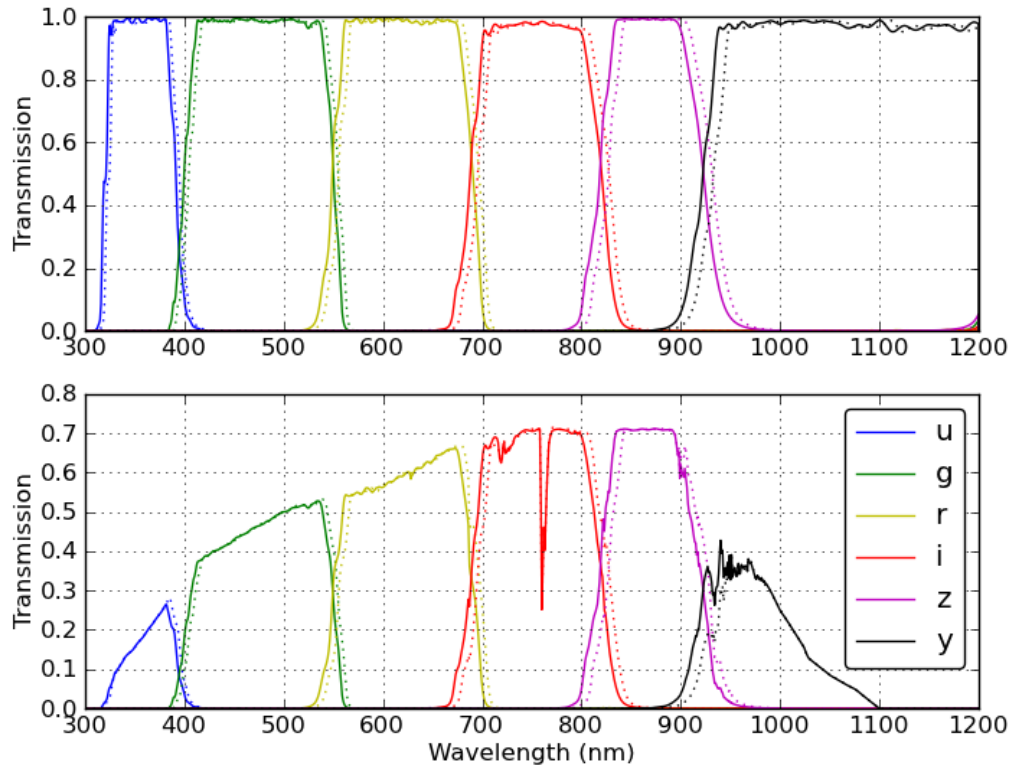
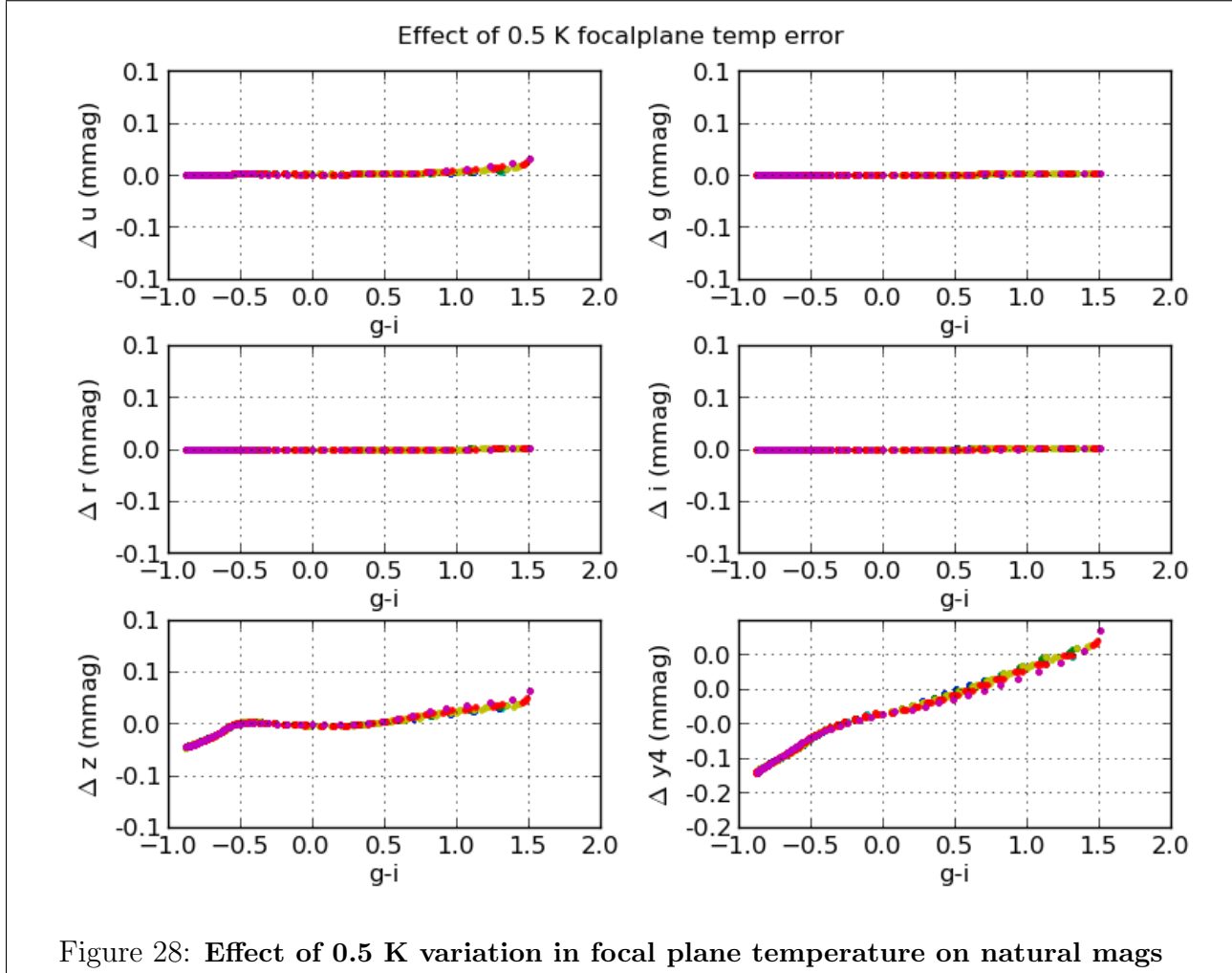
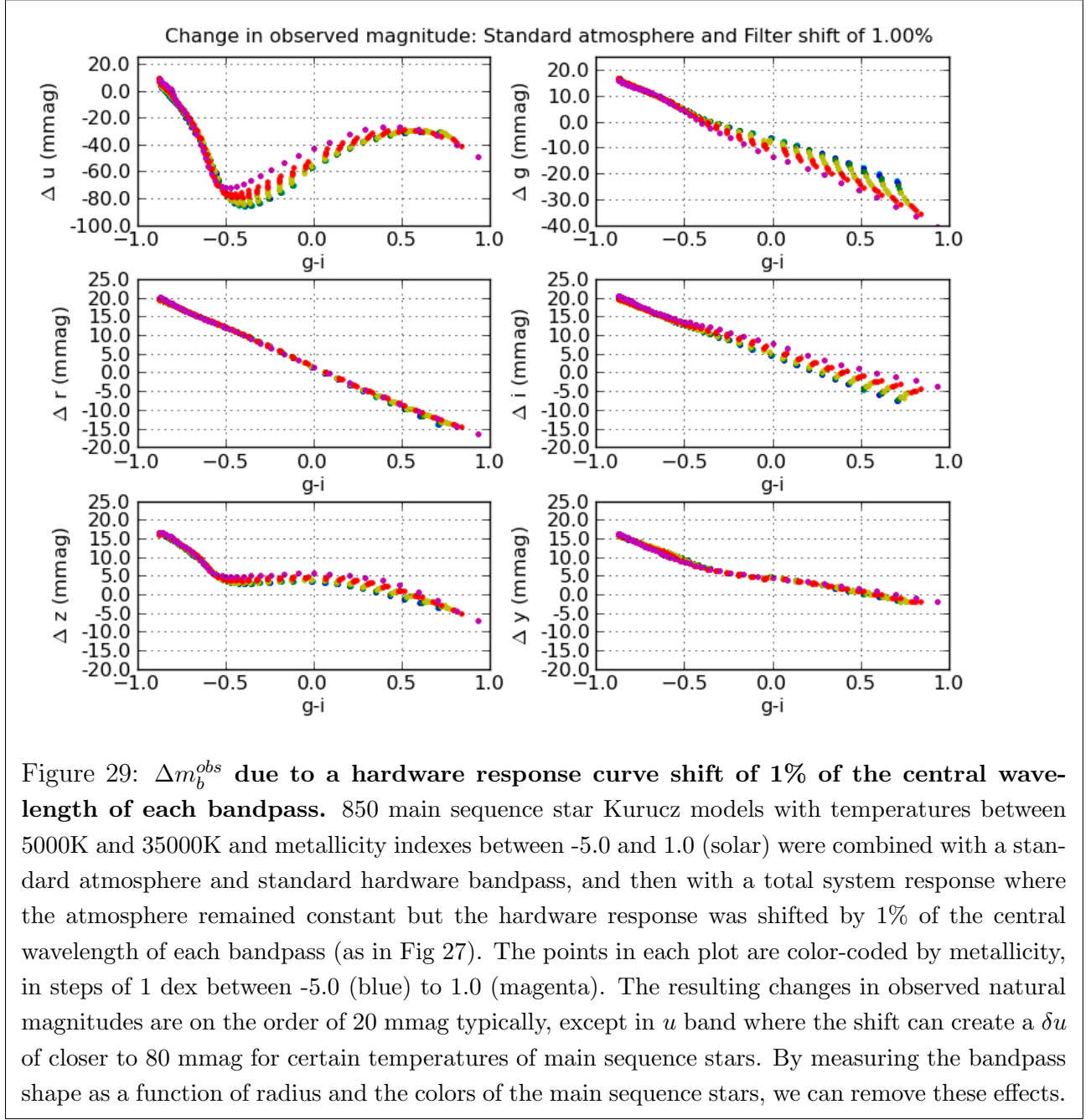
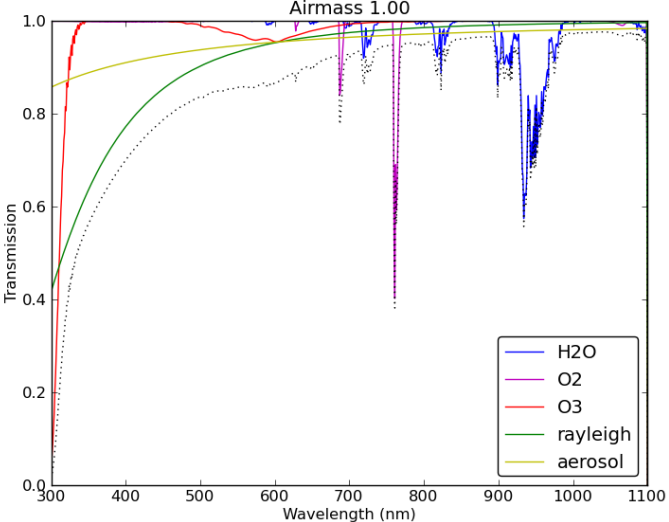


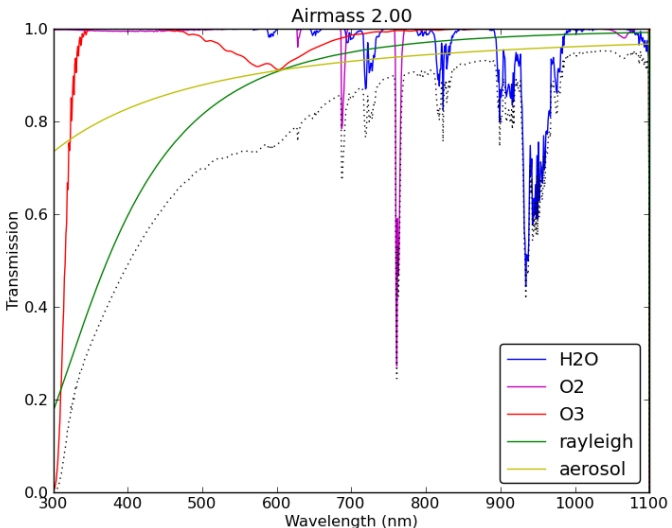
Figure 27: **Baseline filter curves and a potential (1% of the central wavelength) shift due to nonuniformity in the filter bandpass.** The solid lines indicate standard filter bandpasses (top panel: filter alone, bottom panel: filter plus standard mirror, lens, detector and atmosphere response curves) while the dashed lines indicate the same bandpass shifted redward by 1% of the central wavelength.







(a)



(b)

Figure 30: Components of atmospheric absorption. The wavelength dependence of various atmospheric absorption components at zenith (Panel 30a) and at airmass=2.0 (Panel 30b) are shown here. The H₂O (blue) and O₃ (red) molecular absorption contributions are shown separately, while the O₂ absorption is combined with other trace elements (magenta). A typical example of aerosol scattering (Mie scattering) is included (yellow), as is molecular scattering (Rayleigh scattering) (green). All components except aerosol scattering were generated using MODTRAN4 with the US Standard option (aerosol scattering is not part of the US Standard atmosphere). The resulting total absorption curve is the product of each of these effects and is shown with the dotted black line. This is an illustrative atmosphere; under actual observing conditions the molecular absorption components will vary in strength with time and the square root of the airmass, the molecular and aerosol scattering will depend on airmass, and the aerosol scattering profile will also vary with time.

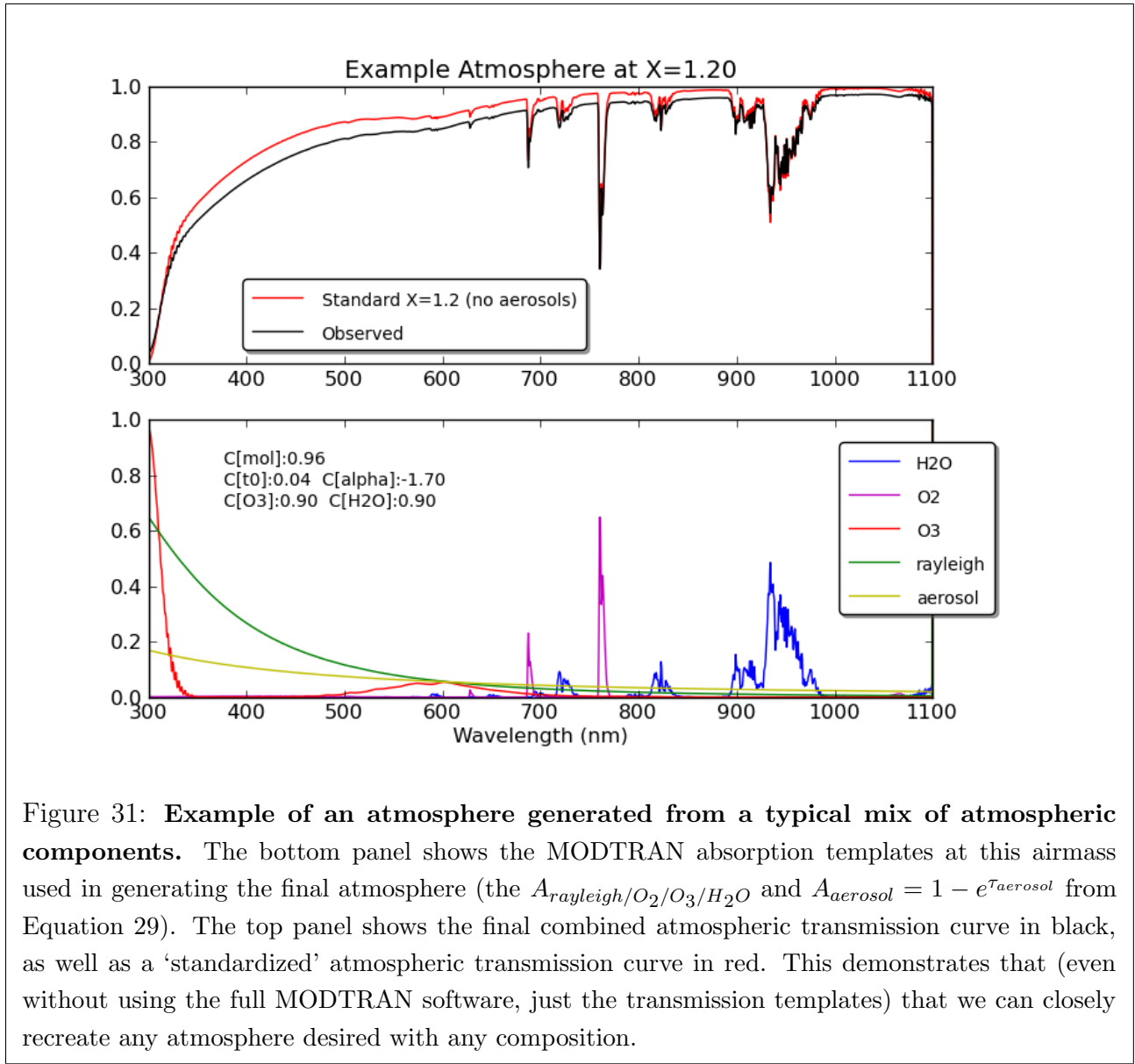


Figure 31: Example of an atmosphere generated from a typical mix of atmospheric components. The bottom panel shows the MODTRAN absorption templates at this airmass used in generating the final atmosphere (the $A_{rayleigh}/O_2/O_3/H_2O$ and $A_{aerosol} = 1 - e^{\tau_{aerosol}}$ from Equation 29). The top panel shows the final combined atmospheric transmission curve in black, as well as a ‘standardized’ atmospheric transmission curve in red. This demonstrates that (even without using the full MODTRAN software, just the transmission templates) that we can closely recreate any atmosphere desired with any composition.

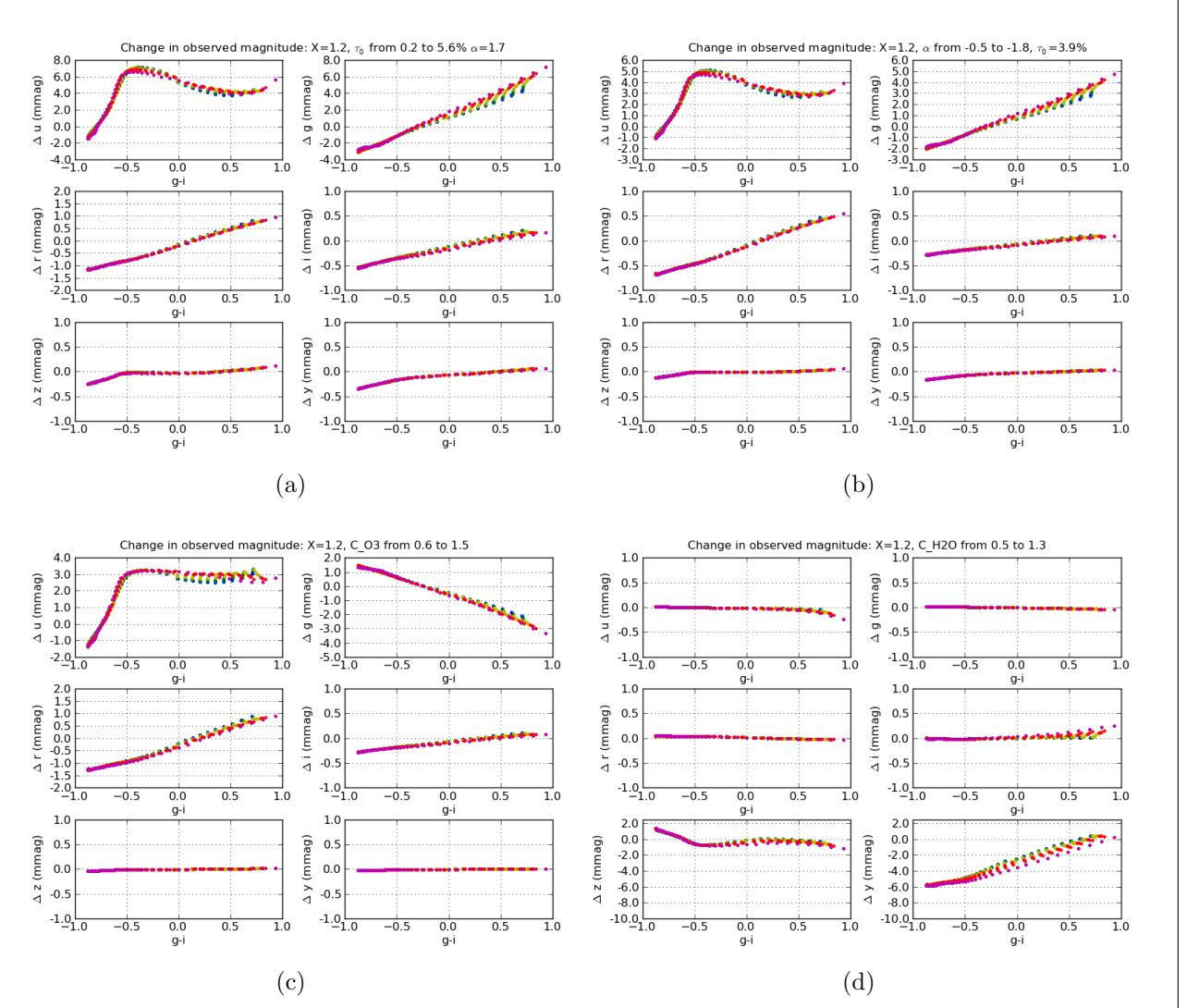
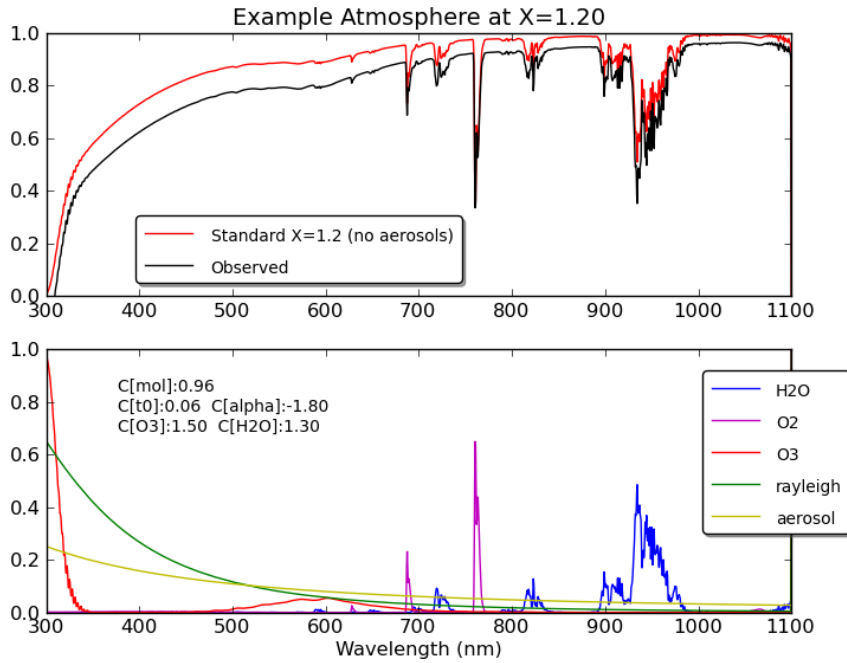
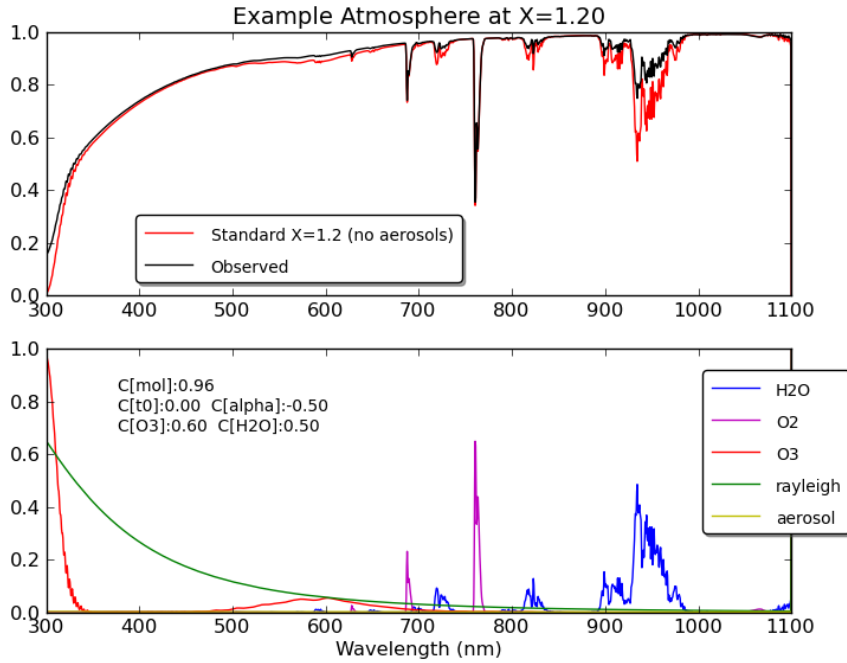


Figure 32: Δm_b^{obs} due to variations of each individual absorption component. Each atmospheric transmission curve (at $X=1.2$) was combined with the set of main sequence Kurucz curves to determine the resulting changes in observed magnitudes, as in Figure 29. Panels 46a and 46b show the effects of varying aerosol absorption in τ_0 and α respectively, Panel 32c shows the effect of varying O_3 absorption. These effects are concentrated in u and g bands, with a negligible effect in izy . Panel 32d shows the effect of varying the H_2O absorption, which is strongest in y , with some effect in z and no effect in $ugri$.

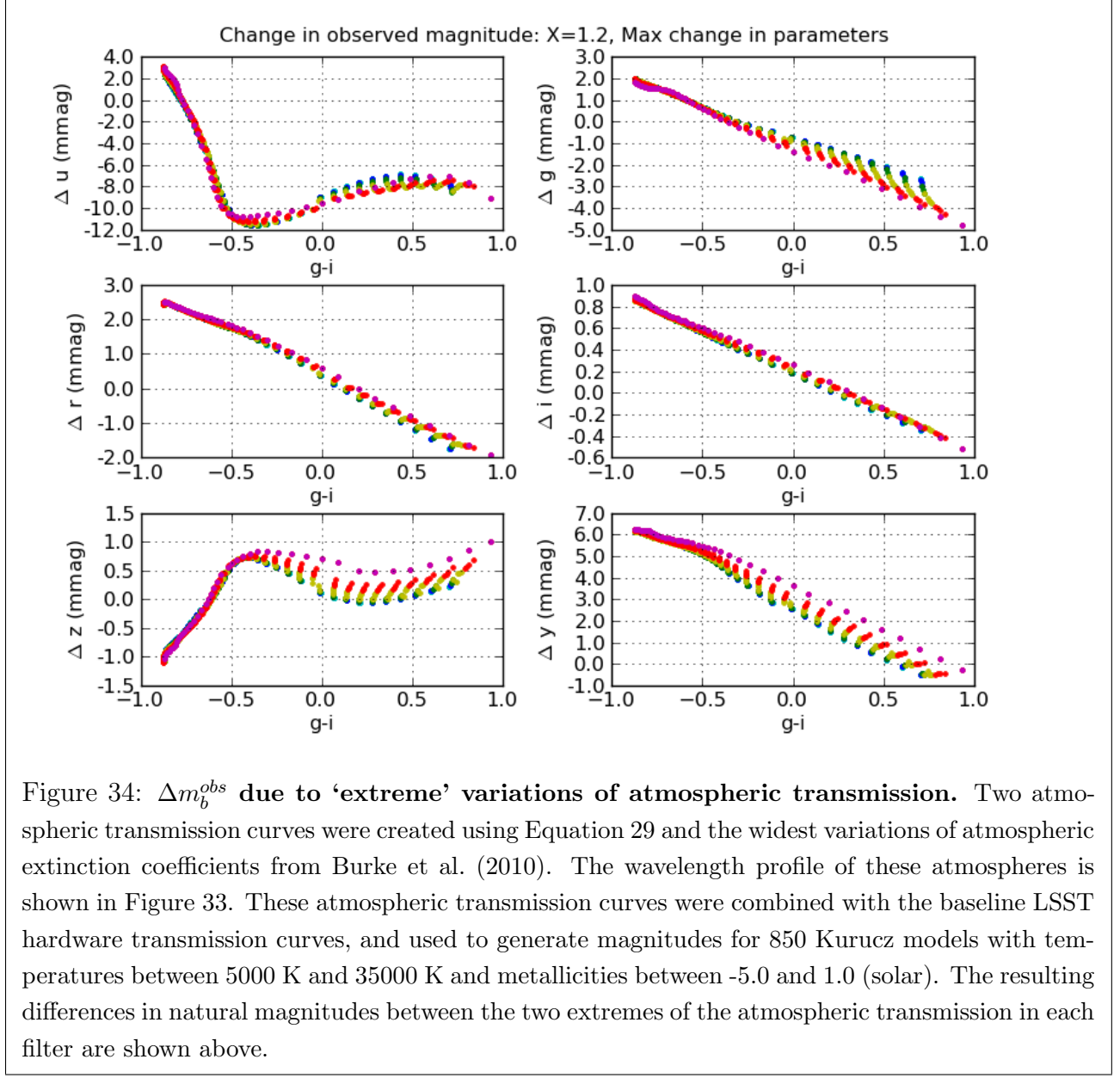


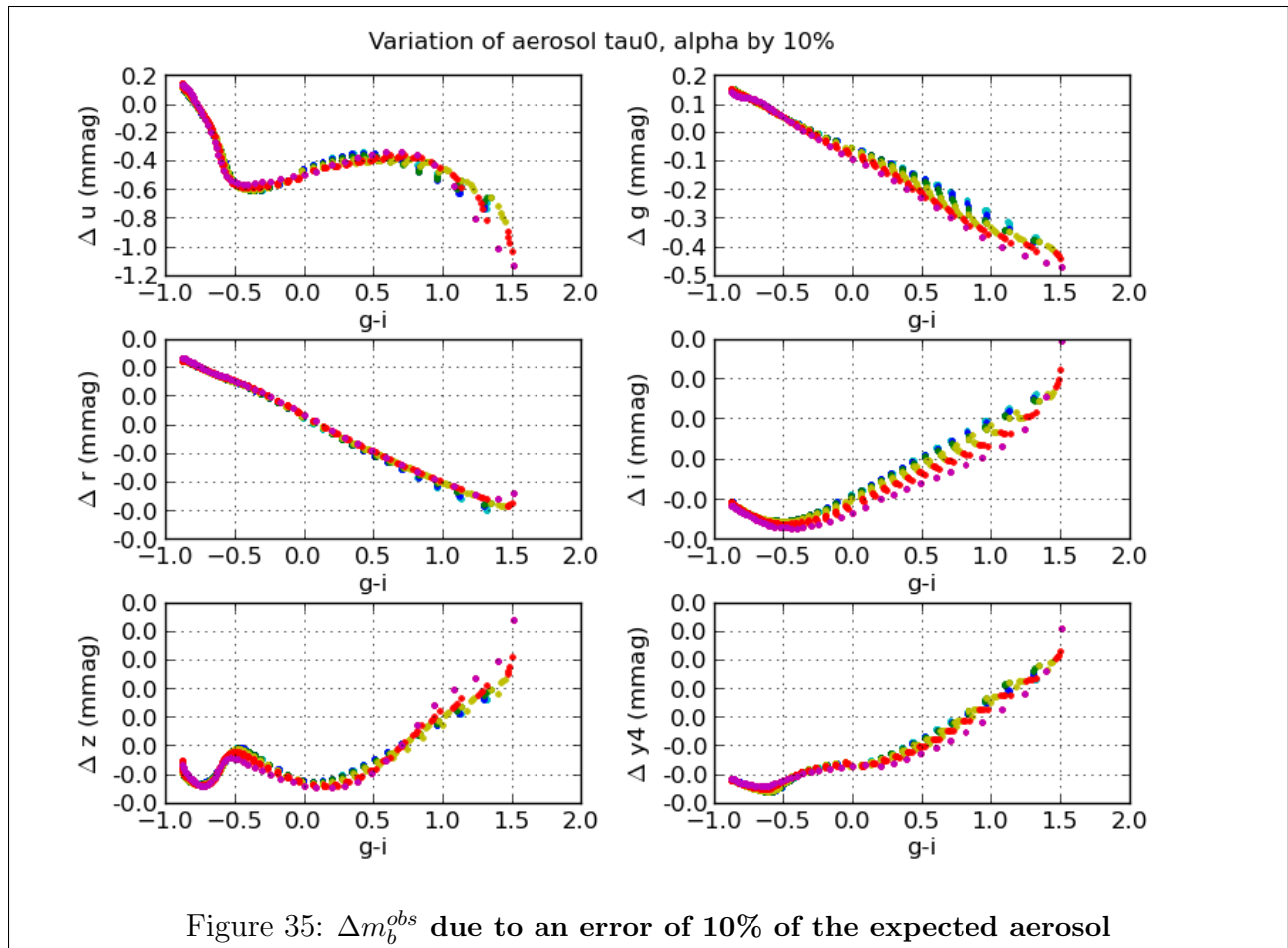
(a)

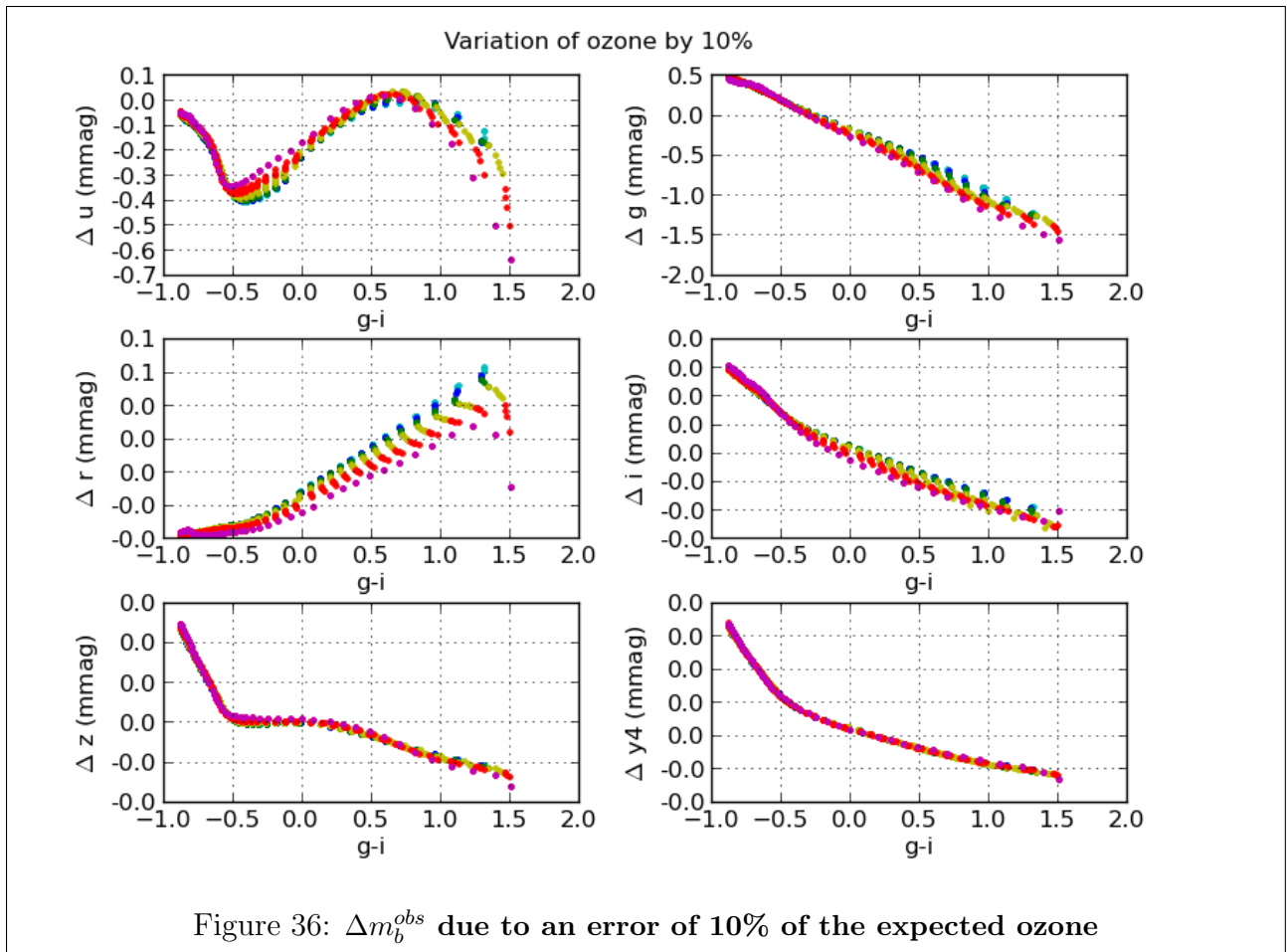


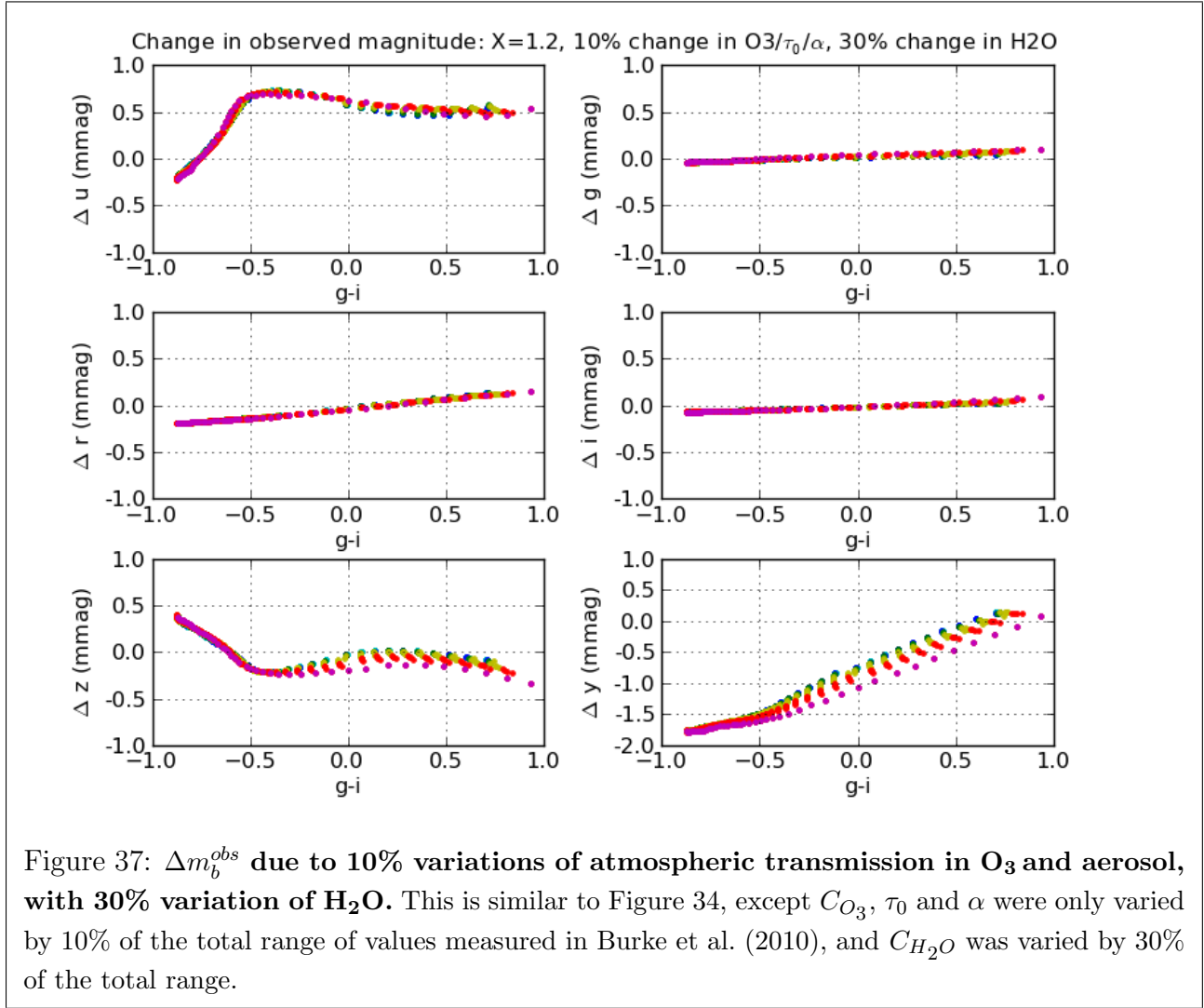
(b)

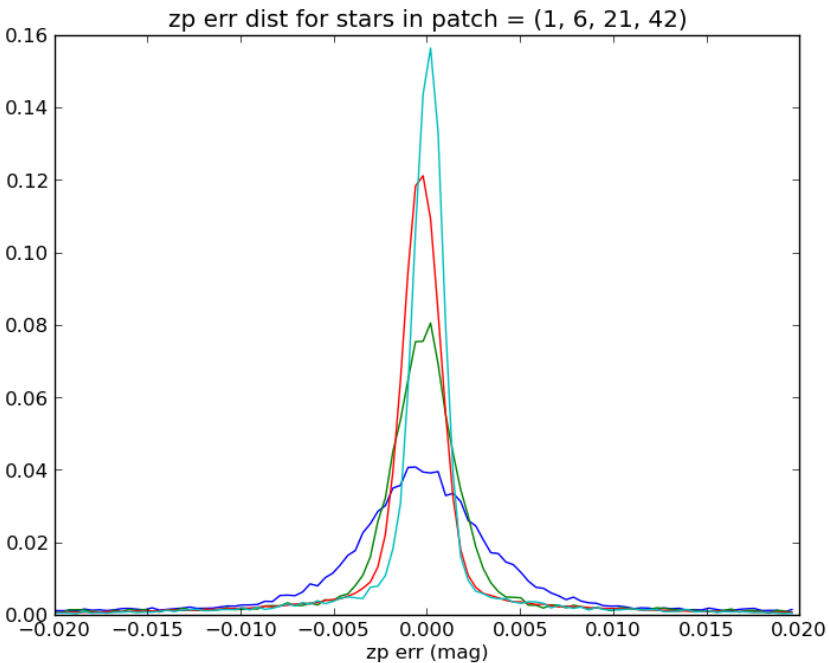
Figure 33: ‘Extreme’ atmospheres generated from MODTRAN profiles and extremes of atmospheric coefficients. Using the extremes of $C_{\text{H}_2\text{O}}$, C_{O_3} , and τ_0 and α from Burke et al. (2010), two test atmospheres with $X = 1.2$ were created using Equation 29.



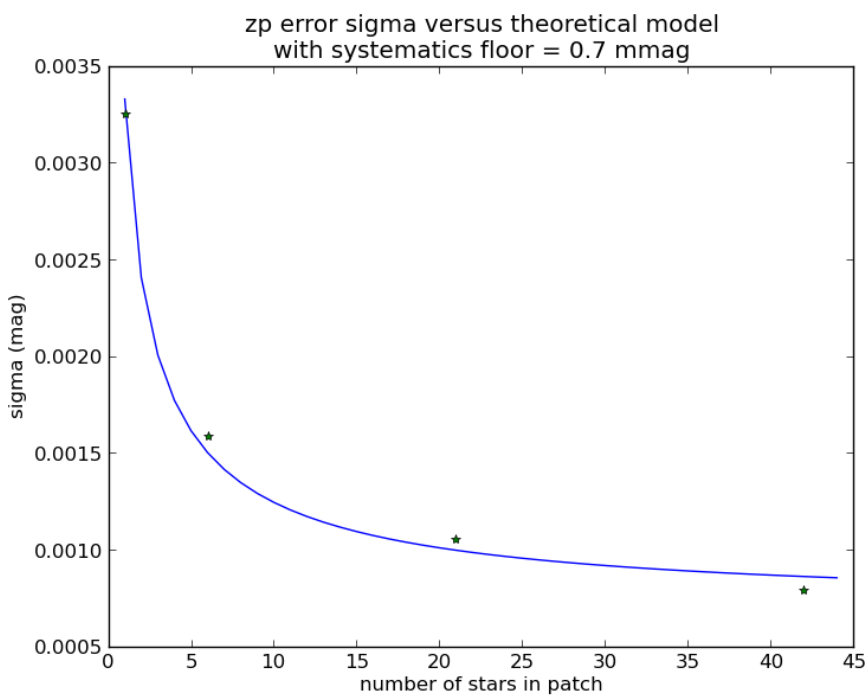






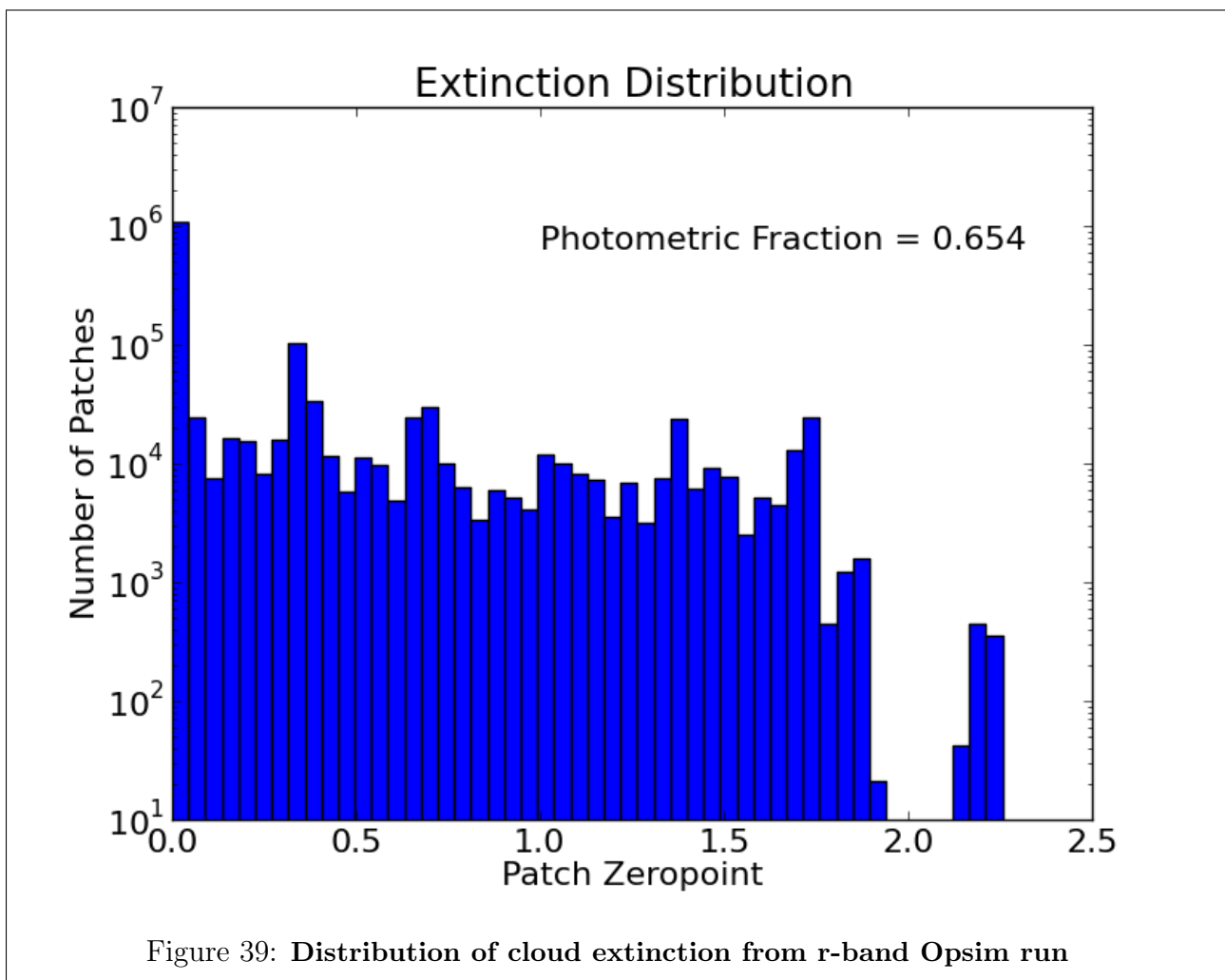


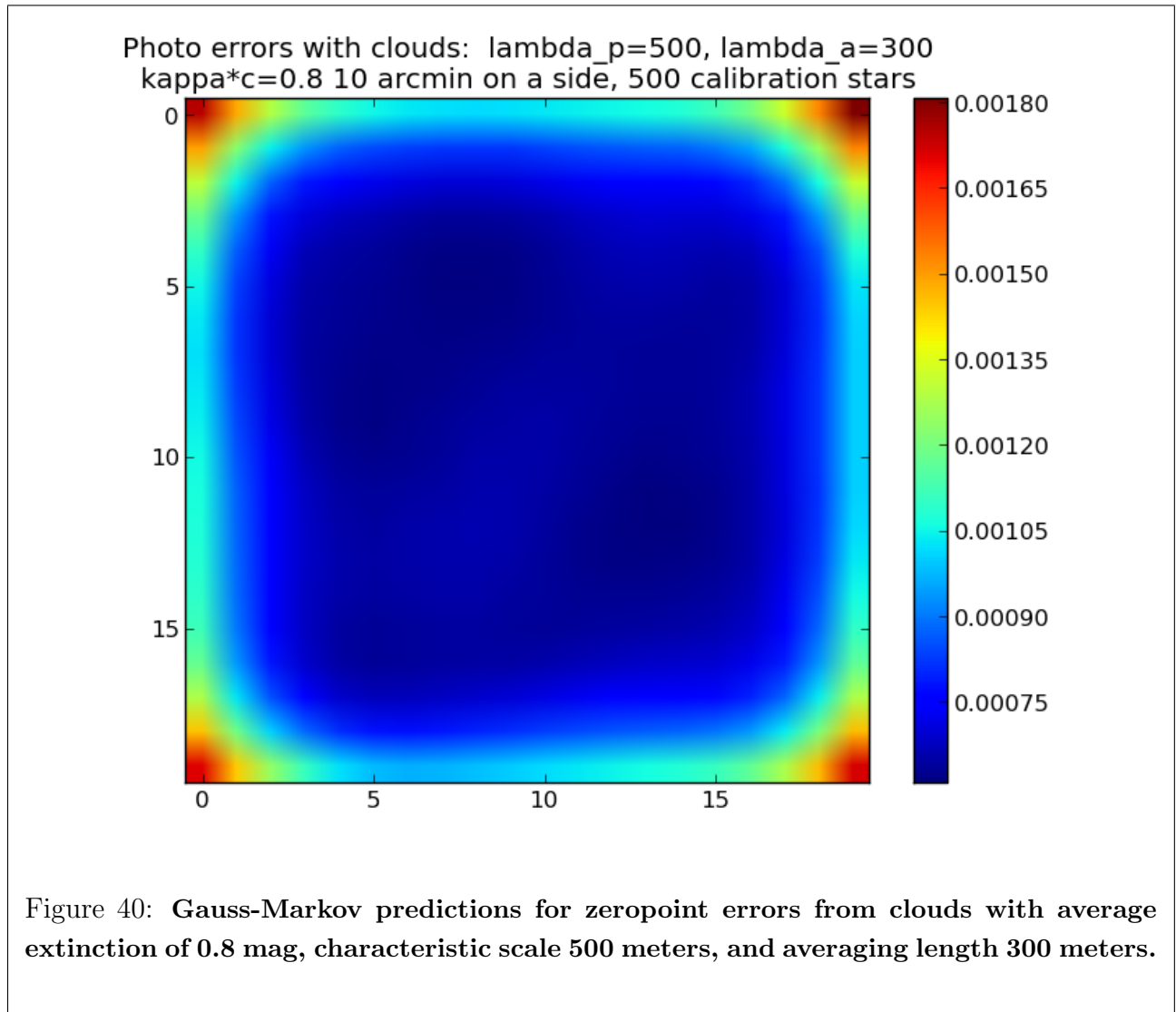
(a)

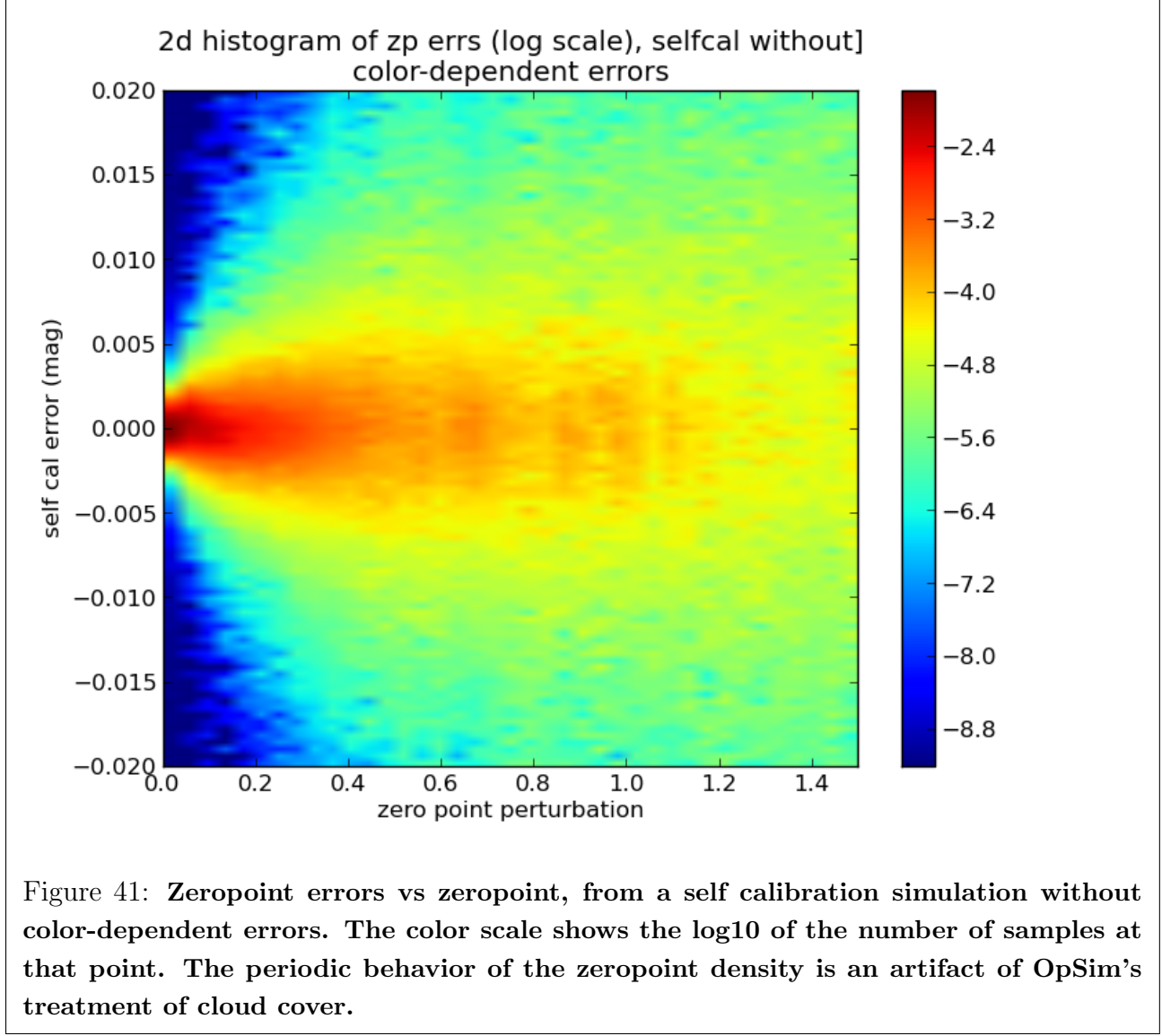


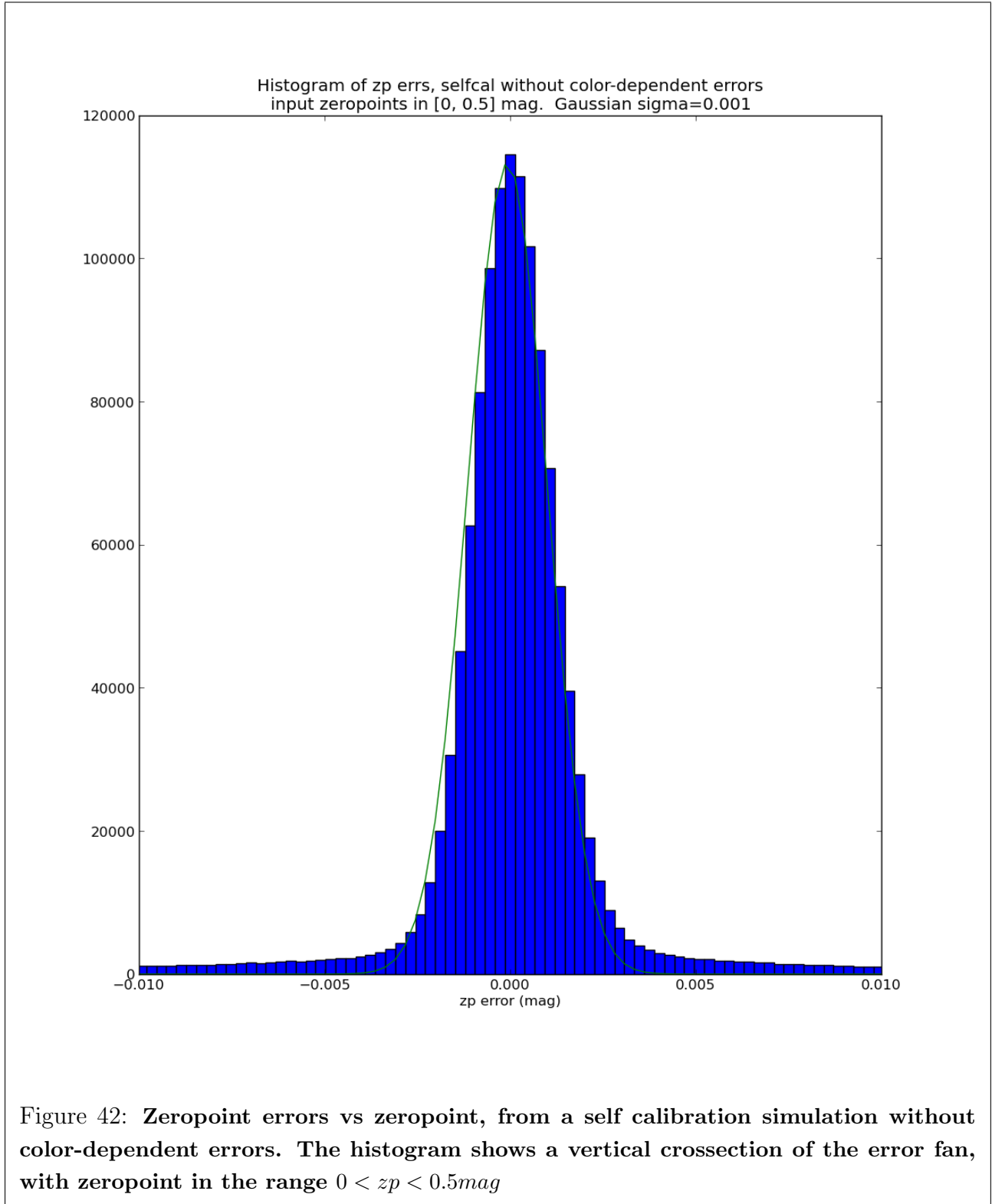
(b)

Figure 38: Zeropoint error distributions from an r-band simulation with no color-dependent errors. The top plot shows the distribution of errors for calibration patches with varying number of stars. The bottom plot shows the behavior of the σ of the Gaussian core as a function of the number of stars. The solid curve is the σ_{sat} function discussed in the text.









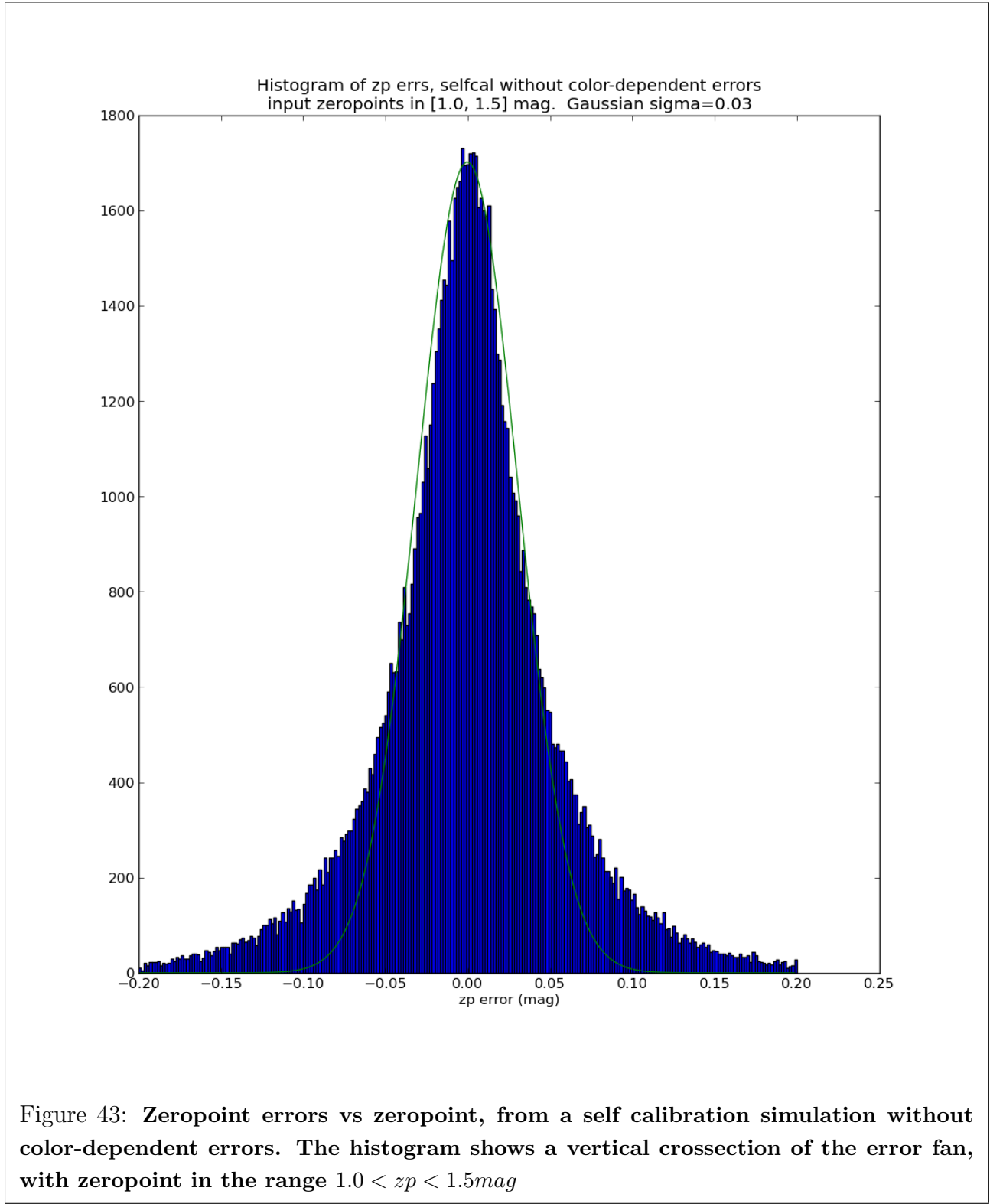


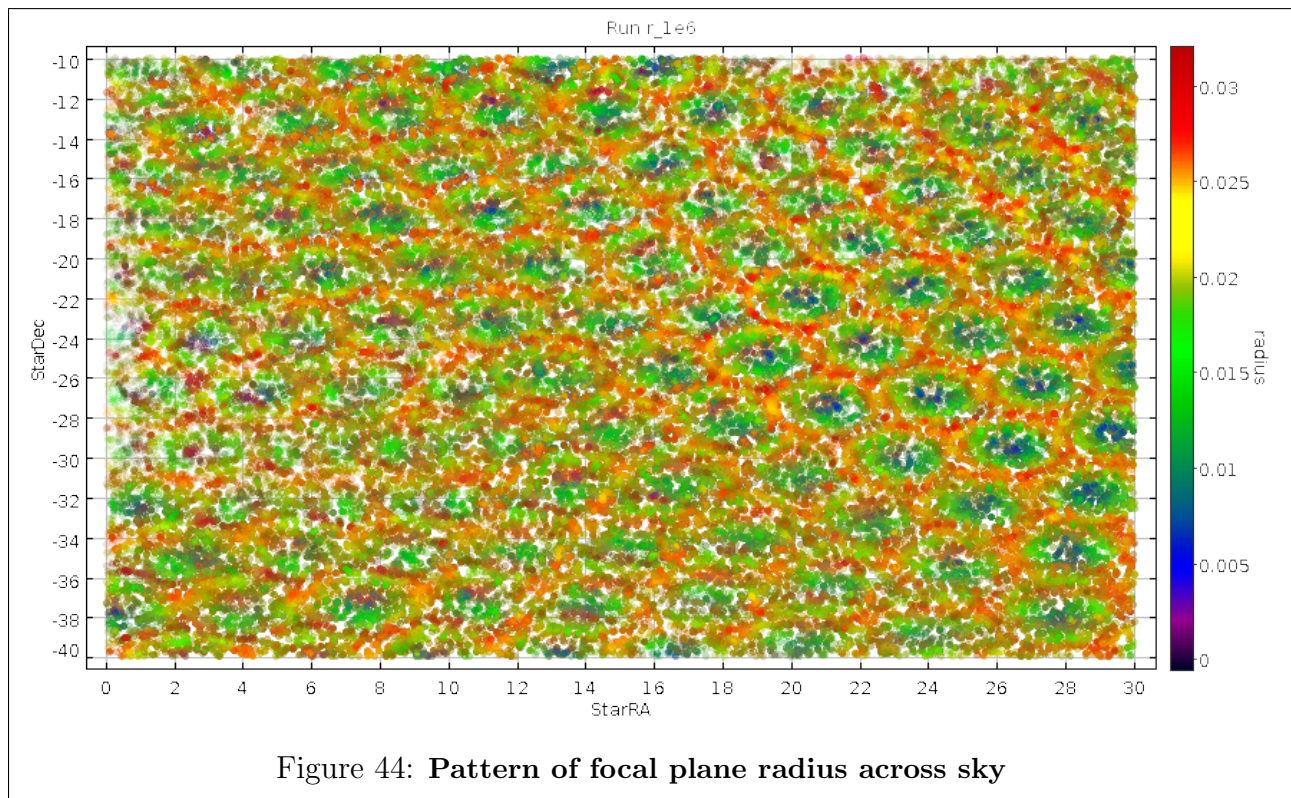
Table 3:: Repeatability error budget. All values are in mmag

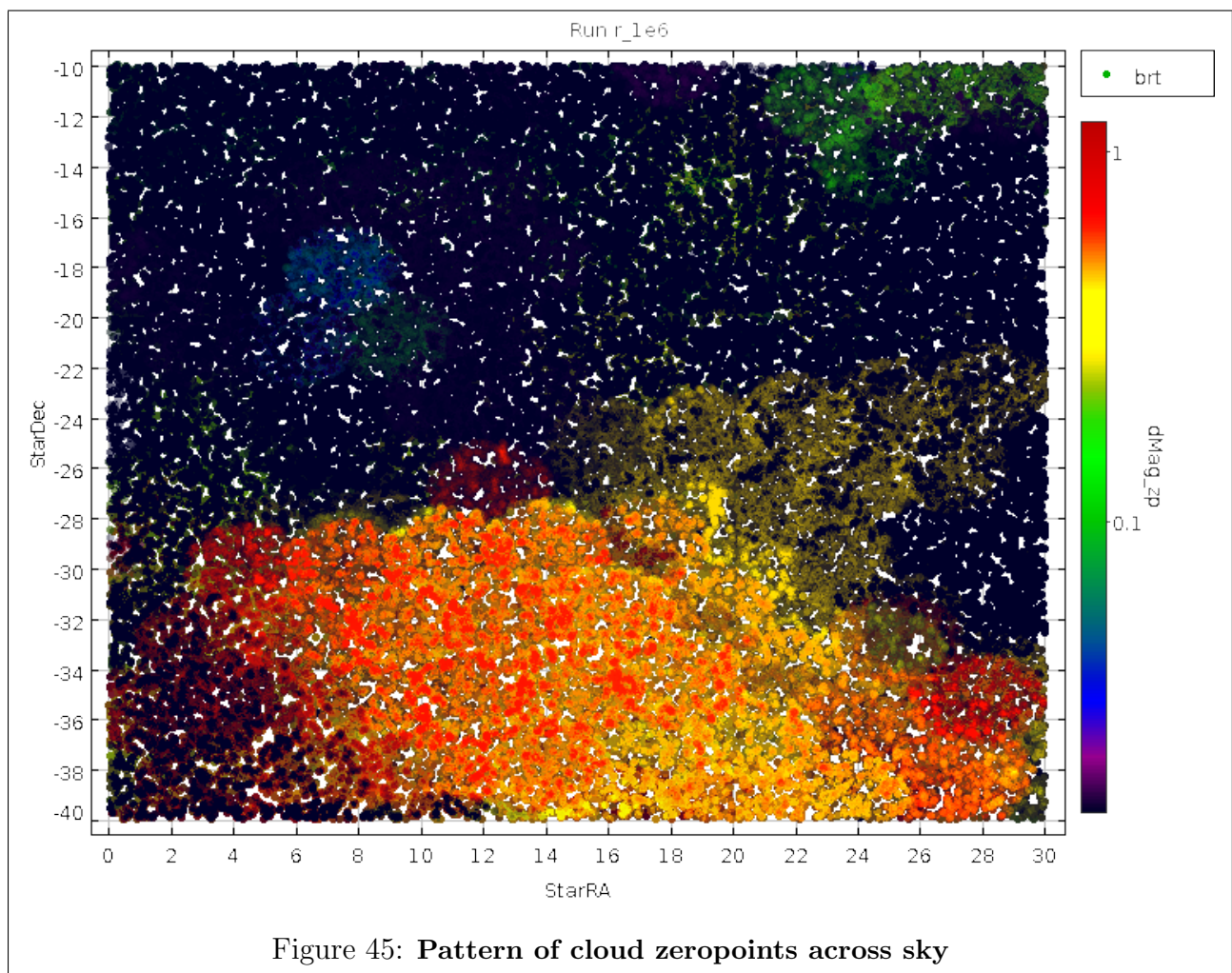
Affected term	Effect	<i>u</i>	<i>g</i>	<i>r</i>	<i>i</i>	<i>z</i>	<i>y</i>
m_b^{obs}	Total	3.0	3.0	3.0	3.0	3.0	3.0
Δm_b^{obs}	Atmospheric water vapor errors	0.2	0	0	0	1.0	2.0
	Atmospheric aerosol and ozone errors	1.6	2.1	0.1	0	0	0
	Undetected atmospheric variability	1.4	0.7	0	0	0	0
	Monochromatic illumination correction errors	3.0	0.5	0.8	0.5	0.1	0.6
	Photodiode monitoring system errors	0.8	0.5	0	0	0	0.1
	Calibration star SED errors	5.6	0.8	0.5	0.4	0.4	0.2
	Focal plane temperature errors	0	0	0	0	0	0.2
	Filter positioning errors	1.0	0.5	0.5	0.5	0.5	0.5
	Total	6.8	2.5	1.1	0.8	1.2	2.2
Z_b^{obs}	Saturated self calibration errors from clouds (90% of obs), atmosphere, and camera effects	2.0	2.0	2.0	2.0	2.0	2.0
Total Estimate		7.7	4.4	3.7	3.8	3.8	4.2
Simulation Result (IQR Median)		8.0	4.9	5.0	5.0	4.4	6.1
Design Requirement		7.5	5.0	5.0	5.0	7.5	7.5
Min. Requirement		12	8.0	8.0	8.0	12	12

 | 10⁷ |

Table 4:: Simulated uniformity errors. All values are in mmag

	<i>u</i>	<i>g</i>	<i>r</i>	<i>i</i>	<i>z</i>	<i>y</i>
Simulation Result (RMS)	8.0	2.0	1.6	1.8	2.3	TBD
Design Requirement	20	10	10	10	10	10
Min. Requirement	30	15	15	15	15	15





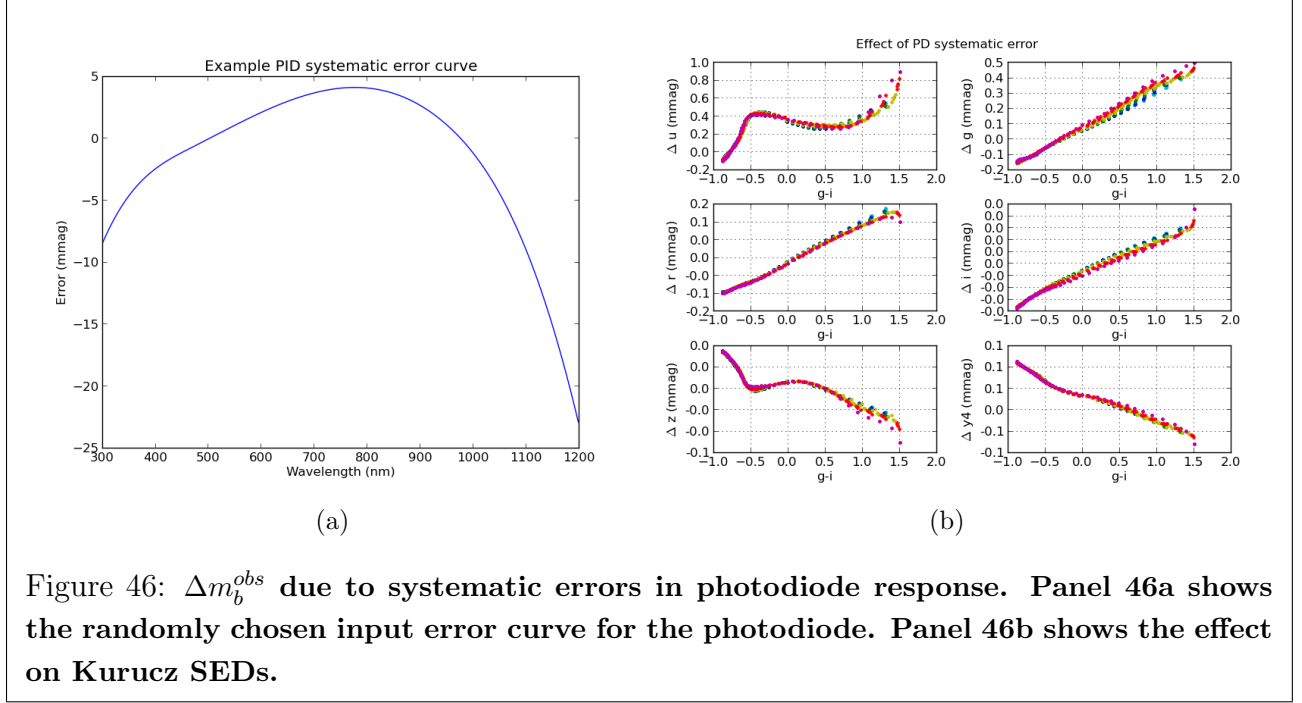


Figure 46: Δm_b^{obs} due to systematic errors in photodiode response. Panel 46a shows the randomly chosen input error curve for the photodiode. Panel 46b shows the effect on Kurucz SEDs.

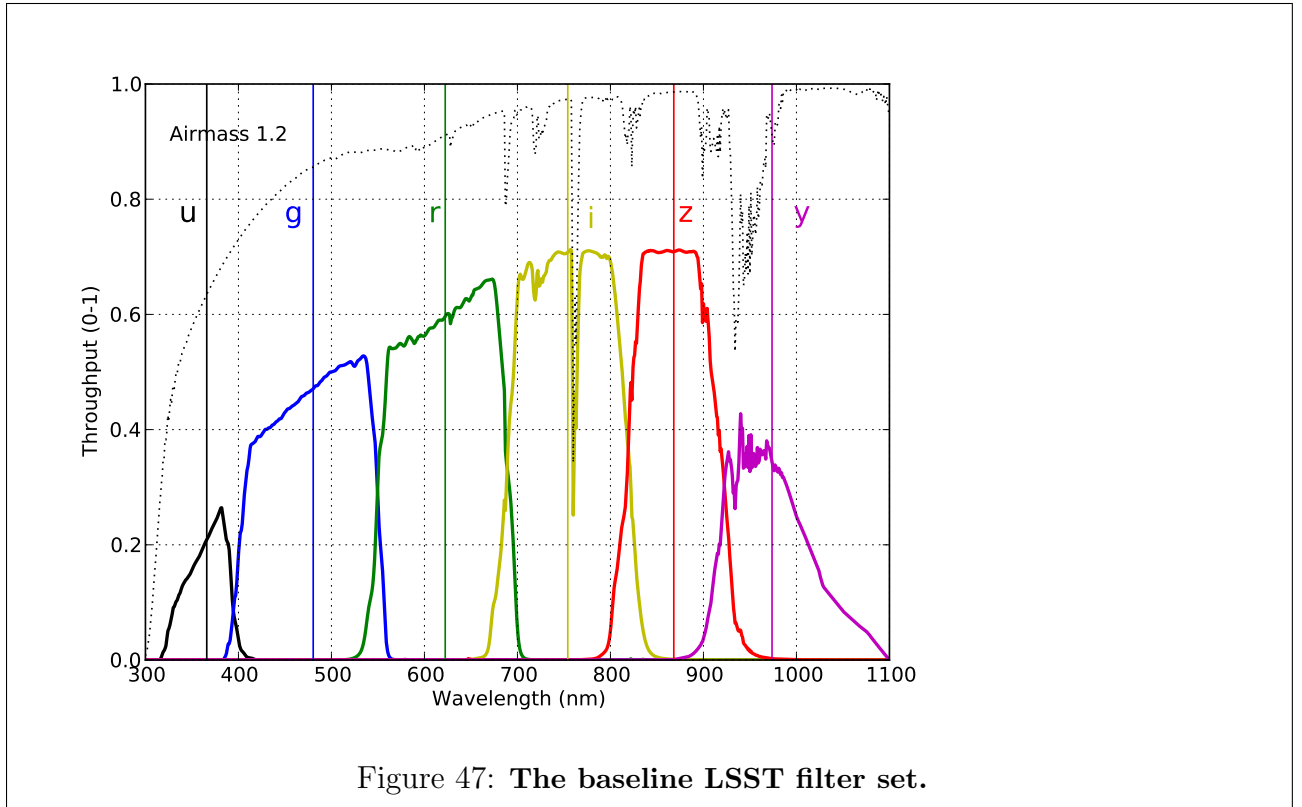
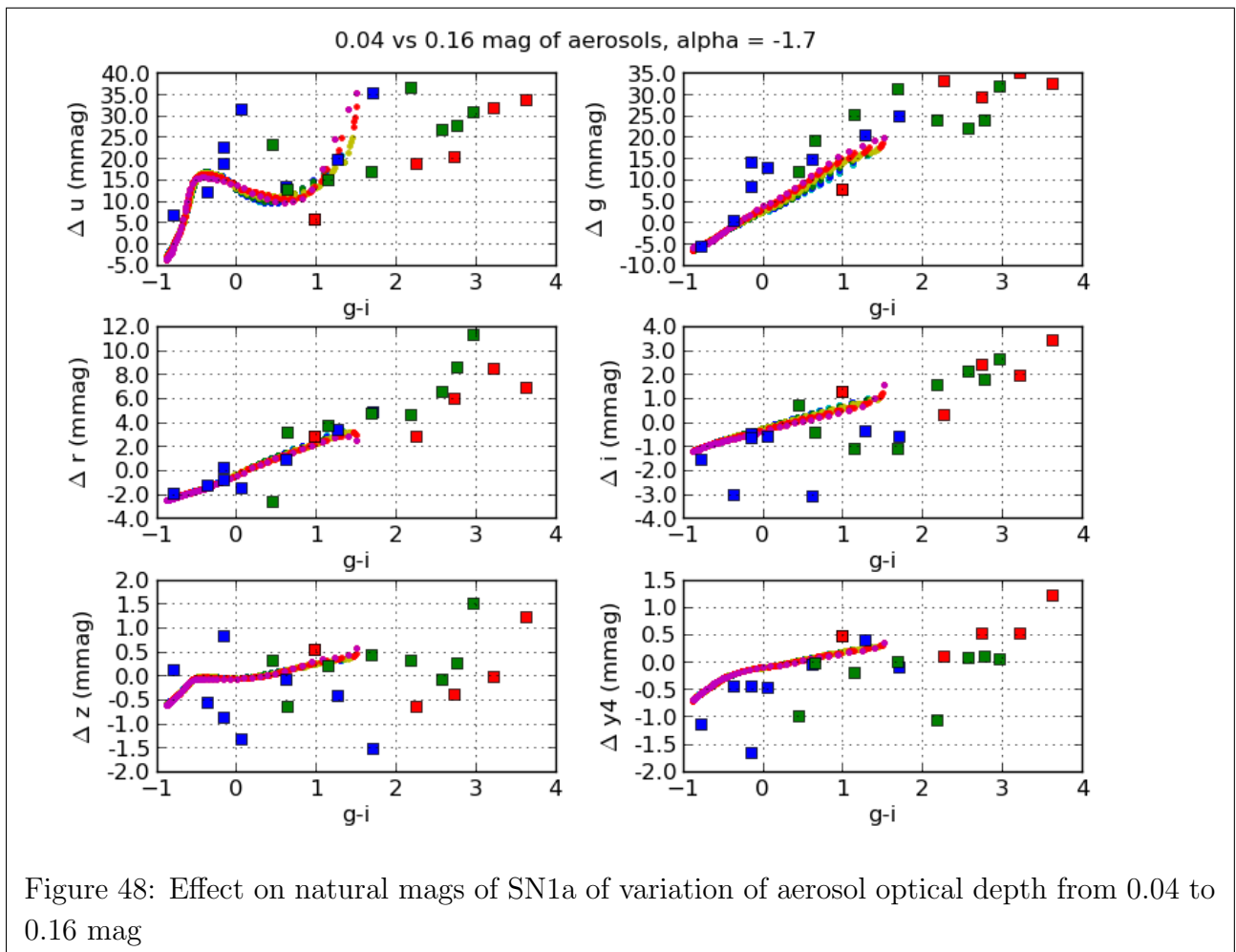
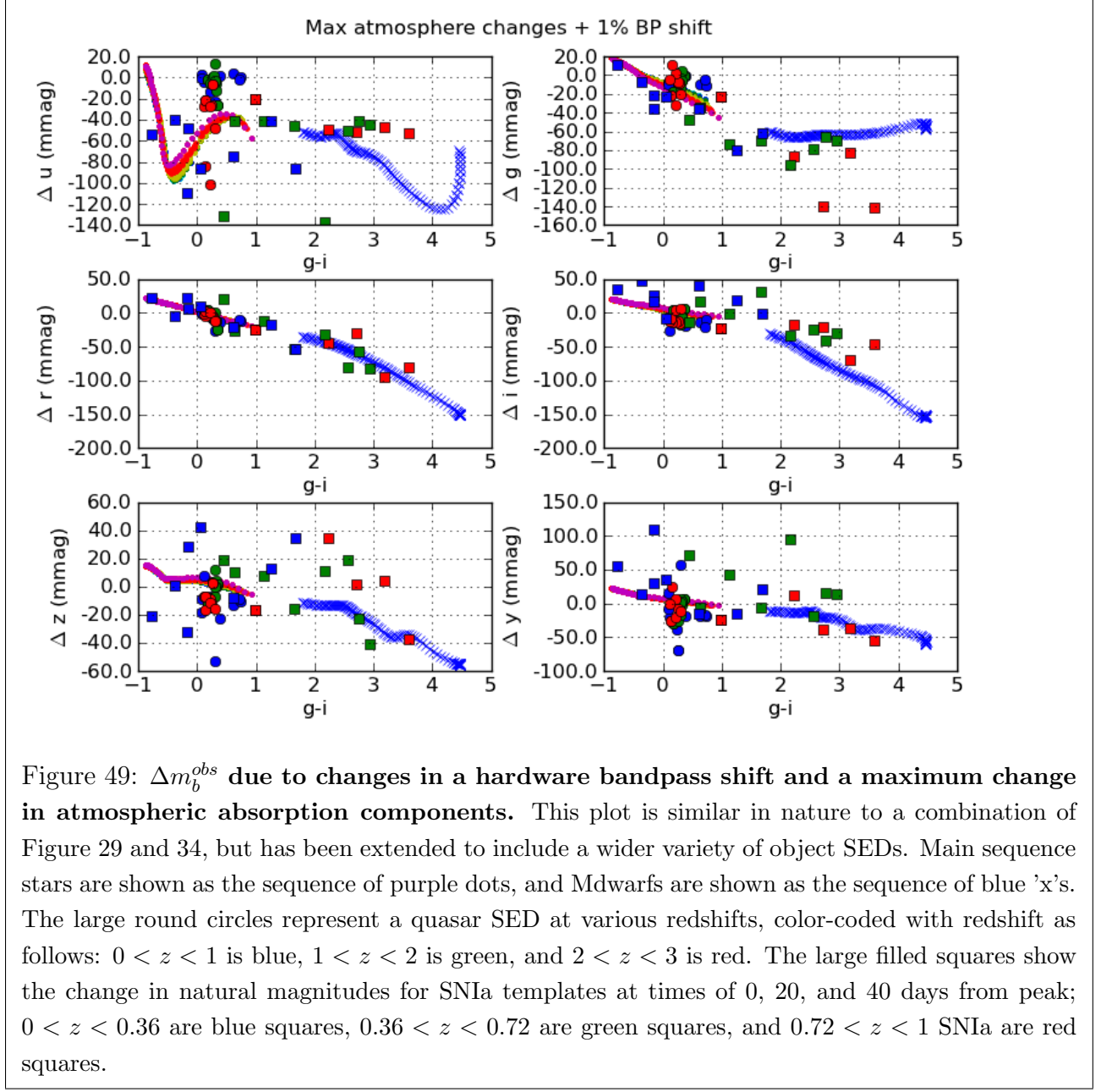
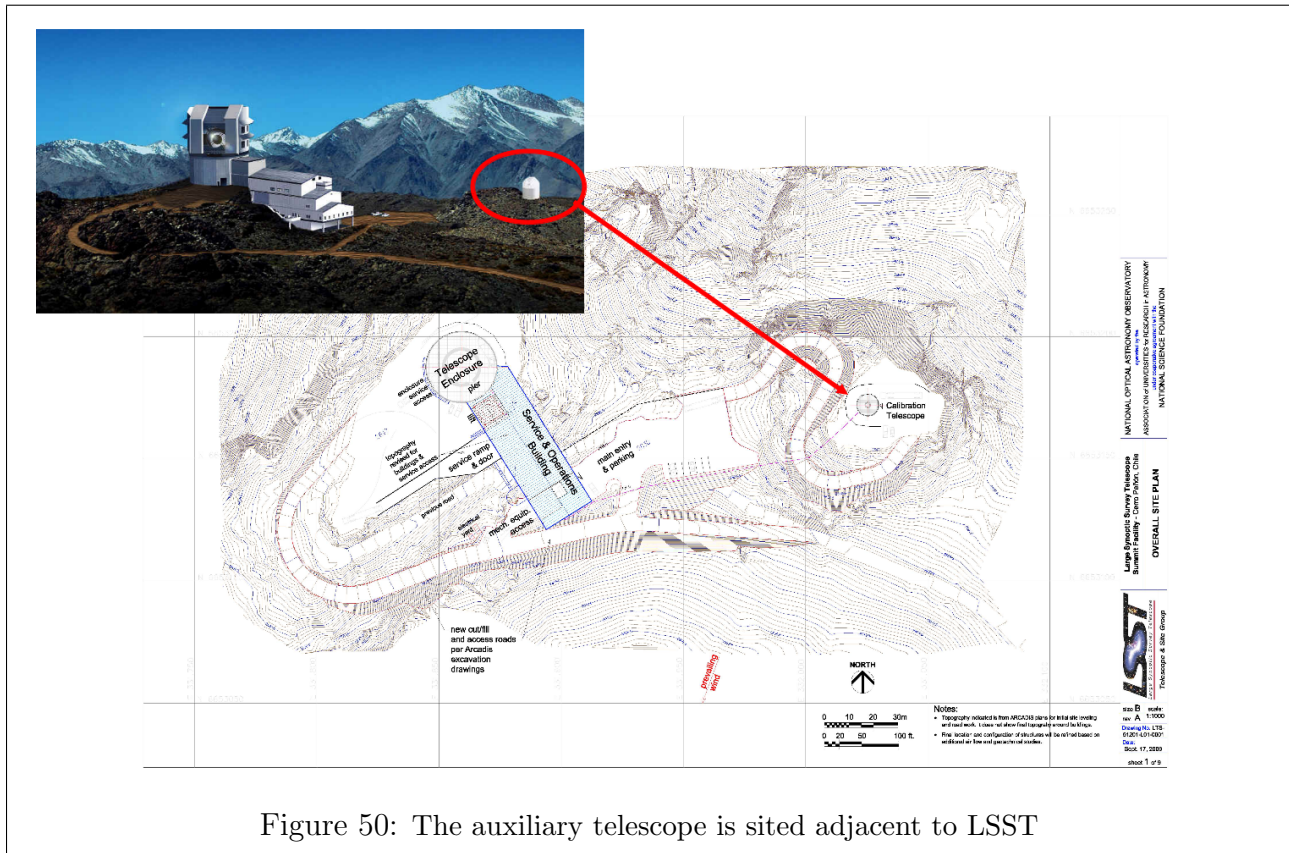
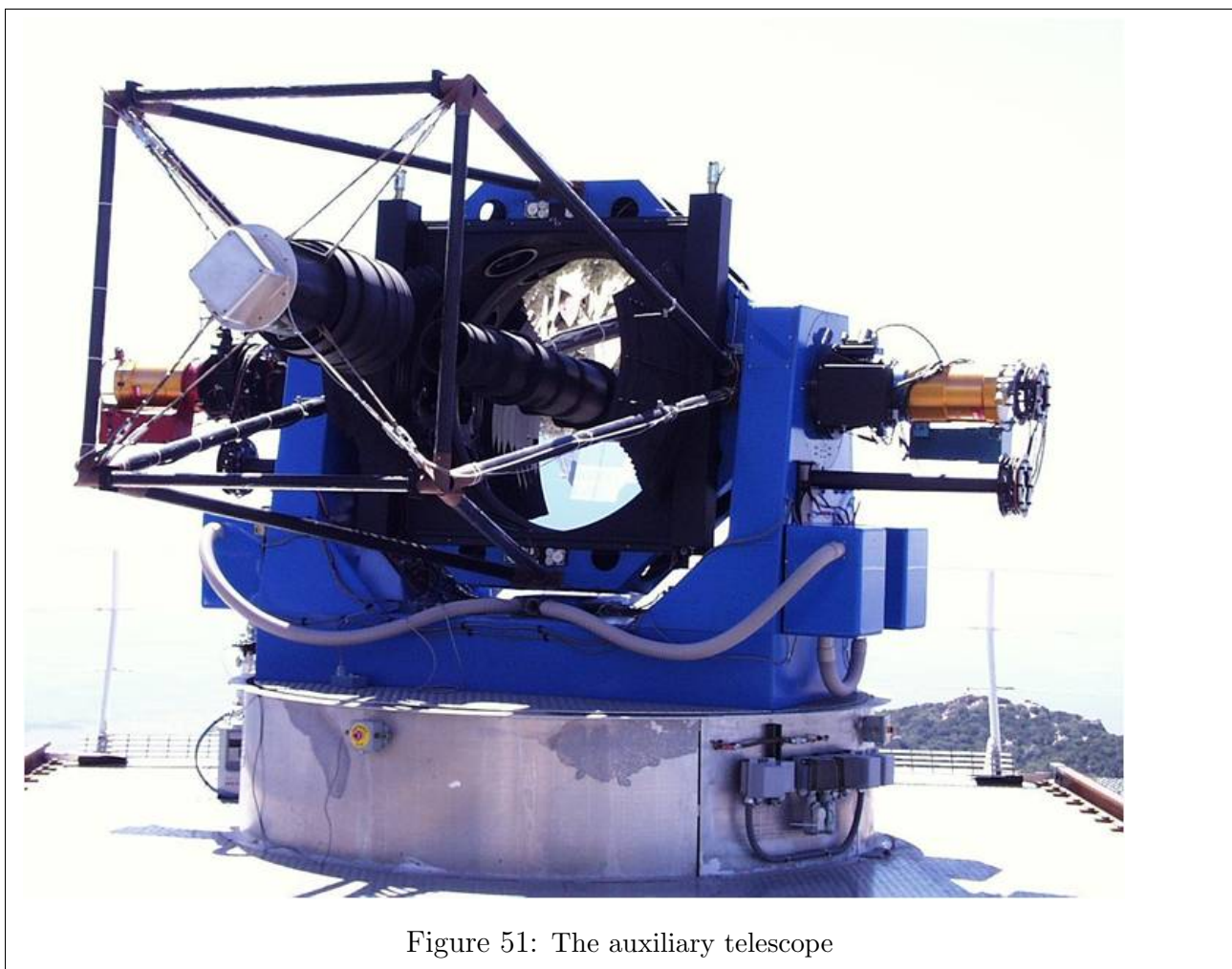


Figure 47: The baseline LSST filter set.









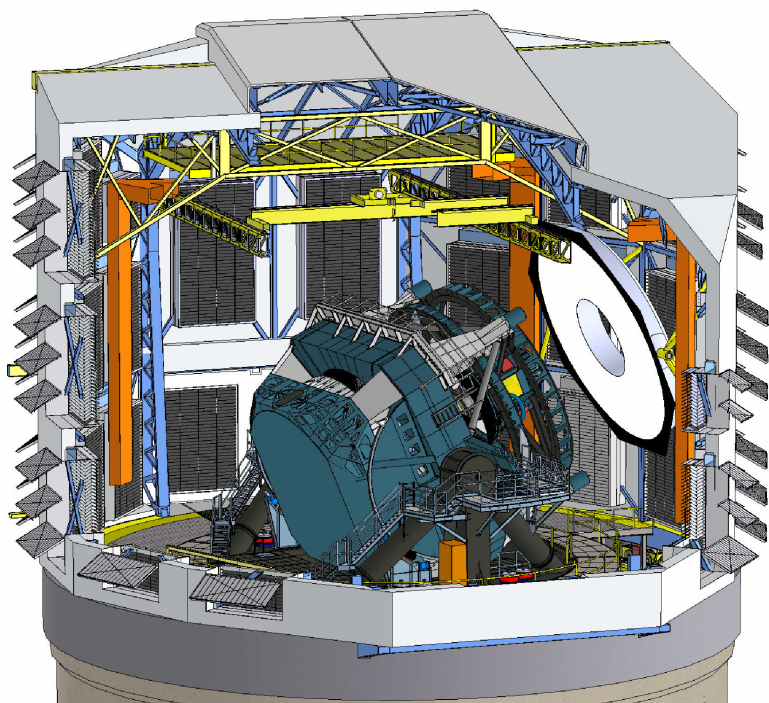
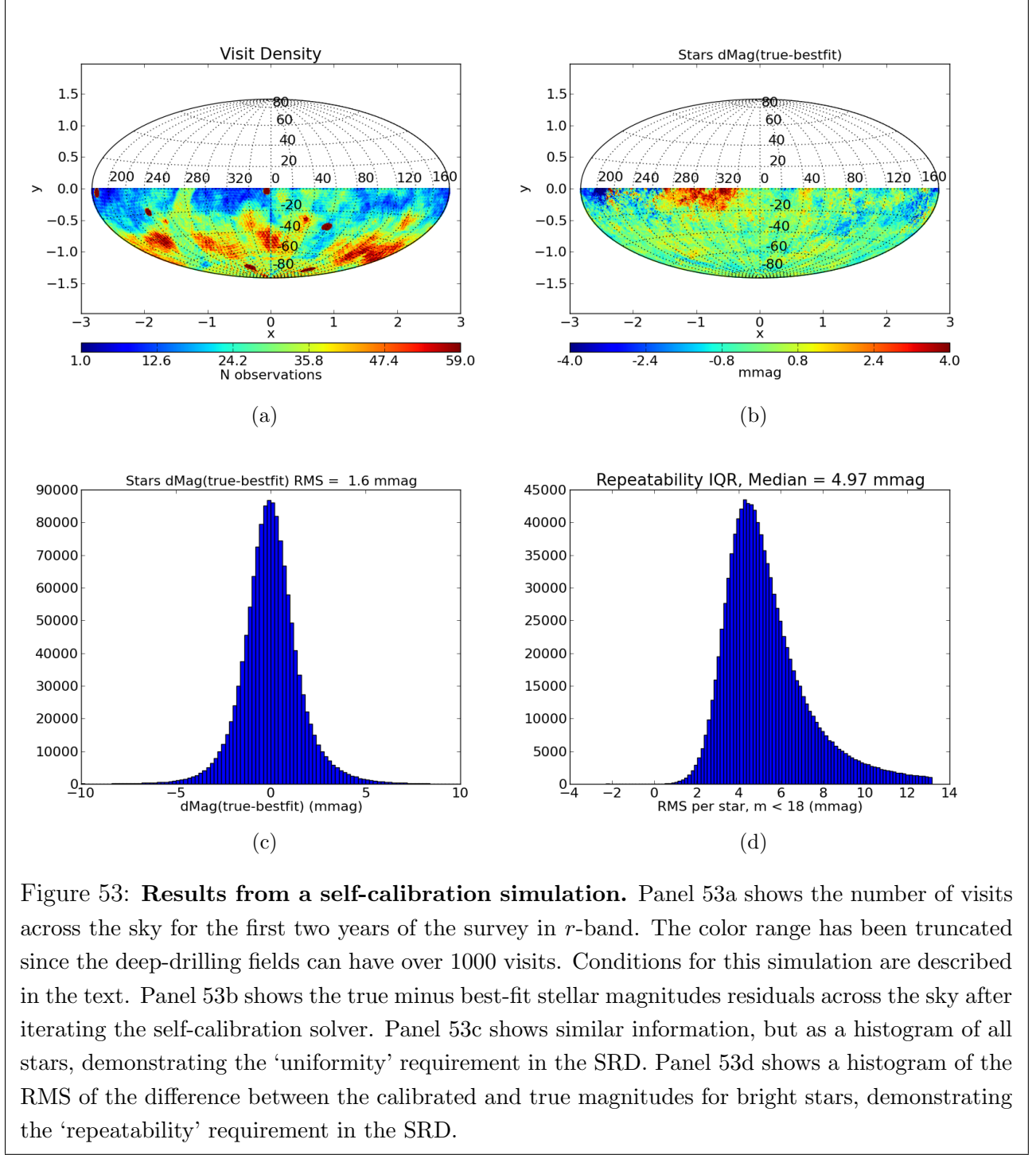
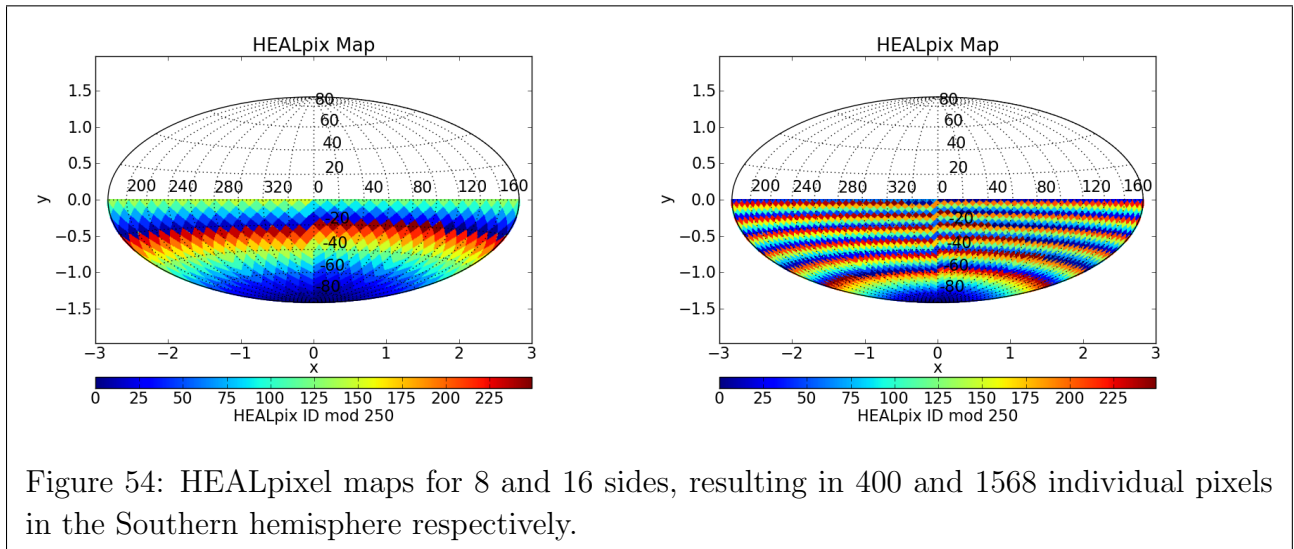
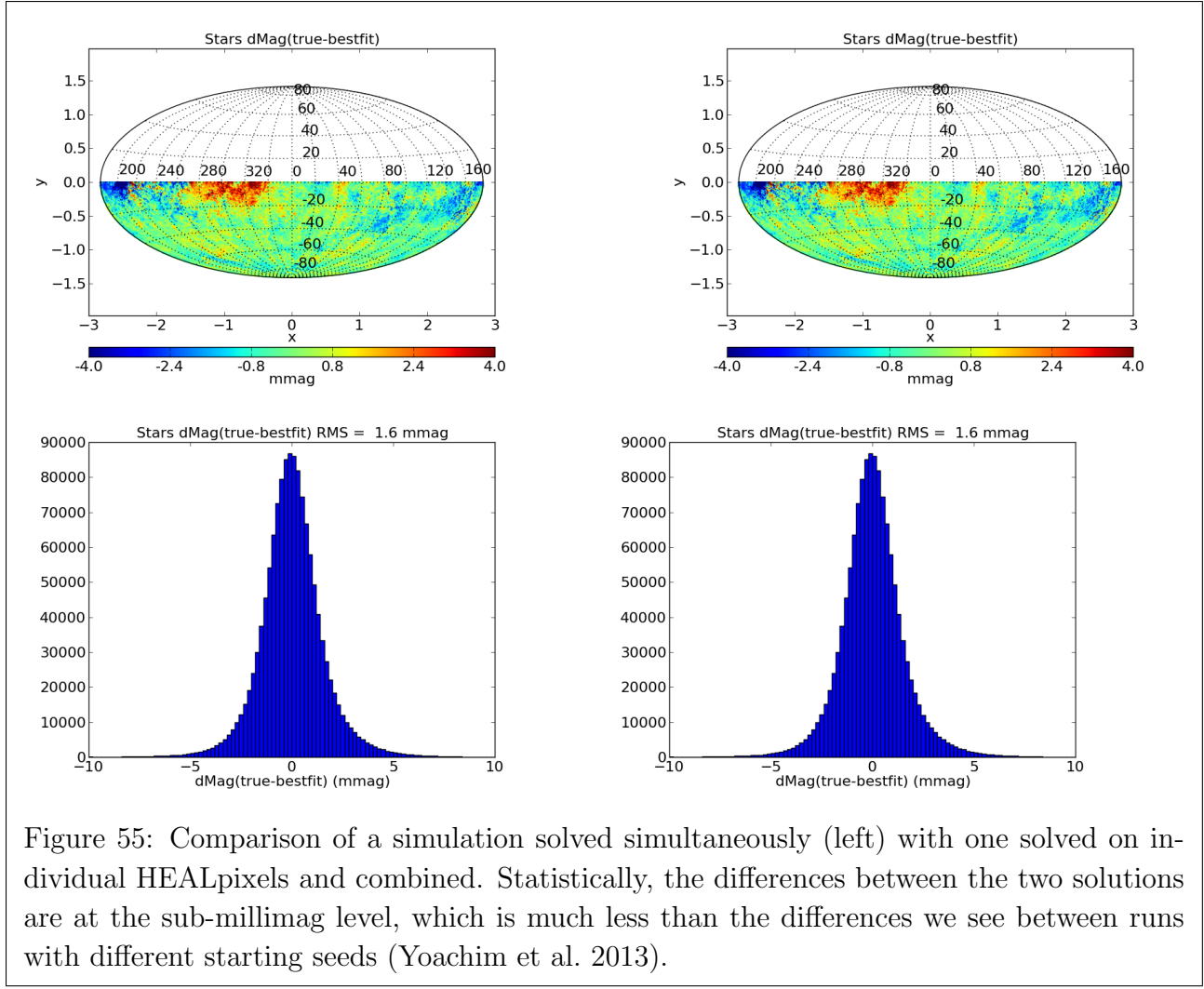


Figure 52: The flat field dome screen in front of the telescope







Standard deviation of true relative error atmospheric transmission, SNR ~ 210.9

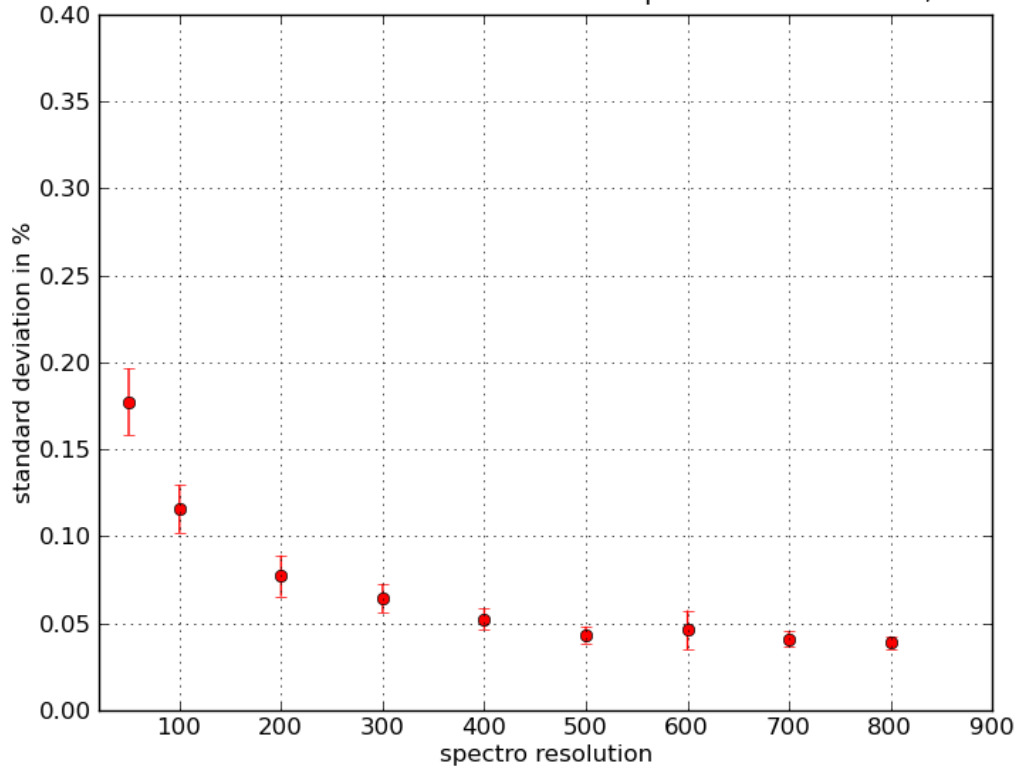


Figure 56: errors in atmospheric transmission functions determined over 7 nights with 80 spectra per night. The x axis is the spectrograph resolution. Improvement of resolution beyond 400 does not improve the accuracy. This may be linked to the similar resolution of the Kurucz spectra used for the stars.

